The first Miocene fossils from coastal woodlands in the southern East African Rift

René Bobe[1,2,3*], Vera Aldeias[3], Zeresenay Alemseged[4], Will Archer[5], Georges Aumaître[6+], Marion K. Bamford[7], Dora Biro[8], Didier L. Bourlès[6], David R. Braun[9], Cristian Capelli[10], João d'Oliveira Coelho[2,11], Jörg M. Habermann[12], Jason J. Head[13], Karim Keddadouche[6+], Kornelius Kupczik[14], Anne-Elisabeth Lebatard[6], Tina Lüdecke[2,15,16], Amélia Macôa[17], Felipe I. Martínez[18], Jacinto Mathe[2], Clara Mendes[17], Luis Meira Paulo[19], Maria Pinto[19], Thomas A. Püschel[2,20], Frederico Tátá Regala[3], Mark Sier[21], Maria Joana Ferreira da Silva[22,23], Marc Stalmans[1], Susana Carvalho[1,2,3,11*]

*Corresponding author
René Bobe: renebobe@gmail.com

Main text: ~9000 words
Number of figures: 18
Number of tables: 4
Number of supplementary tables: 9
Supporting Information: ~3200 words

Authors' affiliations

[1] Gorongosa National Park, Sofala, Mozambique

[2] Primate Models for Behavioural Evolution Lab, Institute of Human Sciences, School of Anthropology, University of Oxford, UK

[3] Interdisciplinary Center for Archaeology and Evolution of Human Behavior (ICArEHB), Universidade do Algarve, Portugal

[4] Department of Organismal Biology & Anatomy, University of Chicago, Chicago, USA

[5] Department of Archaeology, National Museum, Bloemfontein, South Africa

[6] Centre Européen de Recherche et d'Enseignement de Géosciences de l'Environnement CEREGE - UM 34 Aix-Marseille Université, CNRS, IRD, Collège de France, INRAE OSU Institut Pythéas. Technopole Environnement Arbois - Méditerranée, Domaine du Petit Arbois, Avenue Louis Philibert, Les Milles-Aix en Provence BP80, 13545 AIX en Provence, CEDEX 04, France
[6+] ASTER-Team

[7] Evolutionary Studies Institute and School of Geosciences, University of the Witwatersrand, Johannesburg, South Africa

[8] Department of Zoology, University of Oxford, UK

[9] Center for the Advanced Study of Human Paleobiology, Department of Anthropology, George Washington University, Washington, DC, USA

[10] Dipartimento delle Scienze Chimiche, della Vita e della Sostenibilità Ambientale, Università di Parma, Italy

[11] Centre for Functional Ecology, University of Coimbra, Coimbra, Portugal

[12] GeoZentrum Nordbayern, Friedrich-Alexander-Universität Erlangen-Nürnberg, Erlangen, Germany

[13] Department of Zoology, University of Cambridge, UK

[14] Department of Human Evolution, Max Planck Institute for Evolutionary Anthropology, Leipzig, Germany

[15] Emmy Noether Group for Hominin Meat Consumption, Max Planck Institute for Chemistry, Mainz, Germany

[16] Senckenberg Biodiversity and Climate Research Centre, Frankfurt, Germany

[17] Departamento de Arqueologia e Antropologia, Faculdade de Letras e Ciências Sociais, Universidade Eduardo Mondlane, Maputo, Mozambique

[18] Faculty of Social Sciences, School of Anthropology, Pontificia Universidad Católica de Chile, Santiago, Chile

[19] ASDA – Associação de Estudos Subterrâneos e Defesa do Ambiente, Portugal

[20] Ecology and Evolutionary Biology Division, School of Biological Sciences, University of Reading, UK

[21] CENIEH, Burgos, Spain

[22] Organisms and Environment Division, School of Biosciences, Cardiff University, UK

[23] CIBIO/InBio, Centro de Investigação em Biodiversidade e Recursos Genéticos, Universidade do Porto, Portugal

Abstract (200 words)

The Miocene is a key time in the evolution of African mammals and their ecosystems witnessing the origin of the African apes and the isolation of eastern coastal forests through an expanding biogeographic arid corridor. Until recently, however, Miocene sites from the southeastern regions of the continent were unknown. Here we report discovery of the first Miocene fossil teeth from the shoulders of the Urema Rift in Gorongosa National Park, Mozambique, at the southern East African Rift System. We provide the first 1) radiometric age determinations of the fossiliferous Mazamba Formation, 2) reconstructions of past vegetation in the region based on pedogenic carbonates and fossil wood, and 3) description of fossil teeth from the southern rift. Gorongosa is unique in the East African Rift System in combining marine invertebrates, marine vertebrates, terrestrial mammals, and fossil woods in coastal paleoenvironments. The Gorongosa fossil sites offer the first evidence of persistent woodlands and forests on the coastal margins of southeastern Africa during the Miocene, and an exceptional assemblage of fossil vertebrates including new species. Further work will allow the testing of hypotheses positing the formation of a northeast-southwest arid corridor isolating species on the eastern coastal forests from those elsewhere in Africa.

Brief (150 words)

The Miocene is a key time in the evolution of African mammals and their ecosystems encompassing hominine origins and the establishment of an arid corridor that isolated eastern Africa's coastal forests. Until now, however, Miocene sites from southeastern Africa have been unknown. We report the discovery of the first Miocene fossil sites from Gorongosa National Park, Mozambique, and show that these sites formed in coastal settings. We provide radiometric ages for the fossiliferous sediments, reconstructions of past vegetation based on stable isotopes and fossil wood, and a description of the first fossil teeth from the region. Gorongosa is the only paleontological site in the East African Rift that combines fossil woods, marine invertebrates, marine vertebrates, and terrestrial mammals. Gorongosa offers the first evidence of persistent woodlands and forests on the coastal margins of southeastern Africa during the Miocene.

Interdisciplinary: geology, geochemistry, paleobotany, vertebrate paleontology, paleoecology, biogeography

Introduction

Much of our knowledge about African Miocene vertebrates and their environments derives from paleontological sites along the East African Rift System (EARS). However, considerable geographic and temporal gaps in the fossil record obscure a full appreciation of past biodiversity, biogeography, and ecosystem evolution on the continent. For example, until recently there were no sites with Miocene mammals in the southern 1,500 km of the EARS (Figure 1). Thus, the Miocene faunas and ecosystems of this southern region have remained virtually unknown. Furthermore, none of the well-known Miocene fossil sites in the EARS provides evidence of eastern African coastal forests, a major ecosystem that may have played a key role in hominin origins and the evolution of several mammalian lineages (Joordens, Feibel, Vonhof, Schulp, & Kroon, 2019; Kingdon, 2003). Although the necessity of documenting new fossil sites in previously unknown areas is widely appreciated and advocated (Almécija et al., 2021; Cote, 2018), discovering entirely new paleontological areas is a rare event (d'Oliveira Coelho, Anemone, & Carvalho, 2021). Here we describe the first dentognathic specimens of fossil vertebrates discovered in the East African Rift of central Mozambique. The specimens derive from the Mazamba Formation on the eastern shoulder of the Urema Rift in Gorongosa National Park (GNP) (Figure 2) (Habermann et al., 2019). Cosmogenic nuclide dating presented here indicates that the Gorongosa paleontological localities are of Miocene age. These localities formed under estuarine conditions and represent the first samples of eastern African coastal woodlands and forests in the Miocene. The emerging fossil record from Gorongosa opens the possibility of testing, for the first time, key hypotheses about an expanding northeast-southwest arid corridor that would have isolated the eastern coastal forests from those in the central parts of Africa, and for exploring the importance of these processes for hominin origins (Kingdon, 2003). Gorongosa Park is now well known for its successful wildlife restoration project (Bouley, Paulo, Angela, Du Plessis, & Marneweck, 2021; Pringle, 2017; Stalmans, Massad, Peel, Tarnita, & Pringle, 2019), and these new paleontological sites in the park open a unique window on the fauna and environments of ancient Africa.

Brief history of vertebrate paleontological research in the Cenozoic of Mozambique

Until recently, the fossil record of Cenozoic vertebrates in Mozambique has been sparse. More than a century and a half ago, J. Kirk reported on fossil finds of mammals and

reptiles along the lower Zambezi River, but these were mixed with pottery and were likely to be recent, as they represented extant species (Kirk, 1864). In 1977, J. Harris briefly described a left upper premolar (P4) of the proboscidean *Deinotherium* found in coastal beach sands near Praia de Morrungulo, east of Massinga in Inhambane Province (Harris, 1977). This specimen is comparable in morphology and dimensions to Plio-Pleistocene *Deinotherium bozasi*, but the original provenance and geological context of the fossil is unknown. In 1998, a European speleological team surveyed the Cheringoma Plateau's karstic system in Sofala Province (Figure 2), and the results published by M. Laumanns (2001) describe a series of caves near and within GNP. Some of the caves were indicated to have sedimentary infilling and archaeological potential, but there was no mention of any fossil vertebrates. Based on these reports, M. Pickford undertook brief surveys south of Morrungulo in 2012, and of GNP in 2012 and 2013. He discovered well-preserved fossil wood at Menguere Hill (=Mhengere in Pickford's reports) (Figure 3) and found postcranial fragments of fossil mammals of uncertain taxonomic affinities north of the Muaredzi River (Pickford, 2012, 2013). According to Pickford, "The fossils are not well-preserved, and no teeth were found. Comparison with a wide range of mammals failed to provide definite identifications…" (Pickford, 2013: 8). At this time, J. Mercader and P. Sillén undertook archeological surveys of the Gorongosa region including some caves described by Laumanns (2001). They reported Holocene bones and teeth as well as Middle and Later Stone Age artifacts (Mercader & Sillén, 2013), but the bones illustrated by Mercader and Sillén are modern warthog, *Phacochoerus africanus*, and modern bush pig, *Potamochoerus larvatus*.

In 2014, Gorongosa National Park authorities invited S. Carvalho to form a long-term paleontological, archaeological, speleological, and primatological research project. Carvalho created the Paleo-Primate Project Gorongosa (PPPG), an international and interdisciplinary endeavor combining paleontological and primatological approaches aiming to understand the deep time evolutionary history of the region. A central goal of PPPG is the mentoring and training of Mozambican students in areas of paleontology, archaeology, and primatology. In 2016, PPPG initiated systematic surveys of potentially fossiliferous sites within GNP, both in open-air sedimentary exposures of the Mazamba Formation and in the karstic cave systems of the Cheringoma Plateau. PPPG surveyed the vertebrate localities identified by Pickford in 2013 and these yielded several fragmentary fossils. After extensive surveys in new areas during the 2016 field season, the team discovered the first localities with teeth of fossil mammals the southern rift. After four field seasons (2016-2019), PPPG had documented

hundreds of fossil vertebrates and fossil wood from 11 paleontological localities (Figure 3, Supporting Information Figure S1, Table 1). Some of these specimens are described below.

The Urema Graben and the Cheringoma Plateau

At the southern end of the EARS, the Urema Graben crosses GNP along an approximately north-south axis, with the Cheringoma Plateau on the east and Mount Gorongosa dominating the northwestern region (Figures 2 and 3). Mount Gorongosa was formed by a granitic intrusion during the Jurassic (Real, 1966), but the Urema Graben represents one of the youngest sections of the EARS and may have been formed as recently as the Plio-Pleistocene (Grantham, Marques, Wilson, Manhiça, & Hartzer, 2011; Macgregor, 2015). The eastern shoulder of the Urema Graben is the Cheringoma Horst, an uplifted block bounded by the Inhaminga Fault on the west between the Pungue and Zambezi Rivers (Flores, 1973). Several geological formations are exposed in the Cheringoma Plateau, including the Sena Formation (Cretaceous), the Grudja Formation (with late Cretaceous and early Tertiary levels), the Cheringoma Formation (Eocene nummulitic limestones), and the Mazamba Formation (Mazamba sands attributed to the Miocene) (Flores, 1973; GTK_Consortium, 2006; Real, 1966) (Figure 3). Karstification of the Eocene limestones produced the extensive cave system of the Cheringoma Plateau (Laumanns, 2001).

Previous geological surveys of the region have determined that Cenozoic marine deposits begin with the glauconitic sands of the Grudja Formation, with one sample yielding a potassium-argon date of 60 Ma (Flores, 1973). Eocene marine deposits continue with the Cheringoma Formation, a limestone sequence with a thickness of 70-80 m containing abundant nummulites, echinoids, bryozoans, and gastropods deposited in warm, shallow (neritic) waters. The marine invertebrates (e.g., species of the annelid *Tubulostium*) indicate a middle to upper Eocene age for the Cheringoma Formation (Grantham et al., 2011; GTK_Consortium, 2006; Lächelt, 2004; Real, 1966; Teale, 1923). These Paleocene and Eocene deposits of the Grudja and Cheringoma formations represent a marine transgression with shorelines migrating westward (Flores, 1973).

The sedimentary deposits overlying the Cheringoma Formation constitute the Mazamba Formation, named after exposures along the Mazamba River 25 km southwest of Inhaminga in the Cheringoma Plateau. At the type locality in the upper Mazamba River this formation attains 140 m in thickness (Flores, 1973; Real, 1966). These deposits are separated from the underlying Cheringoma Formation by a well-defined erosional unconformity

resulting from marine regression (Flores, 1973; Grantham et al., 2011). According to Flores (1973: 105), "There is an erosional unconformity between the Eocene and the Miocene, with no intervening Oligocene, indicating considerable uplift in post-Eocene-pre-Miocene times". In the 1968 geological map of Mozambique, the Mazamba Formation is divided into two members separated by a chert horizon (as reproduced in Tinley 1977). The lower member ("grés de cor púrpura", or purple clays/sands) (TT_{S1} in the 1968 geological map; Figure 3) is composed of purplish to reddish medium-grained argillaceous sands, which contain gastropods, bivalves, crustaceans, and foraminifera, and are interpreted to be littoral marine intercalated with deltaic deposits (Real, 1966). The upper member (TT_{S2}) is referred to as the Inhaminga beds ("camadas de Inhaminga"), composed of medium to coarse arkosic sands with some irregular conglomerate layers (Figure 3). Real (1966) considers the lower member to be of Miocene age and the upper member to be of late Miocene to Pliocene age, but the criteria used to reach this conclusion are not specified. Lächelt (2004: 146-155) states that "The Mazamba Formation, which consists of conglomerates and sands, is the most distinctive Miocene formation" and attributes the sequence to the lower Miocene, but then he states that the Mazamba Formation correlates laterally with the Inhaminga Purple Sands. Although there are some discrepancies and contradictions (see Supporting Information: Geological Issues), most previous descriptions focused on the geology of the Cheringoma region consider the lower part of the Mazamba Formation to be of Miocene age and the upper part of the sequence to extend into the Pliocene (Kristina Arvidsson, 2010; K. Arvidsson et al., 2011; Habermann et al., 2019; Laumanns, 2001; Pickford, 2013; Tinley, 1977). Thus, we use the term Mazamba Formation to refer to the Mazamba/Inhaminga sequence in the Cheringoma Horst, with two informal members, a lower member and an upper member separated by a chert horizon. In the field, we identified the nodular chert layer separating the lower and upper sequences and undertook geological and paleontological surveys of both lower and upper deposits.

The dating of these sedimentary sequences has been hampered by the lack of radio-isotopic age determinations. Neogene volcanism has been less intensively developed in the southern EARS than in regions to the north (e.g., Afar, Main Ethiopian Rift, Omo-Turkana Basin, Kenya Rift), and volcanic ash layers amenable to radiometric dating seem to be rare. A basaltic intrusion ~8 km northwest of the Cundué River cuts through the Grudja and Cheringoma Formations, and thus would be younger than the Eocene (Real, 1966). This basalt, however, has not been radiometrically dated. In a regional context, recent research on the Zambezi Delta by Ponte and colleagues has identified a major unconformity at the end of

the Oligocene related to uplift of the South African Plateau (Baby, Guillocheau, Boulogne, Robin, & Dall'Asta, 2018), with the 'Mazamba sands' deposited above this unconformity during the early Miocene (Aquitanian and Burdigalian stages) (Ponte et al., 2019). See Supporting Information: Geological Issues for further details.

Materials and Methods

During the 2016-2019 field seasons, the Paleo-Primate Project Gorongosa discovered and documented seven paleontological localities with fossil vertebrates: GPL-1, GPL-2, GPL-6, GPL-7, GPL-8, GPL-11, and GPL-12. Three additional localities have produced invertebrates only (GPL-3, GPL-9, and GPL-10), and two yielded *ex-situ* stone tools (GPL-4 and GPL-5). Menguere Hill, with abundant fossil wood, is the westernmost fossiliferous locality and it is not identified by a GPL number (Figure 3). These localities are listed in Table 1. This study provides new data and integrates several lines of evidence from the Mazamba Formation, including 1) sedimentology and depositional environments of the fossil localities, 2) radiometric age determinations based on cosmogenic nuclides, 3) stable isotopes from pedogenic carbonates, 4) paleobotanical remains, and 5) vertebrate paleontology. First, we consider each of these lines of evidence separately, emphasizing the materials, analytical methods, and results from each approach. We then synthesize, integrate, and discuss these approaches and their paleoenvironmental and evolutionary significance (for details of each methodological approach see Supporting Information).

Sedimentology and stratigraphy of the lower Mazamba Formation

Based on regional stratigraphic relationships, sedimentary facies, facies architecture, and the emerging fossil record, Habermann et al. (2019) interpreted the sedimentary successions of the lower member of the Mazamba Formation exposed in the study region as representing a paleoenvironmental mosaic of estuarine and riverine forest/woodland systems. Estuarine sequences accumulated prior to rifting as compound incised-valley fills on a low-gradient coastal plain following transgression, receiving continental sediment from source terranes west of today's Urema Graben (Habermann et al., 2019). The lower Mazamba successions at the southwestern paleontological sites (GPL-1, GPL-6, GPL-7, GPL-8, GPL-12, see Figure 3) are dominated by basal conglomeratic and sandy facies overlain by clayey sandstones to wackes and sandy clay and marlstone units (Figure 4). These successions are

interpreted as lowstand (fluvial) and transgressive (estuarine) assemblages, comprising alluvial channel, bay head delta, shallow central basin or swamp and fluvio-deltaic distributary channel facies from base to top. In contrast, the northeastern localities represent laterally correlative (GPL-9) as well as younger stratigraphic levels (GPL-2, GPL-3); they are sand-dominated and contain marine invertebrates and some fossil mammals. These successions are interpreted as transgressive highstand assemblages consisting of barrier, shore-face, and lagoonal shelf facies (Habermann et al., 2019).

GPL-1 and GPL-12 are the most fossiliferous localities (Supporting Information Figure S1). The sedimentary sequence of GPL-1 was described in detail by Habermann et al. (2019), and here we describe the sedimentary succession of GPL-12 (Figures 3 and 4). The gully sidewall at GPL-12 exposes a 3 m thick section comprising seven distinct sedimentary facies. Coarse, granule- and pebble-bearing quartz sandstones that are moderately cemented by carbonate and contain variable amounts of clay, clayclasts, mottling, and bioturbation form the base of the succession (Facies 1–3). Bedding, occasionally picked out by pebble stringers or abrupt vertical grain-size changes, is only poorly developed. A single cast of a fossil bivalve was found in Facies 2 close to the bottom of the section. Mottling, reddish discoloration, and clay-filled bioturbation casts, including *Thalassinoides* isp., are most common in Facies 2. This facies also yielded numerous vertebrate fossils, which, besides isolated teeth and bone fragments, includes mandibles from various taxa. Brown, sandy claystones with sand-filled bioturbation casts (Facies 4) follow above, which in turn are overlain by clayey sandstones of Facies 5 that represents the second level in the section with large fossil vertebrate remains. At and near the top surface of Facies 5, carbonate accumulated in the form of finely distributed powder, as small concretionary nodules, or as thin crusts, suggesting a disconformity surface. A thin band of olive-green to reddish waxy claystone follows next (Facies 6), which is overlain by medium-grained, well-sorted sandstones that are cross-bedded in places. In Figure 4 we present tentative correlations between localities based on lithological and sedimentological criteria.

Grain-size and sorting characteristics of the basal sandstones of Facies 1–3 suggest a fluvial depositional environment. The vertebrate, invertebrate, and trace fossils in this part of the succession, however, comprise terrestrial and potentially brackish or marine elements (bivalve in Facies 2 as well as *Thalassinoides* isp., most commonly produced by burrowing decapod crustaceans). The fossil remains thus refine paleoenvironmental inferences, suggesting fluvio-deltaic conditions, possibly in a river-dominated estuarine context (bay-head delta assemblage). Fossil preservation and abundance in Facies 2 may suggest high

sedimentation rates and relatively rapid burial, perhaps during a storm or flood event. Claystone units in the GPL-12 succession may indicate overbank or mudpond deposition in a fluvio-deltaic environment or may reflect a deepening trend so that estuarine muds formed under brackish to marginal marine conditions following transgression.

Cosmogenic nuclide dating

To establish a chronology for the Mazamba Formation we applied the authigenic $^{10}Be/^{9}Be$ cosmogenic nuclide dating method, hereafter referred to as atmospheric ^{10}Be dating, since the method is based on the atmospherically produced isotope ^{10}Be (Lebatard et al., 2010). We extracted 15 rock samples from continuous sections measured in the lower member of the Mazamba Formation at GPL-1, GPL-2, GPL-6, and GPL-12 (Figures 3 and 4). To obtain as unaltered and unweathered rocks as possible, samples were taken from freshly excavated trench or section walls. The most fossiliferous and best studied outcrops thus far, GPL-1 and GPL-12, are covered by six and five samples, respectively, that were collected from consecutively younger units present in each section. All sampling positions were documented by total station measurements. Supplementary Table S1 lists all samples collected for dating together with their paleoenvironmental context interpreted from the sedimentary record.

Besides sampling the sedimentary strata to be dated ("fossil samples"), atmospheric ^{10}Be dating requires sampling of sediments from modern environments ("modern samples") equivalent to those reconstructed from the sedimentary record to determine the initial authigenic ratio N_0 characteristic of the Gorongosa region (Lebatard et al., 2010; Lebatard et al., 2008). To obtain these modern sediment samples, of which we analyzed nine in this study (Supplementary Table S1), a range of environments was sampled, including the banks of three rivers descending from Mount Gorongosa (proximal fluvial settings), the banks of the Pungue and Urema Rivers and the shore of Lake Urema (medial fluvial and lacustrine settings), as well as several localities on the coast, including the Savane River estuary and another estuary northeast of Beira, the shores of which support extensive mangrove swamps and forests (distal coastal, estuarine, and mangrove forest settings). See Supporting Information: Cosmogenic Nuclide Dating for further details.

Atmospheric $^{10}Be/^{9}Be$ dating – results

The authigenic $^{10}Be/^{9}Be$ ratios measured for the modern sediment samples (ranging from 70.9 to 281 x 10^{-13}, Supplementary Table S2) are low compared to the range of authigenic $^{10}Be/^{9}Be$ ratios of recent surficial continental sediments in general (Graham, Ditchburn, & Whitehead, 2001; Šujan et al., 2016; Wittmann et al., 2012). Due to the dispersion of the obtained N_0 values (Supplementary Table S2), with a low statistical correlation value, the modern samples were grouped by depositional environments. Then, three scenarios were considered: (1) a direct modern sedimentary/environmental conditions equivalent, (2) a fully estuarine environmental equivalent, and (3) a sedimentary source equivalent. For the first computing (Table 2 part (1)), assuming that the lower Mazamba sediments were deposited in two main paleoenvironments, i.e., fluvio-deltaic and estuarine-lagoonal, we chose modern samples derived from an environmentally equivalent context. For the fossil fluvio-deltaic deposit samples (n=5) (Be18-Gor-GPL1NE-1, Be18-Gor-GPL1NE-2, Be18-Gor-GPL12-0.1, Be18-Gor-GPL12-1.1, and Be18-Gor-GPL12-4.1), data from the modern sample Be18-Bei-EstRi1-1 was used as the N_0 reference value to calculate depositional ages of 8.6 ± 0.2 Ma and 14.6 ± 0.3 Ma for the first two samples from the base of GPL-1NE. For samples from the basal and middle sections at GPL-12 (GPL12-0.1, -1.1, and -4.1), deposition ages of 17.1 ± 0.5 Ma, 19.5 ± 0.8 Ma, and 16.9 ± 0.6 Ma were calculated, respectively. By contrast, the modern estuarine context samples Be18-Bei-SavEst-1 and Be18-Bei-SavFor-1, for which a weighted mean $^{10}Be/^{9}Be$ ratio of 0.640 ± 0.034 x 10^{-8} was obtained, were used as N_0 reference material to calculate deposition ages for the remaining fossil samples (n = 10) that reflect estuarine-lagoonal conditions. Calculated ages for these samples, coming from middle to upper parts of the GPL-1 and GPL-12 sections, range between 6.9 ± 0.2 Ma (Be18-Gor-GPL1NE-6) and 17.8 ± 0.7 Ma (Be18-Gor-GPL1NE-5).

In the second computing (Table 2 part (2)), assuming the depositional environment for the lower Mazamba Formation was mainly estuarine, only the two modern estuarine context samples (Be18-Bei-SavEst-1 and Be18-Bei-SavFor-1) were considered for age calculations with a mean N_0 value of 0.64 ± 0.03 x 10^{-8}. In this scenario, calculated deposition ages range from 6.9 ± 0.2 Ma (Be18-Gor-GPL1NE-6) to 18.0 ± 0.8 Ma (Be18-Gor-GPL12-1.1) and only the resulting dates for the five fossil fluvio-deltaic samples change with respect to the first computing.

In the third computing (Table 2 part (3)), environmental conditions were largely irrelevant for the choice of modern reference samples. Instead, we chose modern samples for obtaining N_0 values (mainly for the dissolved ^{9}Be input sources) based on sampling localities

in the vicinity of the source rocks that the sediments are inferred to be primarily derived from (i.e., Gorongosa Suite granite and gabbro exposed at Mount Gorongosa; Habermann et al., 2019). Matching depositional environments of modern and fossil samples (in this case fluvial) were considered secondarily only in the selection process. The $^{10}Be/^{9}Be$ ratios obtained from three modern samples, one from the banks of the Urema River (Be18-Gor-Urem-1.1) and two from the banks of the Vunduzi River (Be18-Gor-Vun-1.1 and Be18-Gor-VunS1-1.1), were used to calculate a weighted mean N_0 value of $0.226 \pm 0.007 \times 10^{-8}$. This weighted mean value was then applied in age calculations to the lower Mazamba samples to be dated. In this approach, resulting ages prove to be slightly younger, ranging between 4.8 ± 0.2 Ma (Be18-Gor-GPL1NE-6) and 15.9 ± 0.8 Ma (Be18-Gor-GPL12-1.1). Thus, under the three different models, all but two of the samples yield dates within the time frame of the Miocene. The lower sections of GPL-12 yield the oldest dates and indicate that the sediments are of early Miocene age. The four samples from GPL-2 and GPL-6 provide late Miocene ages under the three different models. Further information is provided in Supporting Information.

Cosmogenic nuclide $^{26}Al/^{10}Be$ dating

The upper member of the Mazamba Formation has not yielded any fossils yet, and previous geological work indicates it is much younger than the lower member, but no radiometric dates have been previously reported. We applied the $^{26}Al/^{10}Be$ burial dating method based on the decay of ^{26}Al and ^{10}Be cosmogenic nuclides produced in situ in quartz (SiO_2) minerals (Lebatard et al., 2014; Lebatard, Bourlès, & Braucher, 2019; Pappu et al., 2011) to date samples from the upper member and thus provide chronological constraints on the fossiliferous lower member. In general, this technique is applicable for the time frame from 100 ka to ~6 Ma (Granger & Muzikar, 2001). We chose two rock samples collected from two detailed stratigraphic sections in the Mussapassua area in the southeastern corner of GNP where the upper member is well exposed. Under two different models, the samples yielded burial duration dates of ~1 Ma and indicate that at least part of the upper member is of early Pleistocene age. For analytical details, please see the Supporting Information: Cosmogenic Nuclide Dating as well as Supplementary Tables S3 and S4.

Pedogenic carbonates

Stable carbon ($\delta^{13}C$) and oxygen ($\delta^{18}O$) isotope values of 17 pedogenic carbonates from GPL-1 were used to infer regional paleovegetation and climate patterns during the formation of the fossil bearing sediments. $\delta^{13}C$ values serve as a robust and well-established tool to reconstruct past vegetation growing on the site following soil development. On a continental scale, different biomes differ in the $\delta^{13}C$ values of associated biomass. Dicots (trees, bushes, herbs) are primarily C_3 plants, whereas tropical grasses and sedges use the C_4 photosynthetic pathway and differ in their discrimination against $^{13}CO_2$ (Pearcy & Ehleringer, 1984). C_4 photosynthesis is typically prevalent in warm and seasonally dry, open conditions with high light intensity, whereas the C_3 pathway is advantageous under low water stress and at high-pCO_2 conditions. Due to a difference in their discrimination against ^{13}C during photosynthesis, $\delta^{13}C$ values of most C_4 plants range from -9 to -19 ‰, while those of C_3 plants lie between -25 and -29 ‰, resulting in $^{13}C/^{12}C$ ratios of tropical grasses and sedges ca. 14 ‰ higher than most trees, shrubs, bushes, and herbaceous plants (Cerling, Harris, Ambrose, Leakey, & Solounias, 1997). The comparably small variability of $\delta^{13}C$ in C_4 plants can be attributed to three different C_4 photosynthetic subpathways (Pearcy & Ehleringer, 1984), while the variation in $\delta^{13}C$ among C_3 plants is affected by a variety of environmental factors including trophic effect, precipitation, temperature, drought, canopy density, salinity, light intensity, nutrient levels, and partial pressure of CO_2 (Diefendorf, Mueller, Wing, Koch, & Freeman, 2010; Ehleringer & Monson, 1993; Farquhar, Ehleringer, & Hubick, 1989; Kohn, 2010; E. Medina & Minchin, 1980; Ernesto Medina, Montes, Guevas, & Rokzandic, 1986). Collectively, however, these effects on $\delta^{13}C$ of C_3 plants are still considerably small compared to the differences between C_3 and C_4 biomass. Pedogenic carbonate formed in equilibrium with soil-respired CO_2 is typically enriched in ^{13}C by 13.5 to 17.0 ‰ compared to the CO_2 which respired from plants or was released during decomposition of soil organic carbon and related organic matter (Cerling, 1984; Cerling, Wang, & Quade, 1993).

Pedogenic carbonate forms in oxygen isotope equilibrium with soil water (Cerling & Quade, 1993). The $\delta^{18}O$ value of soil carbonate is a function of soil water composition and temperature. Soil water is derived from meteoric water, but can differ from this source water due to enrichment through evaporation from the soil surface, mixing with (evaporatively ^{18}O-enriched) infiltrating water, and/or the addition of isotopically distinct water from overland and vadose zone flow (Hsieh, Chadwick, Kelly, & Savin, 1998). Nevertheless, $\delta^{18}O$ values of modern pedogenic carbonate have a strong positive correlation with the composition of meteoric water, which in turn has a positive correlation with local air temperature (Rozanski, Araguás-Araguás, & Gonfiantini, 1992). Collectively, this makes paleosol carbonate an

important paleoclimate proxy. The composition of local meteoric water has a large influence on $\delta^{18}O$ of soil water and hence pedogenic carbonate $\delta^{18}O$. Today, the climate of central Mozambique is a result of interactions between the African Monsoon, the Intertropical Convergence Zone, and the Zaire Air Boundary. These complex patterns complicate the comparison of absolute $\delta^{18}O$ values of distant localities, due to possibly different isotopic composition of local precipitation. See Supporting Information: Pedogenic Carbonates for methodological details.

Pedogenic carbonates – results

All results are listed in Table 3 and shown in Figure 5. Stable carbon isotope ratios of pedogenic carbonates of GPL-1 vary between -9.3 and -5.9 ‰ with an average value of -7.3 ± 1.0 ‰, while oxygen isotopes ratios fluctuate from 25.4 to 26.5 ‰ with an average of 25.9 ± 0.3 ‰. There is very low correlation between $\delta^{13}C$ and $\delta^{18}O$ present ($R^2 = 0.1$). Overall stratigraphic trends cannot be detected in either of the two datasets. Carbonate content of the nodules is generally >50 % with only one sample having a significantly lower carbonate content (16 %), but comparable isotopic values. The average carbonate content is 80 ± 20 %.

Carbon isotope values average -7.3 ± 1.0 ‰ and never exceed -5.9 ‰. Such low values are typical for C_3 dominated ecosystems characterized by woodland, bushland, or wooded grassland environment with a mix of C_3/C_4 vegetation. Following the vegetation classification of (White, 1983), this would indicate average woody cover of at least 50 % (for the average $\delta^{13}C$ value of -7.3 ‰), using the 'paleo-shade' proxy (Cerling et al., 2011). The oxygen isotopic values of pedogenic carbonates from the paleosols of GPL-1 show fluctuations of only 1.1 ‰ towards a relatively persistent climate with no large variation in temperature, source water supply or effects of evaporation. Without constraints on paleotemperature or ancient soil water oxygen isotopic composition, temporal and geographic variations in fossil soil carbonate $\delta^{18}O$ values can only be used to identify qualitative changes in climatic patterns, but the relatively low $\delta^{18}O$ values could indicate a mesic climate with high water supply, which is also supported by the sedimentology, geology and fossil faunal and floral assemblages of this costal riverine forest/woodland ecosystem (Habermann et al., 2019).

Paleobotany

At Menguere Hill, about 3.5 km west of GPL-1, there are large, silicified tree trunks (Figure 6) measuring up to 1.6 m in diameter, as well as scattered fragments of fossil wood, as noted by Pickford (2013) and described by Habermann et al. (2019). Menguere Hill rises 40 m above the surrounding landscapes and exposes a series of silicified limestone beds. During the 2016-2018 field seasons, we collected 41 specimens of well-preserved fossil wood for microscopic analysis of thin sections and here we present a preliminary taxonomic list and the paleoecological implications of the taxa. The Gorongosa sample includes the palm *Hyphaene* (Palmae, family Arecaceae), which is widespread in the humid, hot lowlands of tropical Africa. The most abundant taxon in the collection is *Entandrophragmoxylon* (African mahogany, family Meliaceae) (Figure 7). The modern genus *Entandrophragma* is restricted to tropical Africa, and some species can reach up to 60 m in height. We have previously reported the presence of *Terminalioxylon* (family Combretaceae) (Habermann et al., 2019), a genus that is most diverse in bushveld and savannas, and includes some mangrove species. There are also samples of *Zizyphus* (family Rhamnaceae), which is common along watercourses, and *Zanha* (family Sapindaceae), found in open woodland to dense ravines and riverine forests (Arbonnier, 2004; Beentje, 1994; Coates Palgrave, 2002). A further observation to note is that cross sections of the wood vessels indicate mesophytic trees that cannot tolerate water stress. We interpret the Menguere Hill succession as a correlative inland equivalent to the estuarine fossil sites farther to the east based on similar elevations (see Table 1) (Habermann et al., 2019).

Systematic paleontology

Here we describe several key specimens from the lower Mazamba Formation. Additional Gorongosa fossils have recently been excavated and are currently under preparation, curation, and study (see Supporting Information).

Class Chondrichthyes Huxley, 1880
Subclass Elasmobranchii Bonaparte, 1838
Order Carcharhiniformes Compagno, 1977
Family Carcharhinidae Jordan & Evermann, 1896
Genus *Galeocerdo* Müller & Henle, 1837
Referred specimens: PPG2017-P-121 from GPL-1, PPG2018-P-224 from GPL-1, PPG2019-P-126, 129, 176 from GPL-12

Galeocerdo aduncus Agassiz, 1843

Referred specimen: PPG2019-P-127 from GPL-12

Six specimens of shark teeth have been recovered from the Gorongosa sedimentary sequence. Four of these are fragmentary teeth from GPL-1 (PPG2017-P-121, PPG2018-P-224) and GPL-12 (PPG2019-P-126, PPG2019-P-127), and two are complete crowns and roots from GPL-12 (PPG2019-P-127, PPG2019-P-129) (Figure 8). For shark teeth we use the terminology of Türtscher et al. 2021. The following descriptions and analyses are based on the two complete teeth. One of these teeth (PPG2019-P-129), however, has some weathering on the apex that removed part of the distal cutting edge. The apex of the Gorongosa teeth is dominated by a primary cusp that leans distally. Serrations are present in the mesial cutting edge and the distal heel, but only lightly developed or absent along the apex. The mesial cutting edge has more than a dozen primary serrations that decrease in size away from the apex. The heel is relatively straight and with ~10 primary serrations decreasing in size distally. The serrations are simple (not compound), with only primary serrations visible (no secondary serrations). The outline of the mesial cutting edge has a distinct break between the apex and the rest of the serrated mesial cutting edge with two lines meeting at an obtuse angle (140° in PPG2019-P-127 and 155° in PPG2018-P-129). The length of the apex is one third or less of the length of the rest of the mesial cutting edge. The mesiodistal length of the tooth exceeds its height. The root is relatively thick, bilobate and well-arched, with the slightly asymmetrical lobes forming an obtuse angle. The six specimens differ in coloration, weathering, and preservation, and appear to represent distinct individuals deriving from two localities separated by ~700 m. In overall characteristics, the shark teeth have the cockscomb appearance typical of the genus *Galeocerdo*, tiger sharks.

To assess the taxonomic affinities of the Gorongosa shark specimens, we carried out a series of 2D morphometric analyses of the two complete specimens. We compiled a set of fossil shark photographs from the existing literature to obtain a suitable comparative sample of 600 specimens (Supplementary Table S5). From this comparative sample we used three datasets including: 1) all 600 specimens from four different genera (*Galeocerdo*, *Physogaleus*, *Carcharhinus*, and *Hemipristis*), 2) a subset of 547 specimens from species of *Galeocerdo* and *Physogaleus*, 3) a subset including 436 specimens from different species of the genus *Galeocerdo*. We carried out Principal Component Analyses (PCA) of these datasets followed by multi-group Linear Discriminant Analyses (LDA) to classify the Gorongosa

specimens into taxonomic categories (see Supporting Information: Morphometric Analysis: Chondrichthyes for methodological details).

The first PCA considering four genera of sharks shows that both Gorongosa specimens are located within the convex hulls of *Galeocerdo* (Figure 9A). In the second PCA, considering eight species of *Galeocerdo* and *Physogaleus*, Gorongosa B is located near the center of the *Galeocerdo aduncus* convex hull, whilst Gorongosa A is in a marginal position near the edges of *G. cuvier* and *G. capellini* (Figure 9B). In the third PCA, which considers only species of *Galeocerdo*, Gorongosa B is again near the center of the *G. aduncus* convex hull, whilst Gorongosa A is near the edges of *G. cuvier* and *G. capellini* (Figure 9C). The three LDA models using the Principal Components (PCs) that accounted for 90% of the variance of the sample clearly distinguishes among the taxonomic categories, displaying good performances with satisfactory classification results after cross-validation (Supplementary Table S6). When using the obtained discriminant functions to classify the Gorongosa fossil sharks into these taxonomic categories (as a way of assessing morphological affinities), they were robustly classified within the genus *Galeocerdo*. When classifying the fossils using the species categories, Gorongosa A was classified within *Galeocerdo cuvier*, whilst Gorongosa B was strongly categorized within *Galeocerdo aduncus*. The species *G. aduncus* has a temporal span from the Oligocene to the end of the Miocene, whilst the earliest record of the extant species *G. cuvier* is from the Middle Miocene (Soto Ovalle, 2016; Türtscher et al., 2021).

The size and morphology of the fragmentary teeth in the Gorongosa collection is consistent with those of the complete crowns, and we attribute all six specimens to the same genus. *Galeocerdo* upper and lower teeth are very similar, but they increase in breadth relative to height posteriorly. The teeth of juvenile tiger sharks have fewer serrations than those of adults (Türtscher et al., 2021). The Gorongosa fossil teeth are functionally similar to those of the extant tiger shark, and we may infer similar function in piercing large prey.

Batoidea Compagno, 1973
Order Myliobatiformes Compagno, 1973
Referred specimen: PPG2018-P-257 from GPL-1

A single fragment of batoid symphyseal teeth was found at GPL-1. This indicates that at least two taxa of cartilaginous fishes occur in the Gorongosa fossil record, one species of

shark and one species of ray. Most batoid species live in tropical and subtropical coastal waters, and some can occur in estuaries.

Order Testudines Batsch, 1788
Referred specimens: PPG2016-P-12, 13, 14, 27, 55, PPG2017-P-42, 44, 87, 95, PPG2018-P-10, 201, 203, 206, 217, 233, 234, 235, 270, 271

Family Testudinidae Batsch, 1788
Referred specimen: PPG2016-P-9

There are 20 specimens of turtles and tortoises in the Gorongosa fossil collections, which include fragments of carapace and plastron. One of the first specimens to be recovered in the field was PPG2016-P-9, a plastron fragment consistent in thickness and morphology with terrestrial tortoises (family Testudinidae) (Figure 10A), which have been present in Africa since the late Eocene (Holroyd & Parham, 2003; Zouhri et al., 2017). Most specimens are fragmentary but further analyses will aim to refine the taxonomic attributions.

Order Crocodylia Gmelin, 1789
Family Crocodylidae Cuvier, 1807
Crocodylidae indet.
Referred specimens: PPG2016-P-10, 23, PPGG2017-P-43, 49, 73, 80, 89, PPG2018-P-100, 161, 162, 222, 223, 241, 252, 264, PPG2019-P-116, 117, 128

There are 18 teeth and tooth fragments attributed to Crocodylidae. Their abundance attests to relatively stable bodies of water in the region. Tooth crown morphologies are consistent with size and shape heterodonty in brevirostrine taxa (Figure 10B) (D'Amore, Harmon, Drumheller, & Testin, 2019; Kieser, Klapsidis, Law, & Marion, 1993). Although represented by small sample sizes, maximum tooth crown lengths indicate body sizes similar to comparatively small-bodied crocodylids from the Paleogene and early to middle Miocene of North African and sub-Saharan formations (Brochu & Gingerich, 2000; Conrad et al., 2013; Cossette et al., 2020), as opposed to the gigantic late Miocene-Pleistocene taxa from East Africa (Brochu & Storrs, 2012; Storrs, 2003). A single broken, poorly preserved tooth is elongate and slightly recurved distally, similar to the condition in longirostrine, piscivorous

tomistomine and gavialoid taxa, suggesting the presence of at least two crocodylid taxa in the lower member of the Mazamba Formation.

Mammalia Linnaeus, 1758
Afrotheria Stanhope et al., 1998
Order Hyracoidea Huxley, 1869
Family Saghatheriidae Andrews, 1906
Referred specimens: PPG2018-P-1, 2

Hyraxes (order Hyracoidea) belong to the Afrotheria, a clade of mammals with deep evolutionary roots in Africa. There are five species of modern hyraxes, all in the family Procaviidae, but in the past there were at least four additional families: Geniohyidae, Saghatheriidae, Titanohyracidae, and Pliohyracidae. Hyracoids in the Paleogene of Africa were abundant and diverse, both taxonomically and functionally, but declined in overall diversity during the late Miocene (Rasmussen & Gutiérrez, 2010).

The Gorongosa sample includes an individual with left and right mandibular fragments (Figure 11) excavated in situ from Facies 2 at GPL-12 (Supporting Information Figure S1). The hyracoid mandibles represent some of the oldest mammals found so far in the Gorongosa sequence (early Miocene based on the atmospheric ^{10}Be dates). The left hemimandible (PPG2018-P-1) has the complete premolar-molar dentition, from p1 to m3, but the specimen is extremely fragile, so it remains in its plaster jacket for protection and only the buccal and occlusal aspects are visible. The right mandible fragment (PPG2018-P-2) has a complete set of molars (m1-m3) and two detached premolars (p3 and p4). Tooth measurements are given in Table 4. The mandibular body, as seen on the left side, shows a slight depression on the buccal side below the level of m1-m2. The cheek teeth increase monotonically in mesio-distal length from p1 (12.81 mm) to m3 (31.01 mm). The teeth are brachydont, and the molars are bilophodont with well-developed transverse crests. The posterior premolars, p3-p4, are molarized. In the molars, the protoconid is large and gives rise to the protocristid that extends to the metaconid and forms the mesial loph. The paraconid is reduced and the metaconid is the tallest cusp. The hypoconid gives rise to a marked hypocristid that extends to the entoconid and forms the distal loph. The m3 has a well-developed hypoconulid and a third loph joins the hypoconulid with the endoconulid. A continuous cingulum occurs along the mesial, buccal, and distal parts of the molars. The

well-developed transverse crests and the low-crowned molars of the Gorongosa specimens most likely indicate a folivorous diet based on soft leaves.

To compare the Gorongosa mandibles with those from other sites, we carried out a Principal Component Analysis of dental shape variables. For the left hemimandible (PPG2018-P-1) we used five curves with 15 landmarks each from the buccal side (given that the lingual side is obscured by the plaster jacket) to produce dental row outlines from p3 to m3 (Figure 12A). These landmarks were collected using the software Landmark Editor 3.6 (Wiley et al., 2005). We chose the p3-m3 sequence (excluding p1-p2) to maximize the number of comparative specimens that could be used. We obtained similar outlines from the 3D models of 14 hyracoids. Three of these comparative specimens are housed at the National Museums of Kenya (NMK) and were digitized using photogrammetry following the protocol described by Bucchi and colleagues (Bucchi, Luengo, Fuentes, Arellano-Villalón, & Lorenzo, 2020). Eleven additional comparative specimens were downloaded from Morphosource https://www.morphosource.org/ (Boyer, Gunnell, Kaufman, & McGeary, 2016) (Supplementary Table S7). This comparative sample included the genera *Saghatherium*, *Thyrohyrax*, *Megalohyrax*, *Afrohyrax* and the modern genera *Dendrohyrax* and *Procavia*. The first and last landmarks from each one of the five curves were treated as fixed (i.e., 10 fixed landmarks), whereas all the rest of them (i.e., 65 landmarks) were considered as semi-landmarks. See Supporting Information: Morphometric Analysis: Hyracoidea for further details. This PCA shows that the Gorongosa mandible is closer to specimens of Saghatheriidae (*Saghatherium*, *Thyrohyrax*, and *Megalohyrax*) than to Titanohyracidae (*Afrohyrax*) or modern Procaviidae (*Dendrohyrax* and *Procavia*) (Figure 12B), at least when considering the two first principal components (PCs) that account for ~70% of the variance of the sample.

In another analysis using only the m3 from mandible PPG2018-P-2, we used four curves with 10 landmarks each (Figure 13A). This dataset was then compared with the 3D models of 25 hyracoids. Thirteen of these specimens are also housed at the NMK and that were digitized using photogrammetry using the same protocol that was described above, whilst the rest of the sample was obtained from Morphosource https://www.morphosource.org/ (Supplementary Table S8). The comparative sample derives from five families of Hyracoidea: Geniohyidae (*Bunohyrax*), Saghatheriidae (Saghatherium, *Thyrohyrax*, *Megalohyrax*), Titanohyracidae (*Afrohyrax*, *Mereohyrax*), Pliohyracidae (*Parapliohyrax*), and Procaviidae (*Dendrohyrax* and *Procavia*). This dataset was also subjected to a General Procrustes Analysis (GPA) to obtain shape variables. The first and last

landmarks from each one of the four curves were treated as fixed (i.e., eight fixed landmarks), whilst the remaining 3D coordinates (i.e., 32 landmarks) were considered as semi-landmark and were slid by using Procrustes distance minimization as criterion. The obtained shape residuals were then used to carry out a PCA. This PCA shows that the Gorongosa m3 is closer to specimens of Saghatheriidae than to those of other families (Figure 13B), at least when considering the first two PCs that account for ~64% of the variance of the sample. Although most similar to the genus *Megalohyrax*, the Gorongosa specimen does not fully match any of the known taxa within this genus and represents a new species that we are fully describing in a separate manuscript.

Order Primates *inc. sed.* Linnaeus, 1758
Suborder Anthropoidea Mivart, 1864
Infraorder Catarrhini Geoffroy, 1812
Referred specimen: PPG2017-P-126

A single fossil specimen, PPG2017-P-126, was found at GPL-7. This specimen is a left maxillary fragment preserving part of the alveolar process, the malar process, and part of the zygomatic bone (Figure 14). The zygomatic process of the maxilla is broad and horizontal in orientation, unlike the condition usually observed in catarrhine primates. It extends 24 mm from the alveolar process to its lateral end. Laterally the maxilla-zygomatic suture is preserved. The superior aspect of the malar process preserves an area with cortical bone surface that may be the inferior floor of the orbit or an infraorbital canal (Figure 14). In addition, the posterior aspect of this bone is curved, and the cortical bone surface is preserved. Inspection of the microCT scans does not reveal any presence of the floor of a maxillary sinus which, among African catarrhine primates, is present only in hominoids and macaques (Rae & Koppe, 2004). If present, the maxillary sinus would be located above the root apices and could expand into the zygomatic bone. In contrast and worth noting, the cancellous bone of both the alveolar and zygomatic bones is quite dense and compact, while some of the cancellous bone pores around the root apices appear to be filled in with sediment (Figure 15).

The tooth crowns are missing, but the alveolar process preserves a series of roots below the furcation, which we interpret as a premolar-molar sequence (Figure 16A and 16B). On the mesial end, a portion of the distal wall of the palatal root of the P3 is still present, while the first set of 3 roots represents a P4, with two buccal roots (the mesio-buccal one is

broken) and one palatal root. The second set of 3 roots is M1, again with two buccal roots and one palatal root. The third set of 3 roots is M2, with two buccal roots and a broken palatal root. Distally, there is a small fragment of root encased in sediment that is part of M3. In P4-M2 the lingual root is placed symmetrically between the two buccal roots forming an approximately equilateral triangle. In cross-section it is gutter-shaped along its buccal aspect. The root canals are elliptical in cross-section and relatively small for the dentine present, when compared to a sample of East and South African Miocene and Plio-Pleistocene catarrhine primates. The distal root of M2 has a smaller diameter than the other molar roots. The base of the zygomatic process of the maxilla extends from the P4-M1 junction anteriorly to M3 posteriorly. The mesiodistal length from the mesial root of P4 to the distal root of M2 is 24 mm. The maximum mesiodistal length of M1 at the roots is 8 mm, and the maximum buccolingual width is 9 mm. The overall morphology of the maxillary roots and their cross-sectional shape suggest that the specimen may belong to an anthropoid primate, as noted below.

To better assess the morphological affinities of this specimen, we carried out geometric morphometric analyses of the roots. It has been shown that different primate species exhibit distinct tooth root morphologies and that the analysis of tooth root cross-sectional shape is diagnostic both in terms of designating taxonomic status and determining position within the tooth row (Kullmer et al., 2011; Kupczik, 2003; Kupczik & Dean, 2008; Kupczik, Delezene, & Skinner, 2019; Kupczik & Hublin, 2010; Kupczik, Toro-Ibacache, & Macho, 2018). Even though the available morphology is too fragmentary to properly ascribe PPG2017-P-126 to a low taxonomic level, there is enough information to assess its possible primate status, as well as to carry out preliminary phenetic comparisons. Hence, we analyzed the M1 cross-sectional shape, as it corresponds to the most complete set of tooth roots available. We assembled a comparative sample comprising the CT-stacks of several different extinct and extant primates (Supplementary Table S9 and Figure 17). To obtain comparable root outlines, we manually selected the cross-sectional slices that were at the same level as the exposed roots of PPG2017-P-126 for each one the comparative specimens. Then, 30 equidistant 2D semi-landmarks were collected along the outlines of each one of the three roots available for M1, which resulted in a total of 90 2D coordinates (see Supporting Information: Morphometric Analysis: Primates, and Figure 18A). The first landmark of each one of three root outlines (i.e., landmarks 1, 31 and 61) were treated as fixed, and these were defined as the most lingual points for each one of the M1's root outlines. All the rest of the 2D coordinates (i.e., 87 landmarks) were considered as semi-landmarks. We computed the

multivariate mean shape of the sample using the obtained shape variables and the Procrustes distances between this average M1 root shape and each one of the specimens under analysis was calculated (Figure 18B). We plotted all specimens ordered by their Procrustes distance from the mean shape. The median distance (unbroken line) and upper quartile (dashed lines) summarize the distances from the mean shape. The most distinct morphologies are those represented by the papionins present in our sample (*Papio angusticeps* and *Theropithecus oswaldi*). They are the only specimens above the upper quartile in our sample and that could be considered as 'morphological outliers' in our analysis. PPG2017-P-126 is close to the median, thus exhibiting an M1 root cross-sectional shape that is not unusual for catarrhine primates. In addition, we used the obtained shape variables to perform a PCA. This PCA shows that the PPG2017-P-126 is closer to *Cercopithecoides williamsi*, *Simiolus enjessi*, and some chimpanzees (Figure 18C), at least when considering the two first principal components (PCs) that account for ~62% of the variance of the sample. PPG2017-P-126 is located between the Cercopithecoidea and Hominoidea along PC1, whilst along PC2 it shows values like some chimpanzees and some orangutans. Based on these results, we suggest that the root anatomy of PPG2017-P-126 shows primate affinities as observed in species of Catarrhini.

Discussion and conclusions

The new fossil sites from Gorongosa National Park open an entirely new vista on a region of Africa that, until now, had remained paleontologically unknown until now (Figures 1 and 2). No other sites along the East African Rift System yield the combination of fossil woods (e.g., African mahogany), marine invertebrates (crabs, gastropods, bivalves), marine vertebrates (sharks and rays), and terrestrial mammals (e.g., hyracoids). The geological, sedimentological, paleobotanical, geochemical, and paleontological evidence indicates that the Gorongosa fossil sites formed in coastal settings, even though today these sites are ~95 km from the coast and at ~100-120 m above sea level (Figures 3 and 4).

The new fossils derive from multiple sedimentary beds across ten paleontological localities in the lower member of the Mazamba Formation. Previous geological work assigned this sedimentary sequence broadly to the Miocene (Real, 1966, Flores, 1973, Tinley, 1976), but no radiometric dates had been obtained prior to our work. Here we have presented the first atmospheric beryllium dates for the Mazamba Formation (Table 4). Atmospheric beryllium samples from the lower member range in age from the early to the late Miocene and confirm the broad placement of this part of the sequence in the Miocene. Two samples

from the lowermost sections of GPL-12 provide an early Miocene age for the fluvio-deltaic sediments from which some key fossils derive. Atmospheric beryllium samples from GPL-2, which we expect to be younger based on our tentative correlations (Figures 3 and 4), indicate a late Miocene age for those sediments (Table 4). Thus, the dates obtained so far indicate that the new fossils derive from different intervals of the Miocene, but further applications of different dating techniques are needed to corroborate the chronology suggested by the atmospheric ^{10}Be method.

The sedimentological, isotopic, paleobotanical, and paleontological evidence presented here indicates that the fossil sites formed in coastal woodlands/forests or estuarine conditions. At GPL-1, for example, paleosol carbon and oxygen isotopes indicate the prevalence of C_3 vegetation (trees, shrubs) with some areas of grassland under mesic climate with a high supply of fresh water (Figure 5). This view is supported by the fossil wood (Figure 6), whose most abundant component is *Entandrophragmoxylon* (African mahogany) (Figure 7), a genus that typically grows in areas of high rainfall. There were also palm trees of the genus *Hyphaene*, which are widespread in the humid, hot lowlands with high water tables of tropical Africa today. Other trees in the ancient Gorongosa landscapes include *Terminalioxylon*, which includes some mangrove species, *Zizyphus*, which is common along the edges of watercourses, and *Zanha*, a genus associated with open woodland to dense ravines and riverine forests. Cross sections of the fossil wood vessels indicate the presence of mesophytic trees that cannot tolerate water stress. Thus, these different lines of evidence indicate that terrestrial environments near the coast were consistently warm and wooded, with a prevalence of C_3 vegetation under mesic conditions.

The rivers descending from the west meandered on a low gradient coastal plain, where they gave rise to estuaries near shallow marine environments (Habermann et al., 2019). Sharks of the genus *Galeocerdo* (Figures 8, 9) were top predators in these estuaries and nearshore environments. Specimens of *Galeocerdo* are known from the Eocene to the present (Türtscher et al., 2021), whilst the species *G. aduncus*, present in the Gorongosa sample, has a temporal range from the Oligocene to the late Miocene (Soto Ovalle, 2016; Türtscher et al., 2021). The genus was widely distributed in the tropical and temperate seas of the Miocene, with specimens found in Madagascar (Andrianavalona et al., 2015), North Africa (Argyriou et al., 2015; Cook, Murray, Simons, Attia, & Chatrath, 2010), Oceania (Fitzgerald, 2004), Eurasia (Marsili, Carnevale, Danese, Bianucci, & Landini, 2007; Villafaña et al., 2020), and the Americas (Carrillo-Briceño, Maxwell, Aguilera, Sánchez, & Sánchez-Villagra, 2015; Landini et al., 2017). Modern *Galeocerdo* ranges from pelagic waters to nearshore

environments in tropical and subtropical marine ecosystems, often occurring in river estuaries. Tiger sharks are top predators, with a diet of cephalopods, fish, turtles and other vertebrates (Cortés, 1999). Like the modern tiger sharks, *Galeocerdo* in the past was a highly mobile apex predator that played a major role in structuring coastal ecosystems (Dicken et al., 2017). The presence of these shark fossils in the Miocene of GNP is consistent with our interpretation of estuarine depositional environments (Habermann et al., 2019).

The fossil mammals analyzed here include species of Hyracoidea and Primates. Undoubtedly this is an incomplete list of the taxonomic diversity of Gorongosa fossil mammals, as many of the specimens were only recently excavated and are still under curation and analysis. Hyraxes (order Hyracoidea) belong to the Afrotheria, a clade of mammals with deep evolutionary roots in Africa. There are five species of modern hyraxes, all in the family Procaviidae, but in the past there were at least four additional families: Geniohyidae, Saghatheriidae, Titanohyracidae, and Pliohyracidae. Hyracoids in the Paleogene of Africa were abundant and diverse, both taxonomically and functionally, but declined in overall diversity during the late Miocene (Rasmussen & Gutiérrez, 2010). The chewing teeth of the Gorongosa hyracoid are brachydont and bilophodont, very likely for a diet of relatively soft leaves. The Gorongosa hyracoids represent a very large species with affinities to taxa in the family Saghatheriidae, but different from currently known species (Figures 11, 12, 13). The family Saghatheriidae includes the genera *Microhyrax*, *Saghatherium*, *Selenohyrax*, *Thyrohyrax*, *Megalohyrax*, and *Regubahyrax* spanning from the Eocene to the early Miocene. Specimens of *Regubahyrax* from the early Miocene of Libya document the latest known occurrence of saghatheriids (Pickford, 2009). The lower molars of *Regubahyrax* have well-developed cristids and spurs (Pickford, 2009), but the spurs are not developed in the Gorongosa hyracoid. Although most similar to the genus *Megalohyrax*, the Gorongosa specimen does not fully match any of the known taxa within this genus and represents a new species that we are fully describing in a separate manuscript (Bobe et al. in preparation).

Catarrhine primates also occurred in the ancient Gorongosa landscapes (Figures 14-18). The available morphology of the Gorongosa specimen (PPG2017-P-126) is too fragmentary to ascribe it to a low taxonomic level, but our comparisons of the molar root cross-sectional shape show that PPG2017-P-126 is not unusual for catarrhine primates. Our analyses of the Gorongosa specimen place it close to the primates *Cercopithecoides williamsi*, *Simiolus enjessi*, and some chimpanzees. Thus, conservatively, we assign this specimen to an indeterminate species of catarrhine. Paleogene and early Neogene African primates are associated with wooded or forested environments.

The fossils documented here represent the first descriptions of a substantial fossil record that is just emerging. The Gorongosa paleontological record opens up the possibility of testing important hypotheses about the role of the eastern coastal forests in shaping the evolution of African mammals (Joordens et al., 2019; Kingdon, 2003). As the fossil record from Gorongosa is further described and analyzed, it will yield a potent database spanning different intervals of the Miocene, which will then be compared to other sites on the continent. Thus we will be able to assess the effects of the northeast-southwest arid corridor in promoting the geographic isolation and evolutionary trajectories of coastal forest plant and animal communities in the past (Morley & Kingdon, 2013). The Gorongosa fossil record points to the persistence of woodlands and wooded grasslands along the southeastern coast of Africa during the Miocene, but further work is needed to assess the taxonomic affinities of the Gorongosa mammals with contemporaneous faunas elsewhere in Africa.

After four field seasons (2016-2019), extensive surveys, and new approaches in the search of paleontological sites (d'Oliveira Coelho et al., 2021), the Paleo-Primate Project Gorongosa has 1) documented ten new paleontological localities, 2) established a preliminary stratigraphic and sedimentological framework for the fossil sites (Habermann et al., 2019), 3) provided the first radiometric age determinations for the Mazamba Formation, 4) provided the first reconstructions of past vegetation in the region based on pedogenic carbonates and fossil wood, and 5) described the first fossil teeth from the southern East African Rift System. The Gorongosa sample includes new species of fossil mammals, and a unique combination of fossil specimens straddling the terrestrial/marine biomes. The Gorongosa fossil sites provide the first evidence of persistent woodlands and forests on the coastal margins of southeastern Africa during the Miocene.

Acknowledgements

We are deeply thankful to Greg Carr for his visionary approach to preserving the Gorongosa ecosystem, and for vital support to the Paleo-Primate Project Gorongosa. Research permits were granted by the Direcção Nacional do Património Cultural, Mozambique, with the support of professors Hilário Madiquida and Solange Macamo of Eduardo Mondlane University. We are very grateful to Gorongosa National Park, the Park Warden Pedro Muagura, the *fiscais* who provide support, and the Park staff, including Vasco Galante and Patricia Álvares da Guerra. We appreciate the help with logistics provided by Jason Denlinger and Tongai Castigo. We thank Katarina Almeida-Warren, Robert Anemone, Ana Gledis da Conceição, Gabriela Curtiz, Celina Dias, Katherine Elmes, Roberto Mussibora, Inês Sevene, and students from the Oxford-Gorongosa Paleo-Primate Field School who took part in the excavations and other aspects of field research. Pepson Makanela

prepared and curated specimens while providing training to Mozambican students. We thank S. Adnet, B. Beatty, R. Bernor, C. Brochu, D. Domning, M. Fortelius, D. Geraads, F. Guillocheau, T. Harrison, J. Hutchinson, C. Peters, M. Pickford, C. Robin, C. Robinson, K. Stewart, and W. Sanders for insightful discussions about PPPG research. For access to CT scans of and scanning assistance with the comparative primate fossil specimens we thank the Department of Earth Science, National Museums of Kenya, J.-J. Hublin (Max Planck Institute for Evolutionary Anthropology, Leipzig) E. Mbua, F. Spoor, M. Skinner and H. Temming. For access to the tomographic scan data of South African primate fossil specimens via MorphoSource, we thank Ditsong National Museum of Natural History and J. Adams of the Department of Anatomy and Developmental Biology, Monash University. L. Léanni assisted with chemical treatments and ICP-OES measurements in the LN2C laboratories (Cosmogenic Nuclides French National Laboratory, CEREGE, Aix-en-Provence). The ^{10}Be and ^{26}Al measurements were performed at the ASTER AMS national facility (CEREGE) which is supported by the INSU/CNRS, the ANR through the "Projets thématiques d'excellence" program for the "Equipements d'excellence" ASTER-CEREGE action, IRD. We thank the National Geographic Society for grants to S. Carvalho (NGS-57285R), R. Bobe (NGS-51140R-18), T. Lüdecke and J. Habermann (NGS-51478R). M. Bamford acknowledges funding from PAST (Palaeontological Scientific Trust, South Africa). T. Püschel was funded by the Leverhulme Trust Early Career Fellowship, ECF-2018-264. J. d'Oliveira Coelho was funded by the Portuguese Foundation for Science and Technology (FCT) Grant SFRH/BD/122306/2016.

Bibliography

Almécija, S., Hammond, A. S., Thompson, N. E., Pugh, K. D., Moyà-Solà, S., & Alba, D. M. (2021). Fossil apes and human evolution. *Science, 372*(6542), eabb4363. doi:10.1126/science.abb4363

Andrianavalona, T. H., Ramihangihajason, T. N., Rasoamiaramanana, A., Ward, D. J., Ali, J. R., & Samonds, K. E. (2015). Miocene shark and batoid fauna from Nosy Makamby (Mahajanga Basin, northwestern Madagascar). *PLoS ONE, 10*(6), e0129444. doi:10.1371/journal.pone.0129444

Arbonnier, M. (2004). *Trees, shrubs, and lianas of West African dry zones*. Paris: CIRAD, Margraf Publishers Gmbh, MNHN.

Argyriou, T., Cook, T. D., Muftah, A. M., Pavlakis, P., Boaz, N. T., & Murray, A. M. (2015). A fish assemblage from an early Miocene horizon from Jabal Zaltan, Libya. *Journal of African Earth Sciences, 102*, 86-101. doi:https://doi.org/10.1016/j.jafrearsci.2014.11.008

Arvidsson, K. (2010). *Geophysical and hydrogeological survey in a part of the Nhandugue River valley, Gorongosa National Park, Mozambique: area 2 and 3.* (Master's), Lund University, Lund.

Arvidsson, K., Stenberg, L., Chirindja, F., Dahlin, T., Owen, R., & Steinbruch, F. (2011). A hydrogeological study of the Nhandugue River, Mozambique – A major groundwater recharge zone. *Physics and Chemistry of the Earth, Parts A/B/C, 36*(14–15), 789-797. doi:http://dx.doi.org/10.1016/j.pce.2011.07.036

Baby, G., Guillocheau, F., Boulogne, C., Robin, C., & Dall'Asta, M. (2018). Uplift history of a transform continental margin revealed by the stratigraphic record: The case of the Agulhas transform margin along the Southern African Plateau. *Tectonophysics, 731-732*, 104-130. doi:https://doi.org/10.1016/j.tecto.2018.03.014

Beentje, H. J. (1994). *Kenya trees, shrubs and lianas*. Nairobi: National Museums of Kenya.

Bouley, P., Paulo, A., Angela, M., Du Plessis, C., & Marneweck, D. G. (2021). The successful reintroduction of African wild dogs (*Lycaon pictus*) to Gorongosa National Park, Mozambique. *PLoS ONE, 16*(4), e0249860. doi:10.1371/journal.pone.0249860

Boyer, D. M., Gunnell, G. F., Kaufman, S., & McGeary, T. M. (2016). Morphosource: Archiving and sharing 3-D digital specimen data. *The Paleontological Society Papers, 22*, 157-181. doi:10.1017/scs.2017.13

Brochu, C. A., & Gingerich, P. D. (2000). New tomistomine crocodylian from the middle Eocene (Bartonian) of Wadi Hitan, Fayum Province, Egypt. *Contributions from the Museum of Paleontology, The University of Michigan, 30*(10), 251-268.

Brochu, C. A., & Storrs, G. W. (2012). A giant crocodile from the Plio-Pleistocene of Kenya, the phylogenetic relationships of Neogene African crocodylines, and the antiquity of Crocodylus in Africa. *Journal of Vertebrate Paleontology, 32*(3), 587-602. doi:10.1080/02724634.2012.652324

Bucchi, A., Luengo, J., Fuentes, R., Arellano-Villalón, M., & Lorenzo, C. (2020). Recommendations for improving photo quality in close-range photogrammetry, exemplified in hand bones of chimpanzees and gorillas. *International Journal of Morphology, 38*(2), 348-355.

Carrillo-Briceño, J. D., Maxwell, E., Aguilera, O. A., Sánchez, R., & Sánchez-Villagra, M. R. (2015). Sawfishes and other elasmobranch assemblages from the Mio-Pliocene of the south Caribbean (Urumaco sequence, northwestern Venezuela). *PLoS ONE, 10*(10), e0139230. doi:10.1371/journal.pone.0139230

Cerling, T. E. (1984). The stable isotopic composition of modern soil carbonate and its relationship to climate. *Earth and Planetary Science Letters, 71*, 229-240.

Cerling, T. E., Harris, J. M., Ambrose, S. H., Leakey, M. G., & Solounias, N. (1997). Dietary and environmental reconstruction with stable isotope analyses of herbivore tooth enamel from the Miocene locality of Fort Ternan, Kenya. *Journal of Human Evolution, 33*(6), 635-650.

Cerling, T. E., & Quade, J. (1993). Stable carbon and oxygen isotopes in soil carbonates. In P. K. Swart, K. C. Lohmann, J. McKenzie, & S. Savin (Eds.), *Climate change in continental isotopic records* (Vol. Geophysical Monograph 78, pp. 217-231). Washington DC: The American Geophysical Union.

Cerling, T. E., Wang, Y., & Quade, J. (1993). Expansion of C4 ecosystems as an indicator of global ecological change in the Late Miocene. *Nature, 361*, 344-345.

Cerling, T. E., Wynn, J. G., Andanje, S. A., Bird, M. I., Korir, D. K., Levin, N. E., . . . Remien, C. H. (2011). Woody cover and hominin environments in the past 6 million years. *Nature, 476*, 51-56.

Coates Palgrave, M. (2002). *Keith Coates Palgrave Trees of Southern Africa*. Cape Town: Struik Publishers.

Conrad, J. L., Jenkins, K., Lehmann, T., Manthi, F. K., Peppe, D. J., Nightingale, S., . . . McNulty, K. P. (2013). New specimens of 'Crocodylus' pigotti (Crocodylidae) from Rusinga Island, Kenya, and generic reallocation of the species. *Journal of Vertebrate Paleontology, 33*(3), 629-646. doi:10.1080/02724634.2013.743404

Cook, T. D., Murray, A. M., Simons, E. L., Attia, Y. S., & Chatrath, P. (2010). A Miocene selachian fauna from Moghra, Egypt. *Historical Biology, 22*(1-3), 78-87. doi:10.1080/08912960903249329

Cortés, E. (1999). Standardized diet compositions and trophic levels of sharks. *ICES Journal of Marine Science, 56*(5), 707-717. doi:10.1006/jmsc.1999.0489

Cossette, A. P., Adams, A. J., Drumheller, S. K., Nestler, J. H., Benefit, B. R., McCrossin, M. L., . . . Brochu, C. A. (2020). A new crocodylid from the middle Miocene of Kenya

and the timing of crocodylian faunal change in the late Cenozoic of Africa. *Journal of Paleontology, 94*(6), 1165-1179. doi:10.1017/jpa.2020.60
Cote, S. (2018). Savannah savvy. *Nature Ecology & Evolution, 2*(2), 210-211. doi:10.1038/s41559-017-0450-x
D'Amore, D. C., Harmon, M., Drumheller, S. K., & Testin, J. J. (2019). Quantitative heterodonty in Crocodylia: assessing size and shape across modern and extinct taxa. *PeerJ, 7*, e6485. doi:10.7717/peerj.6485
d'Oliveira Coelho, J., Anemone, R. L., & Carvalho, S. (2021). Unsupervised learning of satellite images enhances discovery of late Miocene fossil sites in the Urema Rift, Gorongosa, Mozambique. *PeerJ, 9*, e11573. doi:10.7717/peerj.11573
Dicken, M. L., Hussey, N. E., Christiansen, H. M., Smale, M. J., Nkabi, N., Cliff, G., & Wintner, S. P. (2017). Diet and trophic ecology of the tiger shark (*Galeocerdo cuvier*) from South African waters. *PLoS ONE, 12*(6), e0177897. doi:10.1371/journal.pone.0177897
Diefendorf, A. F., Mueller, K. E., Wing, S. L., Koch, P. L., & Freeman, K. H. (2010). Global patterns in leaf 13C discrimination and implications for studies of past and future climate. *Proceedings of the National Academy of Sciences, 107*(13), 5738. doi:10.1073/pnas.0910513107
Ehleringer, J. R., & Monson, R. K. (1993). Evolutionary and ecological aspects of photosynthetic pathway variation. *Annual Review of Ecology and Systematics, 24*(1), 411-439. doi:10.1146/annurev.es.24.110193.002211
Farquhar, G. D., Ehleringer, J. R., & Hubick, K. T. (1989). Carbon isotope discrimination and photosynthesis. *Annual Review of Plant Physiology and Plant Molecular Biology, 40*(1), 503-537. doi:10.1146/annurev.pp.40.060189.002443
Fitzgerald, E. M. G. (2004). A review of the Tertiary fossil Cetacea (Mammalia) localities in Australia. *Memoirs of Museum Victoria, 61*(2), 183-208.
Flores, G. (1973). The Cretaceous and Tertiary sedimentary basins of Mozambique and Zululand. In G. Brant (Ed.), *Sedimentary basins of the African coasts* (Vol. 2: South and east coasts, pp. 81-111). Paris: IUGS.
Graham, I. J., Ditchburn, R. G., & Whitehead, N. E. (2001). Be isotope analysis of a 0–500ka loess–paleosol sequence from Rangitatau East, New Zealand. *Quaternary International, 76-77*, 29-42. doi:https://doi.org/10.1016/S1040-6182(00)00087-2
Granger, D. E., & Muzikar, P. F. (2001). Dating sediment burial with in situ-produced cosmogenic nuclides: theory, techniques, and limitations. *Earth and Planetary Science Letters, 188*(1), 269-281. doi:https://doi.org/10.1016/S0012-821X(01)00309-0
Grantham, G. H., Marques, J. M., Wilson, M. G. C., Manhiça, V., & Hartzer, F. J. (2011). *Explanation of the geological map of Mozambique, scale 1:1 000 000*: Direcção Nacional de Geologia Moçambique.
GTK_Consortium. (2006). *Map Explanation, Volume 2: Sheets 1630-1934. Geology of Degree Sheets Mecumbura, Chioco, Tete, Tambara, Guro, Chemba, Manica, Catandica, Gorongosa, Rotanda, Chimoio and Beira, Mozambique*. Maputo: National Directorate of Geology, Republic of Mozambique.
Habermann, J. M., Alberti, M., Aldeias, V., Alemseged, Z., Archer, W., Bamford, M., . . . Carvalho, S. (2019). Gorongosa by the sea: First Miocene fossil sites from the Urema Rift, central Mozambique, and their coastal paleoenvironmental and paleoecological contexts. *Palaeogeography, Palaeoclimatology, Palaeoecology, 514*, 723-738. doi:https://doi.org/10.1016/j.palaeo.2018.09.032
Harris, J. M. (1977). Deinotheres of southern Africa. *South African Journal of Science, 73*, 281-282.

Holroyd, P. A., & Parham, J. F. (2003). The antiquity of African tortoises. *Journal of Vertebrate Paleontology, 23*(3), 688-690.
Hsieh, J. C. C., Chadwick, O. A., Kelly, E. F., & Savin, S. M. (1998). Oxygen isotopic composition of soil water: Quantifying evaporation and transpiration. *Geoderma, 82*(1), 269-293. doi:https://doi.org/10.1016/S0016-7061(97)00105-5
Joordens, J. C. A., Feibel, C. S., Vonhof, H. B., Schulp, A. S., & Kroon, D. (2019). Relevance of the eastern African coastal forest for early hominin biogeography. *Journal of Human Evolution, 131*, 176-202. doi:https://doi.org/10.1016/j.jhevol.2019.03.012
Kieser, J. A., Klapsidis, C., Law, L., & Marion, M. (1993). Heterodonty and patterns of tooth replacement in Crocodylus niloticus. *Journal of Morphology, 218*(2), 195-201. doi:https://doi.org/10.1002/jmor.1052180208
Kingdon, J. (2003). *Lowly origin: When, where, and why our ancestors first stood up*. Princeton: Princeton University Press.
Kirk, J. (1864). On a few fossil bones from the alluvial strata of the Zambesi Delta. *The Journal of the Royal Geographical Society of London, 34*, 199-201. doi:10.2307/1798473
Kohn, M. J. (2010). Carbon isotope compositions of terrestrial C3 plants as indicators of (paleo)ecology and (paleo)climate. *Proceedings of the National Academy of Sciences, 107*(46), 19691-19695. doi:10.1073/pnas.1004933107
Kullmer, O., Sandrock, O., Kupczik, K., Frost, S. R., Volpato, V., Bromage, T. G., & Schrenk, F. (2011). New primate remains from Mwenirondo, Chiwondo Beds in northern Malawi. *Journal of Human Evolution, 61*(5), 617 - 623. doi:10.1016/j.jhevol.2011.07.003
Kupczik, K. (2003). *Tooth root morphology in primates and carnivores.* (PhD), University College London, London.
Kupczik, K., & Dean, M. C. (2008). Comparative observations on the tooth root morphology of *Gigantopithecus blacki*. *Journal of Human Evolution, 54*(2), 196 - 204. doi:10.1016/j.jhevol.2007.09.013
Kupczik, K., Delezene, L. K., & Skinner, M. M. (2019). Mandibular molar root and pulp cavity morphology in Homo naledi and other Plio-Pleistocene hominins. *Journal of Human Evolution, 130*, 83-95. doi:https://doi.org/10.1016/j.jhevol.2019.03.007
Kupczik, K., & Hublin, J.-J. (2010). Mandibular molar root morphology in Neanderthals and Late Pleistocene and recent *Homo sapiens*. *Journal of Human Evolution, 59*(5), 525 - 541. doi:10.1016/j.jhevol.2010.05.009
Kupczik, K., Toro-Ibacache, V., & Macho, G. A. (2018). On the relationship between maxillary molar root shape and jaw kinematics in *Australopithecus africanus* and *Paranthropus robustus*. *Royal Society Open Science, 5*(8), 180825. doi:10.1098/rsos.180825
Lächelt, S. (2004). *The geology and mineral resources of Mozambique*: Républica de Moçambique, Monostério dos Recursos Minerais e Energia, Direcçâo Nacional de Geologia.
Landini, W., Altamirano-Sierra, A., Collareta, A., Di Celma, C., Urbina, M., & Bianucci, G. (2017). The late Miocene elasmobranch assemblage from Cerro Colorado (Pisco Formation, Peru). *Journal of South American Earth Sciences, 73*, 168-190. doi:https://doi.org/10.1016/j.jsames.2016.12.010
Laumanns, M. (2001). *Mozambique 1998: Report on the European Speleological Project "Cheringoma 1998"*. Retrieved from Berlin:
Lebatard, A.-E., Alçiçek, M. C., Rochette, P., Khatib, S., Vialet, A., Boulbes, N., . . . de Lumley, H. (2014). Dating the Homo erectus bearing travertine from Kocabaş

(Denizli, Turkey) at at least 1.1 Ma. *Earth and Planetary Science Letters, 390*, 8-18. doi:https://doi.org/10.1016/j.epsl.2013.12.031

Lebatard, A.-E., Bourlès, D. L., & Braucher, R. (2019). Absolute dating of an Early Paleolithic site in Western Africa based on the radioactive decay of in situ-produced 10Be and 26Al. *Nuclear Instruments and Methods in Physics Research Section B: Beam Interactions with Materials and Atoms, 456*, 169-179. doi:https://doi.org/10.1016/j.nimb.2019.05.052

Lebatard, A.-E., Bourlès, D. L., Braucher, R., Arnold, M., Duringer, P., Jolivet, M., . . . Brunet, M. (2010). Application of the authigenic 10Be/9Be dating method to continental sediments: Reconstruction of the Mio-Pleistocene sedimentary sequence in the early hominid fossiliferous areas of the northern Chad Basin. *Earth and Planetary Science Letters, 297*(1–2), 57-70. doi:http://dx.doi.org/10.1016/j.epsl.2010.06.003

Lebatard, A.-E., Bourlès, D. L., Duringer, P., Jolivet, M., Braucher, R., Carcaillet, J., . . . Brunet, M. (2008). Cosmogenic nuclide dating of *Sahelanthropus tchadensis* and *Australopithecus bahrelghazali*: Mio-Pliocene hominids from Chad. *Proceedings of the National Academy of Sciences, 105*(9), 3226-3231. doi:10.1073/pnas.0708015105

Macgregor, D. (2015). History of the development of the East African Rift System: A series of interpreted maps through time. *Journal of African Earth Sciences, 101*, 232-252. doi:http://dx.doi.org/10.1016/j.jafrearsci.2014.09.016

Marsili, S., Carnevale, G., Danese, E., Bianucci, G., & Landini, W. (2007). Early Miocene vertebrates from Montagna della Maiella, Italy. *Annales de Paléontologie, 93*(1), 27-66. doi:https://doi.org/10.1016/j.annpal.2007.01.001

Medina, E., & Minchin, P. (1980). Stratification of δ13C values of leaves in Amazonian rain forests. *Oecologia, 45*(3), 377-378. doi:10.1007/BF00540209

Medina, E., Montes, G., Guevas, E., & Rokzandic, Z. (1986). Profiles of CO2 concentration and δ13C values in tropical rain forests of the upper Rio Negro Basin, Venezuela. *Journal of Tropical Ecology, 2*(3), 207-217.

Mercader, J., & Sillén, P. (2013). Middle and Later Stone Age sites from Sofala, Gorongosa (Central Mozambique). *Nyame Akuma, 80*, 3-13.

Morley, R. J., & Kingdon, J. (2013). Africa's environmental and climatic past. In J. Kingdon, D. C. Happold, T. M. Butynski, M. Hoffmann, M. Happold, & J. Kalina (Eds.), *Mammals of Africa* (Vol. 1, pp. 43-56). London: Bloomsbury Publishing.

Pappu, S., Gunnell, Y., Akhilesh, K., Braucher, R., Taieb, M., Demory, F., & Thouveny, N. (2011). Early Pleistocene presence of Acheulian hominins in South India. *Science, 331*(6024), 1596-1599. doi:10.1126/science.1200183

Pearcy, R. W., & Ehleringer, J. (1984). Comparative ecophysiology of C3 and C4 plants. *Plant, Cell & Environment, 7*(1), 1-13. doi:10.1111/j.1365-3040.1984.tb01194.x

Pickford, M. (2009). New Neogene hyracoid specimens from the peri-Tethys region and East Africa. *Paleontological Research, 13*(3), 265-278.

Pickford, M. (2012). *Moçambique palaeontology reconnaissance*. Retrieved from Gorongosa NP:

Pickford, M. (2013). *Gorongosa palaeontology survey*. Retrieved from Gorongosa National Park:

Ponte, J.-P., Robin, C., Guillocheau, F., Popescu, S., Suc, J.-P., Dall'Asta, M., . . . Gaillot, J. (2019). The Zambezi delta (Mozambique channel, East Africa): High resolution dating combining bio- orbital and seismic stratigraphies to determine climate (palaeoprecipitation) and tectonic controls on a passive margin. *Marine and Petroleum Geology, 105*, 293-312. doi:https://doi.org/10.1016/j.marpetgeo.2018.07.017

Pringle, R. M. (2017). Upgrading protected areas to conserve wild biodiversity. *Nature, 546*(7656), 91-99. doi:10.1038/nature22902

Rae, T. C., & Koppe, T. (2004). Holes in the head: Evolutionary interpretations of the paranasal sinuses in catarrhines. *Evolutionary Anthropology, 13*(6), 211-223. doi:https://doi.org/10.1002/evan.20036

Rasmussen, D. T., & Gutiérrez, M. (2010). Hyracoidea. In L. Werdelin & W. J. Sanders (Eds.), *Cenozoic mammals of Africa* (pp. 123-145). Berkeley: University of California Press.

Real, F. (1966). *Geologia da bacia do rio Zambeze (Moçambique): Características geológico-mineiras da bacia do rio Zambeze em território moçambicano*. Lisbon: Junta de Investigações do Ultramar.

Rozanski, K., Araguás-Araguás, L., & Gonfiantini, R. (1992). Isotopic patterns in Global Precipitation. *Journal of Geophysical Research, 78*. doi:10.1029/GM078p0001

Soto Ovalle, L. P. (2016). *Systematics and paleoecology of a new chondrychthian fauna from the Middle Miocene (Barstovian) Torreya Formation, Gadsen County, Florida, USA.* (Master of Science), University of Florida, Gainesville.

Stalmans, M. E., Massad, T. J., Peel, M. J. S., Tarnita, C. E., & Pringle, R. M. (2019). War-induced collapse and asymmetric recovery of large-mammal populations in Gorongosa National Park, Mozambique. *PLoS ONE, 14*(3), e0212864. doi:10.1371/journal.pone.0212864

Storrs, G. W. (2003). Late Miocene-Early Pliocene crocodilian fauna of Lothagam, southwest Turkana Basin, Kenya. In M. G. Leakey & J. M. Harris (Eds.), *Lothagam: The Dawn of Humanity in Eastern Africa* (pp. 137-159). New York: Columbia University Press.

Šujan, M., Braucher, R., Kováč, M., Bourlès, D. L., Rybár, S., Guillou, V., & Hudáčková, N. (2016). Application of the authigenic 10Be/9Be dating method to Late Miocene–Pliocene sequences in the northern Danube Basin (Pannonian Basin System): Confirmation of heterochronous evolution of sedimentary environments. *Global and Planetary Change, 137*, 35-53. doi:https://doi.org/10.1016/j.gloplacha.2015.12.013

Teale, E. O. (1923). The geology of Portuguese East Africa between the Zambesi and Sabi Rivers. *South African Journal of Geology, 26*(Transactions 1923), 103-159.

Tinley, K. L. (1977). *Framework of the Gorongosa ecosystem.* (PhD), University of Pretoria, Pretoria.

Türtscher, J., López-Romero, F. A., Jambura, P. L., Kindlimann, R., Ward, D. J., & Kriwet, J. (2021). Evolution, diversity, and disparity of the tiger shark lineage *Galeocerdo* in deep time. *Paleobiology*, 1-17. doi:10.1017/pab.2021.6

Villafaña, J. A., Marramà, G., Klug, S., Pollerspöck, J., Balsberger, M., Rivadeneira, M., & Kriwet, J. (2020). Sharks, rays and skates (Chondrichthyes, Elasmobranchii) from the Upper Marine Molasse (middle Burdigalian, early Miocene) of the Simssee area (Bavaria, Germany), with comments on palaeogeographic and ecological patterns. *PalZ*. doi:10.1007/s12542-020-00518-7

White, F. (1983). The vegetation of Africa, a descriptive memoir to accompany the UNESCO/AETFAT/UNSO vegetation map of Africa (3 Plates, Northwestern Africa, Northeastern Africa, and Southern Africa, 1: 5,000,000). In: Unesco, Paris.

Wiley, D. F., Amenta, N., Alcantara, D. A., Ghosh, D., Kil, Y. J., Delson, E., . . . Hamann, B. (2005, 23-28 Oct. 2005). *Evolutionary morphing.* Paper presented at the VIS 05. IEEE Visualization, 2005.

Wittmann, H., von Blanckenburg, F., Bouchez, J., Dannhaus, N., Naumann, R., Christl, M., & Gaillardet, J. (2012). The dependence of meteoric 10Be concentrations on particle size in Amazon River bed sediment and the extraction of reactive 10Be/9Be ratios.

Chemical Geology, 318-319, 126-138. doi:https://doi.org/10.1016/j.chemgeo.2012.04.031

Zouhri, S., Khalloufi, B., Bourdon, E., De Lapparent De Broin, F., Rage, J.-C., M'HaÏDrat, L., . . . Elboudali, N. (2017). Marine vertebrate fauna from the late Eocene Samlat Formation of Ad-Dakhla, southwestern Morocco. *Geological Magazine, 155*(7), 1596-1620. doi:10.1017/S0016756817000759

CAPTIONS FOR FIGURES AND TABLES

Number of figures: 18
Number of supplementary figures: 1
Number of tables: 4
Number of supplementary tables: 9

FIGURES

Figure 1. **A)** The East African Rift System (EARS) with the Eastern Branch, the Western Branch, and some of the major basins and rifts, including the Urema Graben at its southern end. The development of the EARS since the Miocene has played a major role in shaping the physical environments and modifying the conditions under which plants and animals have been evolving in eastern Africa. Base map from Nasa Shuttle Radar Topography Mission (https://www2.jpl.nasa.gov/srtm/). **B)** Number of Miocene paleontological localities along the EARS by latitude. There are many Miocene localities in the rift near the equator, but the record away from the equator, especially to the south, is very sparse. Gorongosa is the only Miocene paleontological locality in the southern ~1500 km of the EARS. Locality data from the Paleobiology Database https://paleobiodb.org/classic.

Figure 2. Map of Gorongosa National Park along the East African Rift Valley, with the Cheringoma Plateau to the east and Mount Gorongosa to the northwest. The park hosts a wide range of environments. The new paleontological sites on the Cheringoma Plateau are ~95 km from the coast.

Figure 3. Gorongosa Paleontological Localities and geological formations. **A)** Geological map of Gorongosa National Park and surrounding areas. **B)** Vertical geological cross-section of the Urema Rift stretching from Mount Gorongosa to Inhaminga village. **C)** Map section showing the locations of the fossiliferous sites (GPL = Gorongosa Paleontological Locality). Figure modified from Habermann et al. (2019) and references therein, with new paleontological localities added.

Figure 4. Stratigraphic sections; modified and updated from Habermann et al 2019.

Figure 5. Stable carbon, $\delta^{13}C$, and oxygen, $\delta^{18}O$, isotopic compositions related to the stratigraphic column of GPL-1NE (see Habermann et al., 2019).

Figure 6. Silicified tree trunk with bark preserved at Menguere Hill.

Figure 7. Photomicrographs of thin sections of fossil wood specimen PPP-G-36 from Menguere Hill, *Entandrophragmoxylon* sp. (Meliaceae, African Mahogany). **A)** Transverse section showing large mostly solitary vessels, vasicentric to aliform parenchyma and wide rays with dark contents. **B)** Radial longitudinal section with a vertical column of axial parenchyma cells, and horizontal radial parenchyma cells that are procumbent. **C)** Tangential longitudinal section with vertical columns of axial parenchyma cells and lens-shaped outline of rays with circular parenchyma cells. Letters: V = vessel; R = ray; P = axial parenchyma. Scale bars: A = 1cm; B, C = 500µm.

Figure 8. Gorongosa fossil sharks, all in the genus *Galeocerdo*, tiger sharks. **A)** PPG2019-P-129; **B)** PPG2019-P-127; **C)** PPG2018-P-224; D) PPG2019-P-176; E) PPG2017-P-121; F) PPG2019-P-126.

Figure 9. **A)** PCA of 600 Miocene shark teeth from the genera *Carcharhinus*, *Galeocerdo*, *Hemipristis*, and *Physogaleus*, and including the two Gorongosa complete crowns. **B)** PCA of 547 Miocene shark teeth of the species *Galeocerdo* sp., and *Physogaleus* sp., and the Gorongosa specimens. **C)** PCA of shark teeth including the species *G. aduncus, G. capellini, G. clarkensis, G. cuvier, G. eaglesomei,* and *G. mayumbensis*, with the Gorongosa specimens.

Figure 10: Some fossil reptiles from Gorongosa. **A)** Testudines, **B)** Crocodylia.

Figure 11. **A)** Hyracoid left mandible GPL2018-P-1. **B)** Hyracoid right mandibular fragment, GPL2018-P-2.

Figure 12. **A)** *Thyrohyrax* specimen (DPC 2763) showing the landmarks (orange spheres) and semi-landmarks (light blue spheres) used in this study. This specimen was selected to display the 3D coordinates as it corresponds to the specimen closest to the multivariate mean in this analysis. **B)** Principal component analysis (PCA) of the dental shape variables (only the two first PCs are shown).

Figure 13. **A)** *Afrohyrax* specimen (ZP349) showing the landmarks (orange spheres) and semi-landmarks (light blue spheres) used in this study. This specimen was selected to display the 3D coordinates as it corresponds to the specimen closest to the multivariate mean in this analysis. **B)** Principal component analysis (PCA) of the m3 shape variables (only the two first PCs are shown).

Figure 14. Surface rendering of PPG2017-P-126, left maxillary fragment with alveolar process. **A)** Superior view. In the zygomatic bone some cortical bone surface is still preserved (area highlighted in blue). **B)** inferior view with postcanine tooth roots highlighted in blue. Anterior is to the top. Scale bar = 1 cm.

Figure 15. 3D rendering and CT sections of PPG2017-P-126, left maxillary fragment with alveolar process. **A)** Buccal view. Anterior to the left. Dashed lines indicate virtual sections at the levels of mid-root and root apex. **B)** Apical view of tooth roots and transverse CT scan showing cancellous bone at the level of root apex. **C)** Apical view of tooth roots and transverse CT scan showing cancellous bone at mid-root. Scale bars = 1 cm.

Figure 16. **A)** Inferior view of specimen PPG2017-P-126 showing the broken tooth roots. **B)** Inferior view of specimen PPG2017-P-126 with the tooth roots highlighted in color.

Figure 17: Micro-CT scan of Gorongosa fossil PPG2017-P-126 in inferior view to compare root cross-sections, root canals, and part of the dental arcade with other Miocene and Plio-Pleistocene catarrhine fossil primates from eastern and southern Africa. Anterior is to the top.

Figure 18. **A)** Gorongosa specimen PPG2017-P-126 showing an outline of the M1 roots cross-section with 30 equidistant landmarks and the most lingual point of each root marked in red. **B)** Multivariate mean shape of the primate specimens using the obtained shape variables and the Procrustes distances between the average M1 root shape and each one of the specimens under analysis. Specimens ordered by their Procrustes distance from the mean shape. The median distance (unbroken line) and upper quartile (dashed line) summarize the distances from the mean shape. **C)** Principal Component Analysis (PCA) of the cross-sectional root shapes showing that the Gorongosa specimen is closest to *Cercopithecoides williamsi*, *Simiolus enjessi*, and some chimpanzees when considering the two first principal components (PCs) that account for ~62% of the variance of the sample.

SUPPLEMENTARY FIGURE

Supplementary Figure S1: Detail of the location of Gorongosa Paleontological Locality 12 (GPL-12) with a high density of fossils. See also Figure 3C.

TABLES

Table 1. Gorongosa paleontological localities and depositional environments.

Table 2. Computed authigenic ages for the lower member of the Mazamba Formation. (1) Modern environmental equivalent sample used for fossil samples Be18-Gor-GPL1NE-1, Be18-Gor-GPL1NE-2, Be18-Gor-GPL12-0.1, Be18-Gor-GPL12-1.1, and Be18-Gor-GPL12-4.1: Be18-Bei-EstRi1-1; Modern environmental equivalent samples used for the other fossil samples: Be18-Bei-SavEst-1 and Be18-Bei-SavFor-1 with a weighted mean $^{10}Be/^{9}Be$ ratio of $0.640 \pm 0.034 \times 10^{-8}$. (2) Modern estuarine equivalent samples used for all fossil samples: Be18-Bei-SavEst-1 and Be18-Bei-SavFor-1 with a weighted mean $^{10}Be/^{9}Be$ ratio of $0.640 \pm 0.034 \times 10^{-8}$. (3) Modern source equivalent samples used for all fossil samples: Be18-Gor-Urem-1.1, Be18-Gor-Vun-1.1 and Be18-Gor-VunS1-1.1 with a weighted mean $^{10}Be/^{9}Be$ ratio of $0.226 \pm 0.007 \times 10^{-8}$.

Table 3. Stable carbon and oxygen isotopic values with sample ID, distance from the base of section GPL-1NE, amount of untreated carbonate powder and carbonate content. For stratigraphic context see Habermann et al 2019 and Figure 4.

Table 4. Measurements of hyracoid teeth in mm.

SUPPLEMENTARY TABLES

Supplementary Table S1: Sampling details for rock samples from the lower member of the Mazamba Formation and modern sediment samples taken for atmospheric ^{10}Be dating.

Supplementary Table S2: ^{10}Be and ^{9}Be concentrations and $^{10}Be/^{9}Be$ ratios for modern reference samples and fossil samples from the lower member of the Mazamba Formation

selected for atmospheric ^{10}Be dating. The modern samples and corresponding chemical blank (measured in February 2019) were spiked using 300 µl of a 10^{-3} g.g^{-1} ^{9}Be solution (Sharlau 1000 mg/L Be standard), while the lower Mazamba Formation samples and corresponding chemical blank (measured in May 2019) were spiked with ~150 µl of the LN2C in-house phenakite 3.10^{-3} g.g^{-1} ^{9}Be carrier solution. The ^{10}Be/^{9}Be ratios measured at ASTER were corrected from chemical blank ratios of 1.51 x 10^{-14} for the modern samples and 1.45 x 10^{-15} for the lower Mazamba Formation samples.

Supplementary Table S3 (in-situ): Results of ^{26}Al/^{10}Be analyses. Uncertainties (±1σ) include only analytical uncertainties. To each sample, ~150 µl of the LN2C in-house phenakite 3.10^{-3} g.g^{-1} ^{9}Be carrier solution was added. ^{27}Al natural concentrations were measured by ICP-OES, and these concentrations were sufficient to perform measurements without addition of an aluminum carrier. The concentration measurements were corrected for the chemical blank ratios of 1.91 ± 0.53 x 10^{-15} and 1.32 ± 0.66 x 10^{-15} for ^{10}Be/^{9}Be and ^{26}Al/^{27}Al ratios, respectively.

Supplementary Table S4 (in-situ): Model outputs of burial durations and denudation rates. The data were obtained using a Monte Carlo Regression Model (Braucher, Merchel, Borgomano, & Bourlès, 2011; Pappu et al., 2011). Burial age (expressed here in ka = 1000 a) and denudation rate (expressed in m.Ma^{-1}= meter per million years) uncertainties (reported as 1σ) are a propagation of the half-life uncertainties. Parameters used for the calculation: latitude: 19,09°; altitude: 166 m; pressure: 993.5 mbar; mean density: 2.5 g.cm^{-3}; Stone Scaling: 0.75; τ^{10}Be: 1.387 ± 0.0120 Ma (Chmeleff, von Blanckenburg, Kossert, & Jakob, 2010; Korschinek et al., 2010); τ^{26}Al: 0.705 ± 0.024 Ma (Nishiizumi, 2004; Norris, Gancarz, Rokop, & Thomas, 1983); P10 SLHL: 4.03 ± 0.18 at.g^{-1}.a^{-1} (Borchers et al., 2016; Molliex et al., 2013); ^{10}Be sea level slow muon-induced production: 0.013 ± 0.012 at.g^{-1}.a^{-1}; ^{10}Be sea level fast muon induced production: 0.040 ± 0.004 at.g^{-1}.a^{-1}; ^{26}Al sea level slow muon-induced production: 0.84 ± 0.017 at.g^{-1}.a^{-1}; ^{26}Al sea level fast muon-induced production: 0.081 ± 0.051 at.g^{-1}.a^{-1}; ^{26}Al/^{10}Be spallogenic production ratio: 6.61 ± 0.52; Attenuation Length neutrons: 160 g.cm^{-2}; Attenuation Length slow muons: 1500 g.cm^{-2}; Attenuation Length fast muons: 4320 g.cm^{-2} (Braucher et al., 2011). The studied site's scaled neutronic production is 3.04 at.g^{-1}.a^{-1} for ^{10}Be and 20.11 at.g^{-1}.a^{-1} for ^{26}Al, slow muons production is 0.01 at.g^{-1}.a^{-1} for ^{10}Be and 0.91 at.g^{-1}.a^{-1} for ^{26}Al, and fast muons production is 0.04 at.g^{-1}.a^{-1}

for ^{10}Be and 0.08 $at.g^{-1}.a^{-1}$ for ^{26}Al (Stone, 2000; Braucher et al., 2011). B. = burial; Denud. = denudation; Min = minimum; Max = maximum.

Supplementary Table S5. Comparative sample of fossil shark teeth from the published record.

Supplementary Table S6. Analysis of shark teeth: results of LDA models.

Supplementary Table S7: Comparative sample of hyracoid mandibular teeth from the National Museums of Kenya, Nairobi.

Supplementary Table S8: Comparative sample of hyracoid m3s from the National Museums of Kenya, Nairobi.

Supplementary Table S9: primate M1 roots comparative sample.

Bibliography

Borchers, B., Marrero, S., Balco, G., Caffee, M., Goehring, B., Lifton, N., . . . Stone, J. (2016). Geological calibration of spallation production rates in the CRONUS-Earth project. *Quaternary Geochronology, 31*, 188-198. doi:https://doi.org/10.1016/j.quageo.2015.01.009

Braucher, R., Merchel, S., Borgomano, J., & Bourlès, D. L. (2011). Production of cosmogenic radionuclides at great depth: A multi element approach. *Earth and Planetary Science Letters, 309*(1), 1-9. doi:https://doi.org/10.1016/j.epsl.2011.06.036

Chmeleff, J., von Blanckenburg, F., Kossert, K., & Jakob, D. (2010). Determination of the 10Be half-life by multicollector ICP-MS and liquid scintillation counting. *Nuclear Instruments and Methods in Physics Research Section B: Beam Interactions with Materials and Atoms, 268*(2), 192-199. doi:https://doi.org/10.1016/j.nimb.2009.09.012

Korschinek, G., Bergmaier, A., Faestermann, T., Gerstmann, U. C., Knie, K., Rugel, G., . . . Remmert, A. (2010). A new value for the half-life of 10Be by Heavy-Ion Elastic Recoil Detection and liquid scintillation counting. *Nuclear Instruments and Methods in Physics Research Section B: Beam Interactions with Materials and Atoms, 268*(2), 187-191. doi:https://doi.org/10.1016/j.nimb.2009.09.020

Molliex, S., Siame, L. L., Bourlès, D. L., Bellier, O., Braucher, R., & Clauzon, G. (2013). Quaternary evolution of a large alluvial fan in a periglacial setting (Crau Plain, SE France) constrained by terrestrial cosmogenic nuclide (10Be). *Geomorphology, 195*, 45-52. doi:https://doi.org/10.1016/j.geomorph.2013.04.025

Nishiizumi, K. (2004). Preparation of 26Al AMS standards. *Nuclear Instruments and Methods in Physics Research Section B: Beam Interactions with Materials and Atoms, 223-224*, 388-392. doi:https://doi.org/10.1016/j.nimb.2004.04.075

Norris, T. L., Gancarz, A. J., Rokop, D. J., & Thomas, K. W. (1983). Half-life of 26Al. *Journal of Geophysical Research: Solid Earth, 88*(S01), B331-B333. doi:https://doi.org/10.1029/JB088iS01p0B331

Pappu, S., Gunnell, Y., Akhilesh, K., Braucher, R., Taieb, M., Demory, F., & Thouveny, N. (2011). Early Pleistocene presence of Acheulian hominins in South India. *Science, 331*(6024), 1596-1599. doi:10.1126/science.1200183

Figure 1

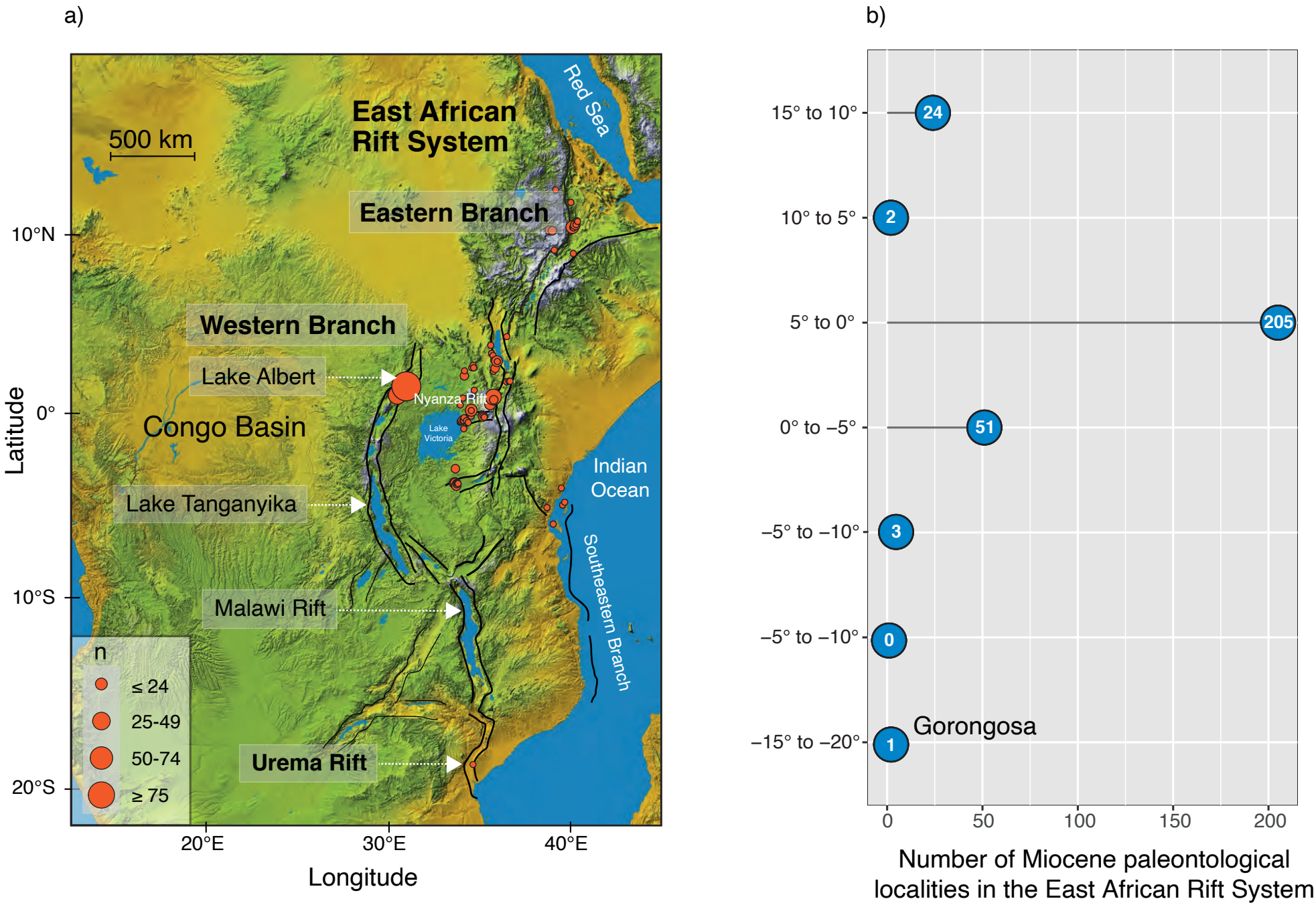
a)
b)
East African
Rift System
500 km
Red Sea
Eastern Branch
Western Branch
Lake Albert
Nyanza Rift
Lake
Victoria
Congo Basin
Lake Tanganyika
Malawi Rift
Urema Rift
Indian
Ocean
Southeastern Branch
n
≤ 24
25-49
50-74
≥ 75
10°N
0°
10°S
20°S
Latitude
20°E
30°E
40°E
Longitude
15° to 10°
10° to 5°
5° to 0°
0° to −5°
−5° to −10°
−5° to −10°
−15° to −20°
24
2
205
51
3
0
1
Gorongosa
0
50
100
150
200
Number of Miocene paleontological
localities in the East African Rift System

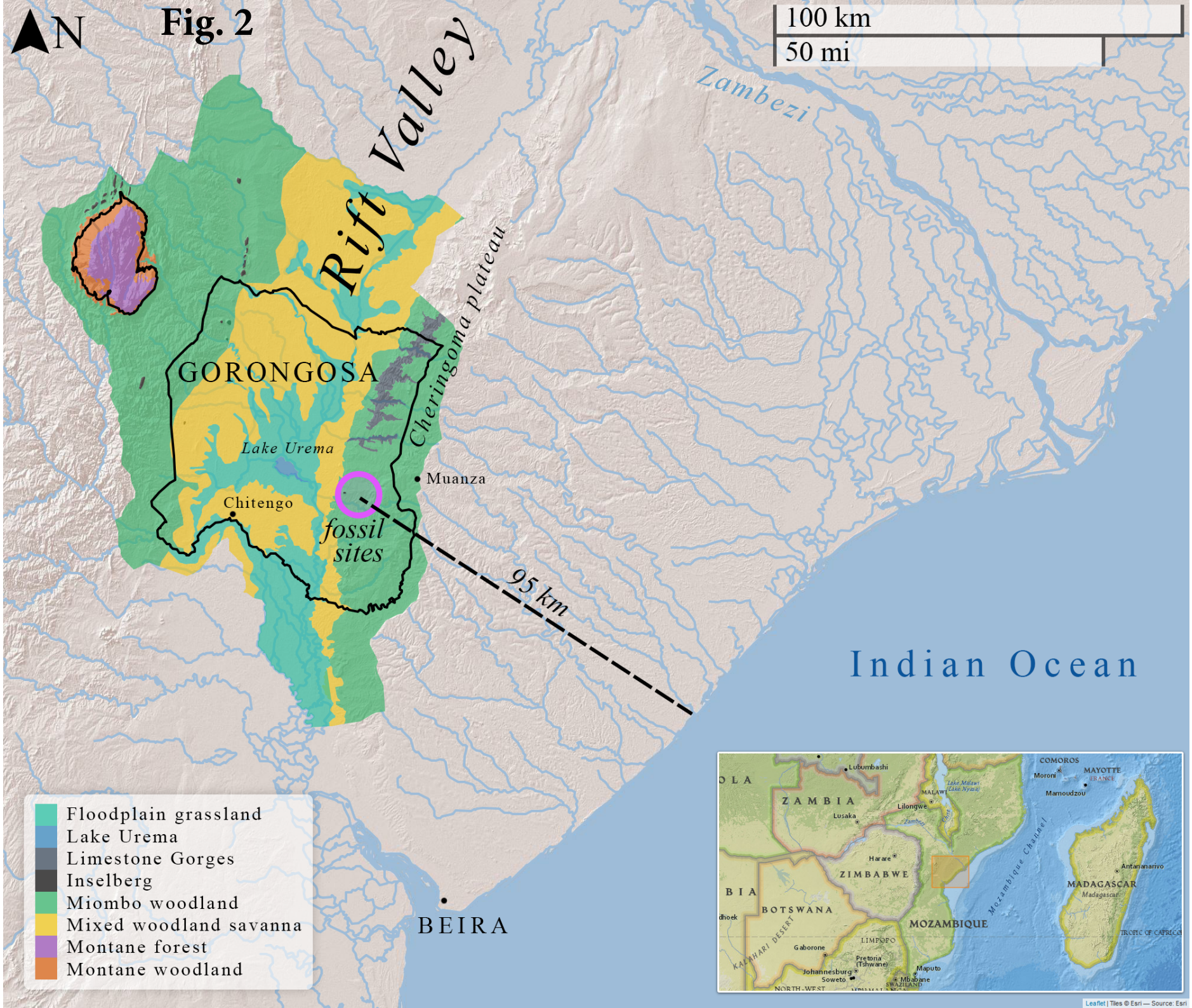
N
Fig. 2
100 km
50 mi
Zambezi
Rift Valley
Cheringoma plateau
GORONGOSA
Lake Urema
Muanza
Chitengo
fossil sites
95 km
Indian Ocean
BEIRA
Floodplain grassland
Lake Urema
Limestone Gorges
Inselberg
Miombo woodland
Mixed woodland savanna
Montane forest
Montane woodland
ZAMBIA
ZIMBABWE
BOTSWANA
MOZAMBIQUE
MADAGASCAR
COMOROS
MAYOTTE
Lubumbashi
Lusaka
Lilongwe
Harare
Gaborone
Pretoria (Tshwane)
Johannesburg
Soweto
Maputo
Mbabane
Moroni
Mamoudzou
Antananarivo
Mozambique Channel
KALAHARI DESERT
LIMPOPO
TROPIC OF CAPRICORN
Leaflet | Tiles © Esri — Source: Esri

Figure 3

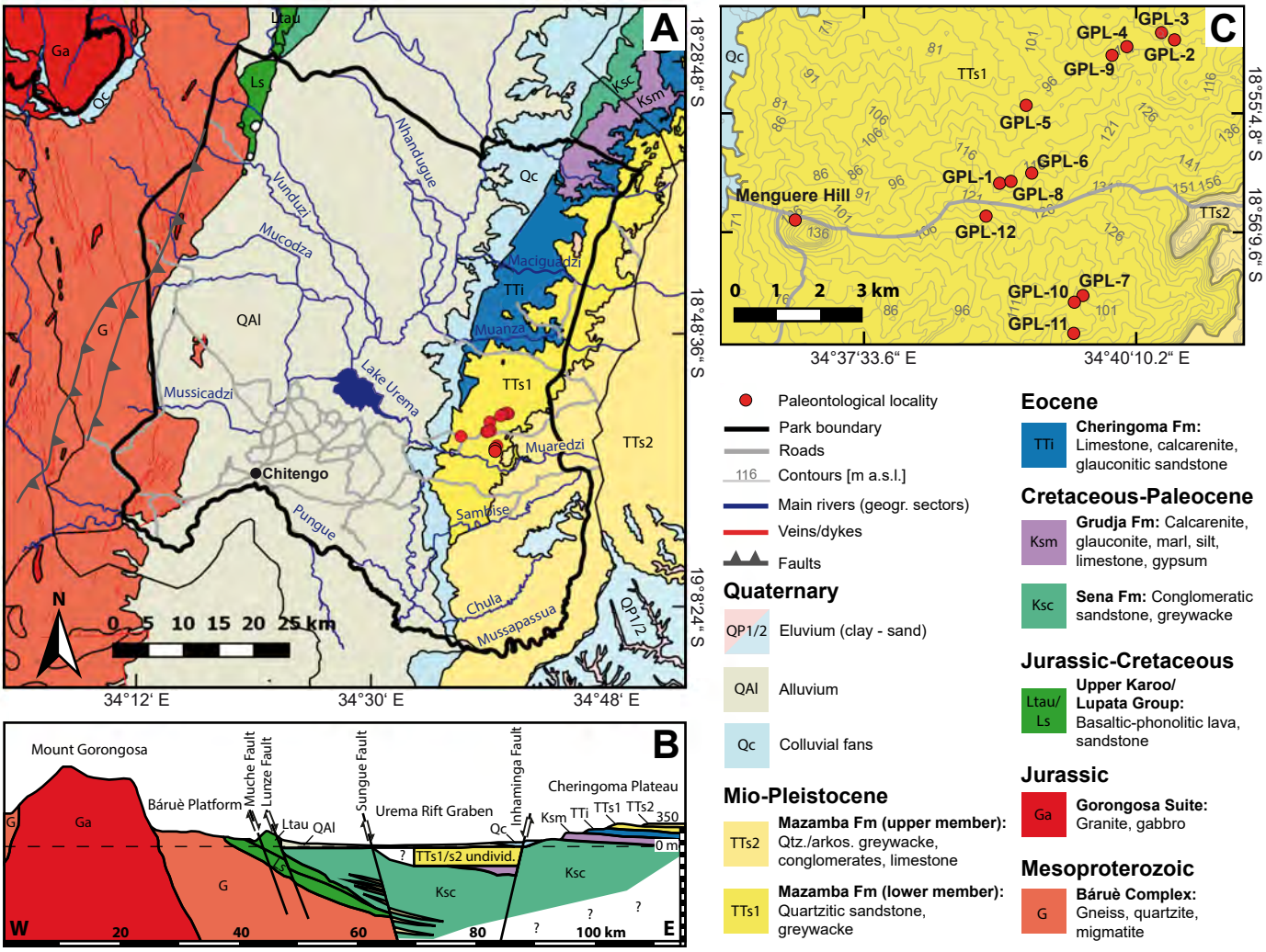

Paleontological locality
Park boundary
Roads
116 Contours [m a.s.l.]
Main rivers (geogr. sectors)
Veins/dykes
Faults

Quaternary

QP1/2 Eluvium (clay - sand)

QAl Alluvium

Qc Colluvial fans

Mio-Pleistocene

TTs2 **Mazamba Fm (upper member):** Qtz./arkos. greywacke, conglomerates, limestone

TTs1 **Mazamba Fm (lower member):** Quartzitic sandstone, greywacke

Eocene

TTi **Cheringoma Fm:** Limestone, calcarenite, glauconitic sandstone

Cretaceous-Paleocene

Ksm **Grudja Fm:** Calcarenite, glauconite, marl, silt, limestone, gypsum

Ksc **Sena Fm:** Conglomeratic sandstone, greywacke

Jurassic-Cretaceous

Ltau/Ls **Upper Karoo/ Lupata Group:** Basaltic-phonolitic lava, sandstone

Jurassic

Ga **Gorongosa Suite:** Granite, gabbro

Mesoproterozoic

G **Báruè Complex:** Gneiss, quartzite, migmatite

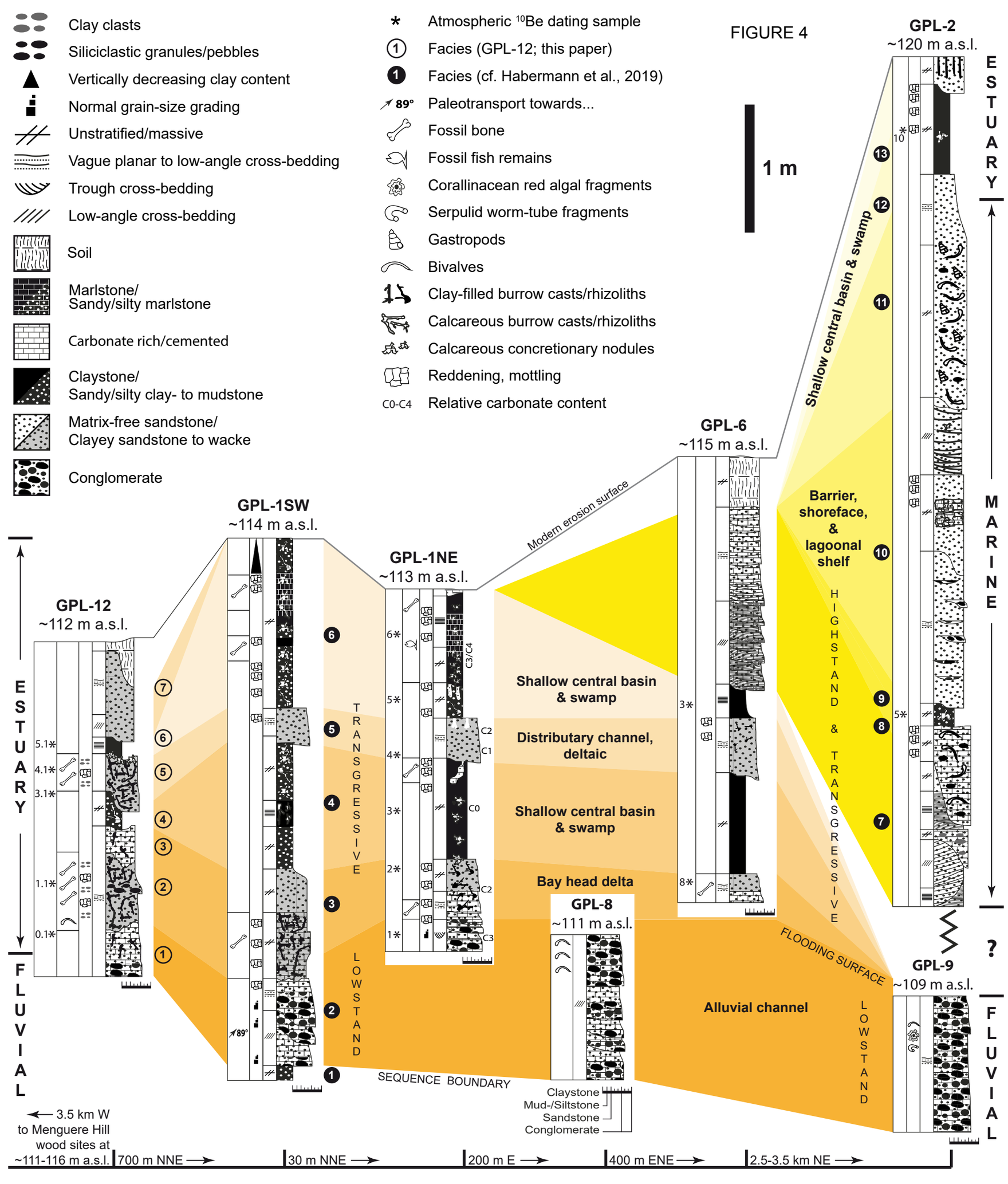
FIGURE 4
Clay clasts
Siliciclastic granules/pebbles
Vertically decreasing clay content
Normal grain-size grading
Unstratified/massive
Vague planar to low-angle cross-bedding
Trough cross-bedding
Low-angle cross-bedding
Soil
Marlstone/
Sandy/silty marlstone
Carbonate rich/cemented
Claystone/
Sandy/silty clay- to mudstone
Matrix-free sandstone/
Clayey sandstone to wacke
Conglomerate
Atmospheric 10Be dating sample
Facies (GPL-12; this paper)
Facies (cf. Habermann et al., 2019)
89° Paleotransport towards...
Fossil bone
Fossil fish remains
Corallinacean red algal fragments
Serpulid worm-tube fragments
Gastropods
Bivalves
Clay-filled burrow casts/rhizoliths
Calcareous burrow casts/rhizoliths
Calcareous concretionary nodules
Reddening, mottling
C0-C4 Relative carbonate content
1 m
GPL-2
~120 m a.s.l.
GPL-6
~115 m a.s.l.
GPL-1SW
~114 m a.s.l.
GPL-1NE
~113 m a.s.l.
GPL-12
~112 m a.s.l.
GPL-8
~111 m a.s.l.
GPL-9
~109 m a.s.l.
Modern erosion surface
Shallow central basin & swamp
Barrier, shoreface, & lagoonal shelf
HIGHSTAND & TRANSGRESSIVE
Shallow central basin & swamp
Distributary channel, deltaic
Shallow central basin & swamp
Bay head delta
Alluvial channel
FLOODING SURFACE
LOWSTAND
TRANSGRESSIVE
LOWSTAND
SEQUENCE BOUNDARY
ESTUARY
MARINE
ESTUARY
FLUVIAL
FLUVIAL
?
Claystone
Mud-/Siltstone
Sandstone
Conglomerate
3.5 km W to Menguere Hill wood sites at ~111-116 m a.s.l.
700 m NNE
30 m NNE
200 m E
400 m ENE
2.5-3.5 km NE

Figure 5: Stable carbon and oxygen isotopic compositions related to the stratigraphic column of GPL-1NE (see Habermann et al. 2019)

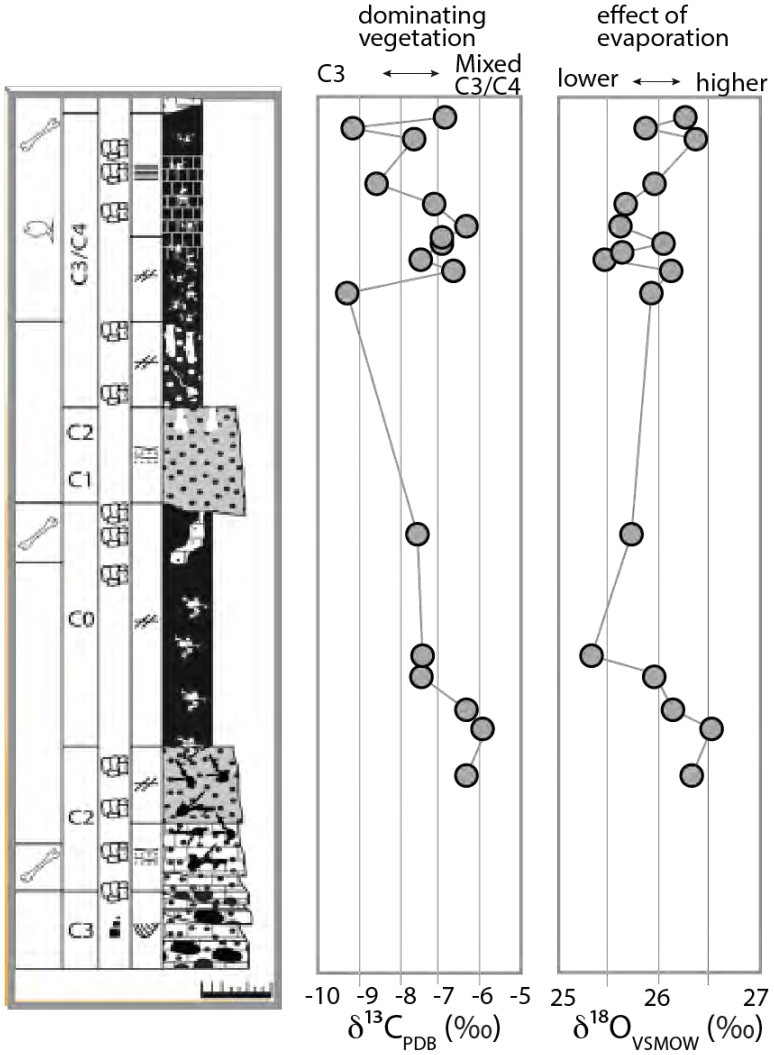

Fig. 6

GSA
PHOTO SCALE/FOCUS GUIDE
Avoid incorrect exposures by taking meter readings before placing scale in picture area. Fine-focus on GSA seal.
IN
CM
Grain Size Scale
1 2 3 4 5
mm

Figure 7

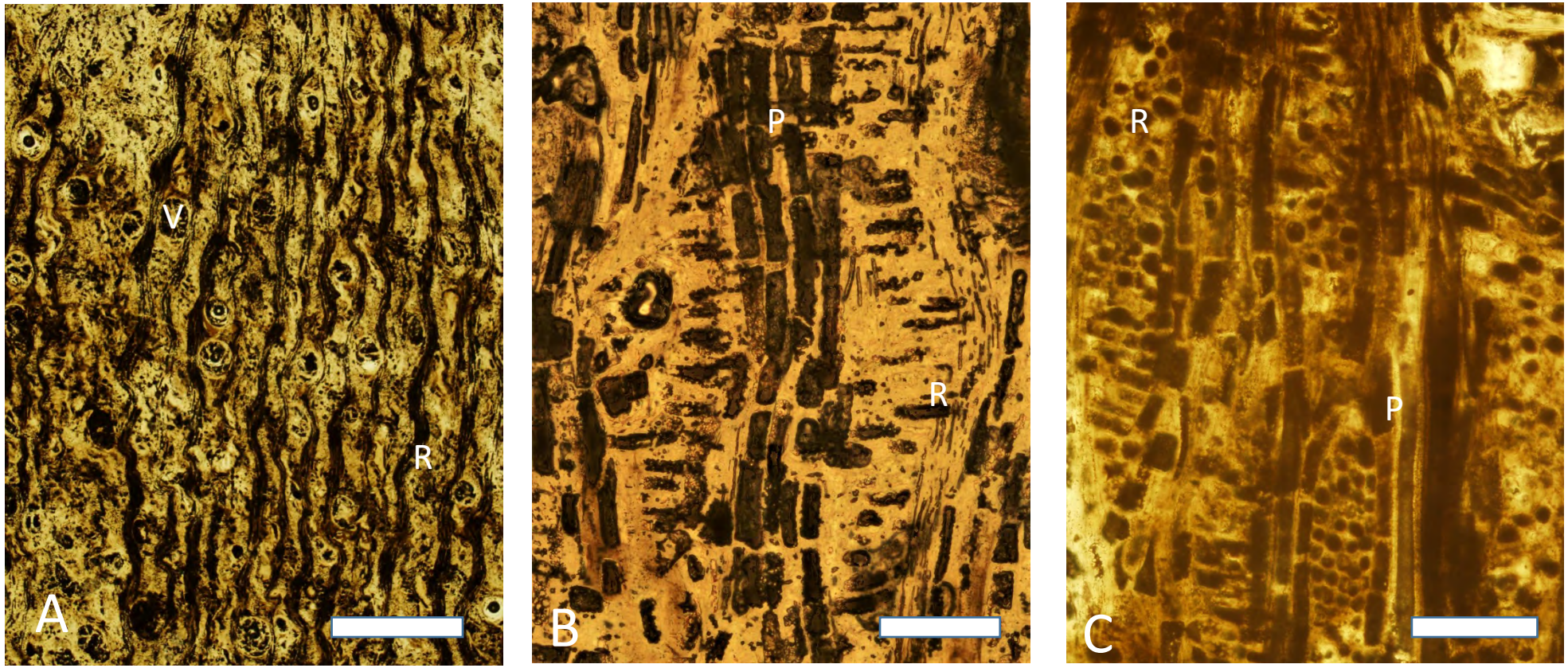

Figure 7: Photomicrographs of thin sections of fossil wood specimen PPP-G-36 from Menguere Hill, *Entandrophragmoxylon* sp. (Meliaceae, African Mahogany). A) Transverse section showing large mostly solitary vessels, vasicentric to aliform parenchyma and wide rays with dark contents. B) Radial longitudinal section with a vertical column of axial parenchyma cells, and horizontal radial parenchyma cells that are procumbent. C) Tangential longitudinal section with vertical columns of axial parenchyma cells and lens-shaped outline of rays with circular parenchyma cells. Letters: V = vessel; R = ray; P = axial parenchyma. Scale bars: A = 1cm; B, C = 500µm.

Fig. 8

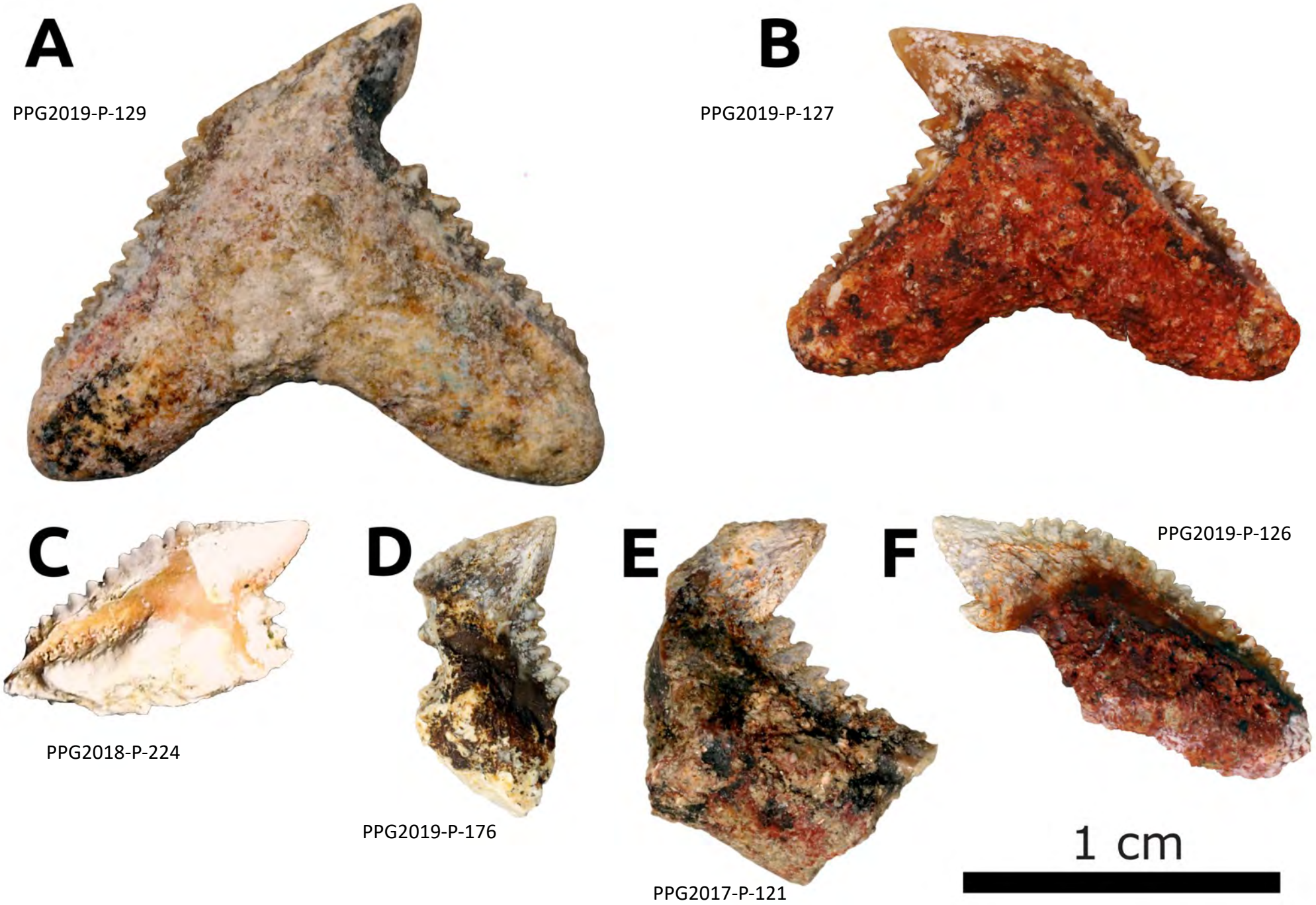
A
PPG2019-P-129
B
PPG2019-P-127
C
PPG2018-P-224
D
PPG2019-P-176
E
PPG2017-P-121
F
PPG2019-P-126
1 cm

Fig. 9A

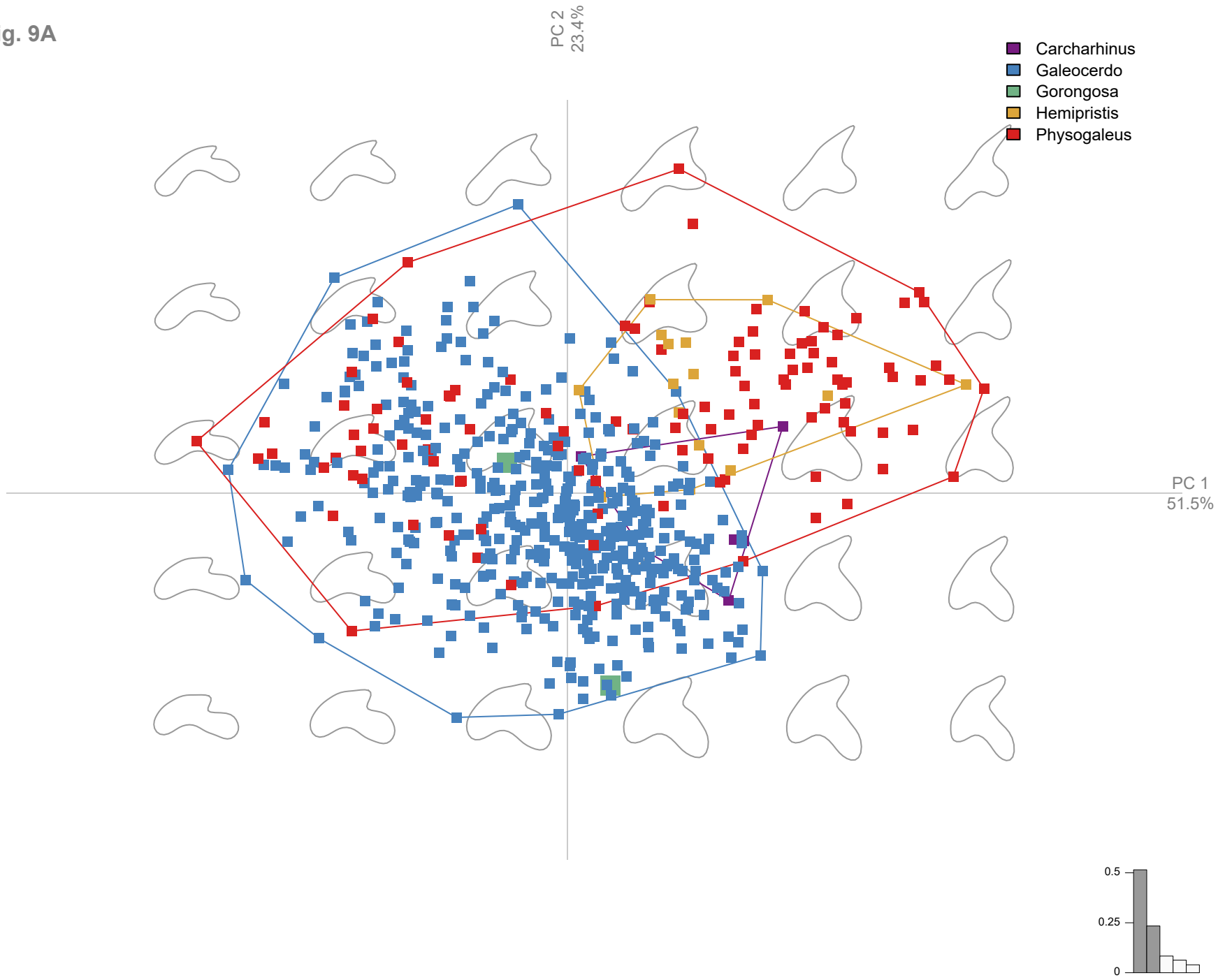
PC 2
23.4%
Carcharhinus
Galeocerdo
Gorongosa
Hemipristis
Physogaleus
PC 1
51.5%
0.5
0.25
0

Fig. 9B

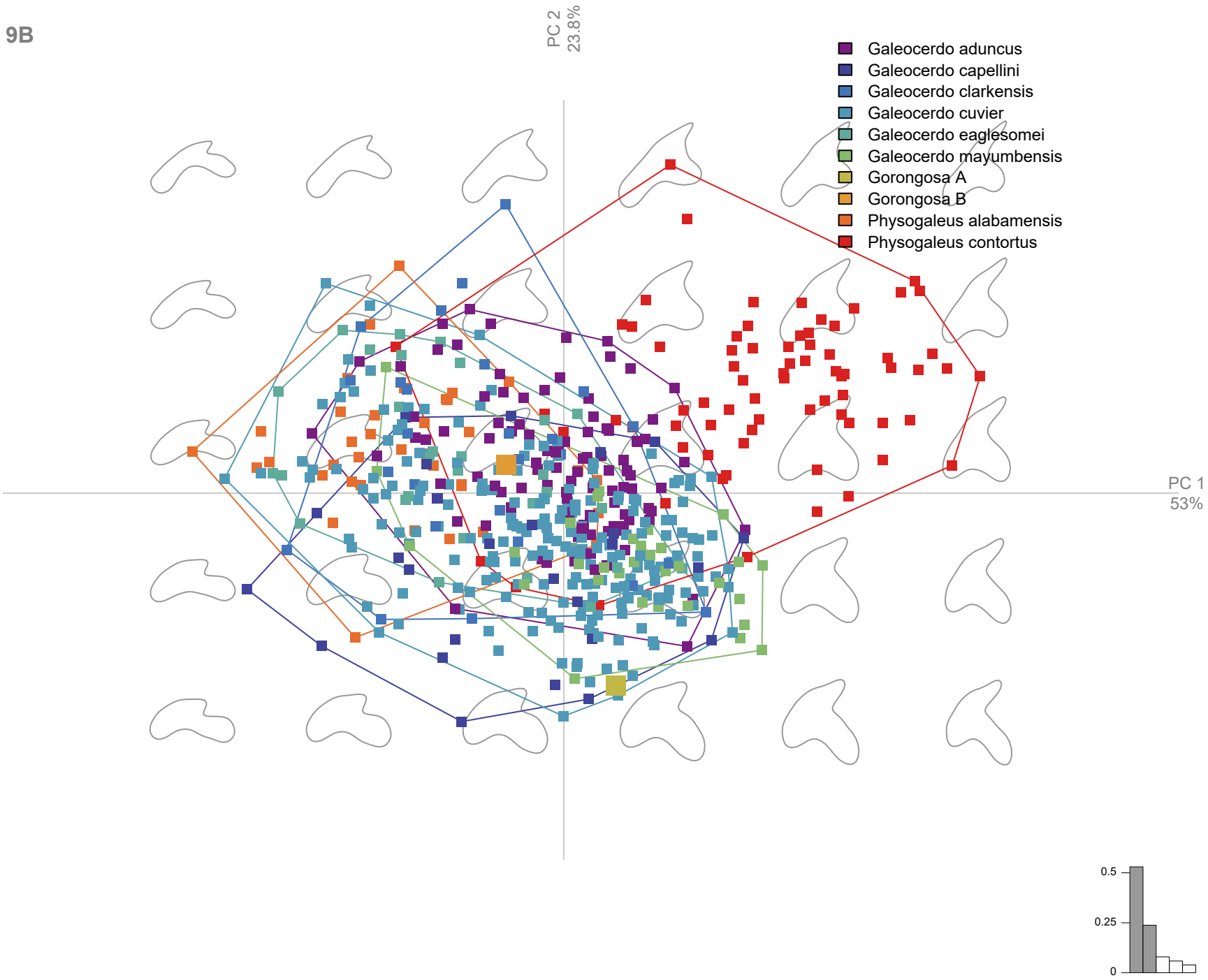
PC 2
23.8%
PC 1
53%
Galeocerdo aduncus
Galeocerdo capellini
Galeocerdo clarkensis
Galeocerdo cuvier
Galeocerdo eaglesomei
Galeocerdo mayumbensis
Gorongosa A
Gorongosa B
Physogaleus alabamensis
Physogaleus contortus
0.5
0.25
0

Fig. 9C

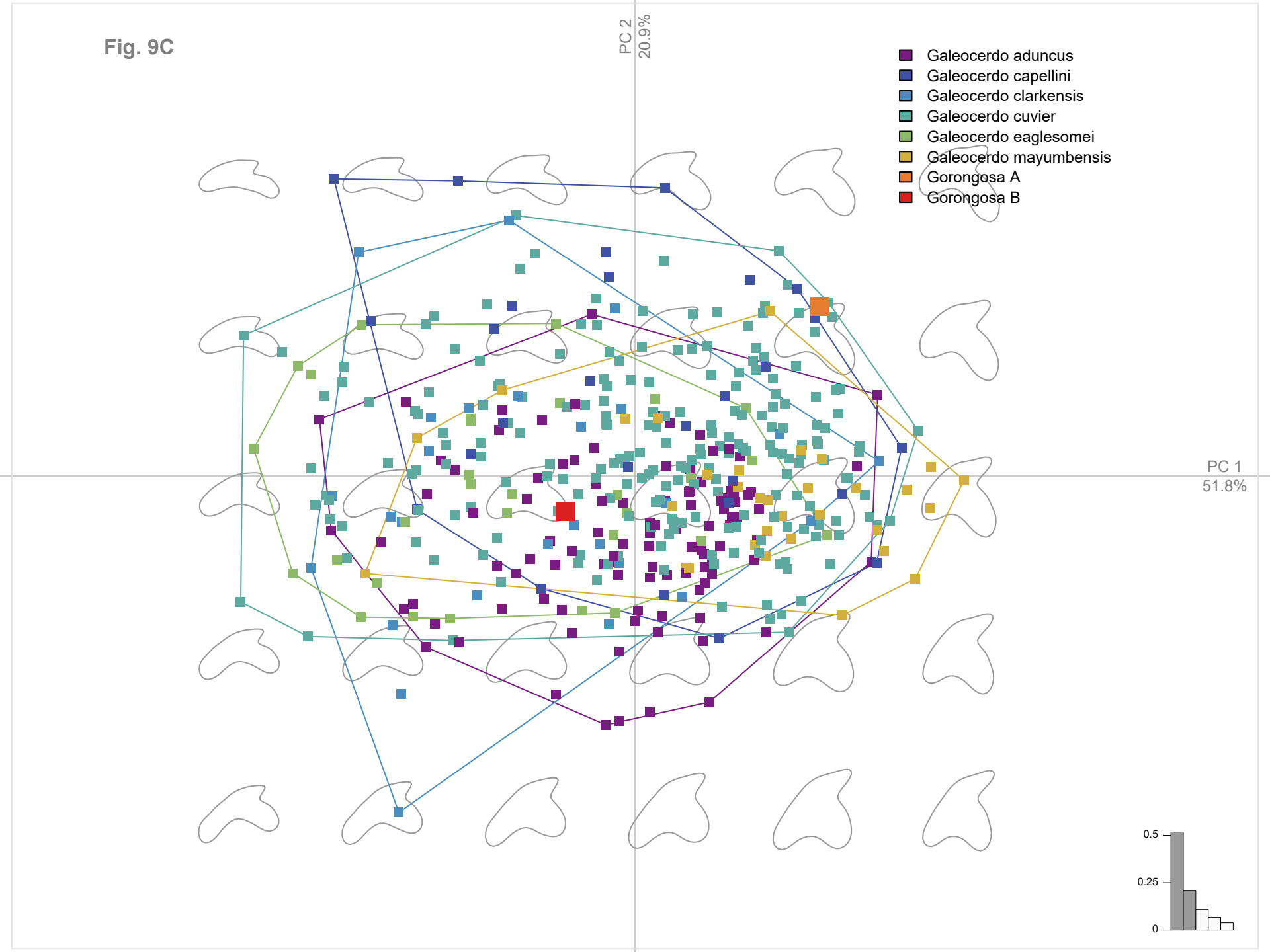
PC 2
20.9%
PC 1
51.8%
Galeocerdo aduncus
Galeocerdo capellini
Galeocerdo clarkensis
Galeocerdo cuvier
Galeocerdo eaglesomei
Galeocerdo mayumbensis
Gorongosa A
Gorongosa B
0.5
0.25
0

Fig 10

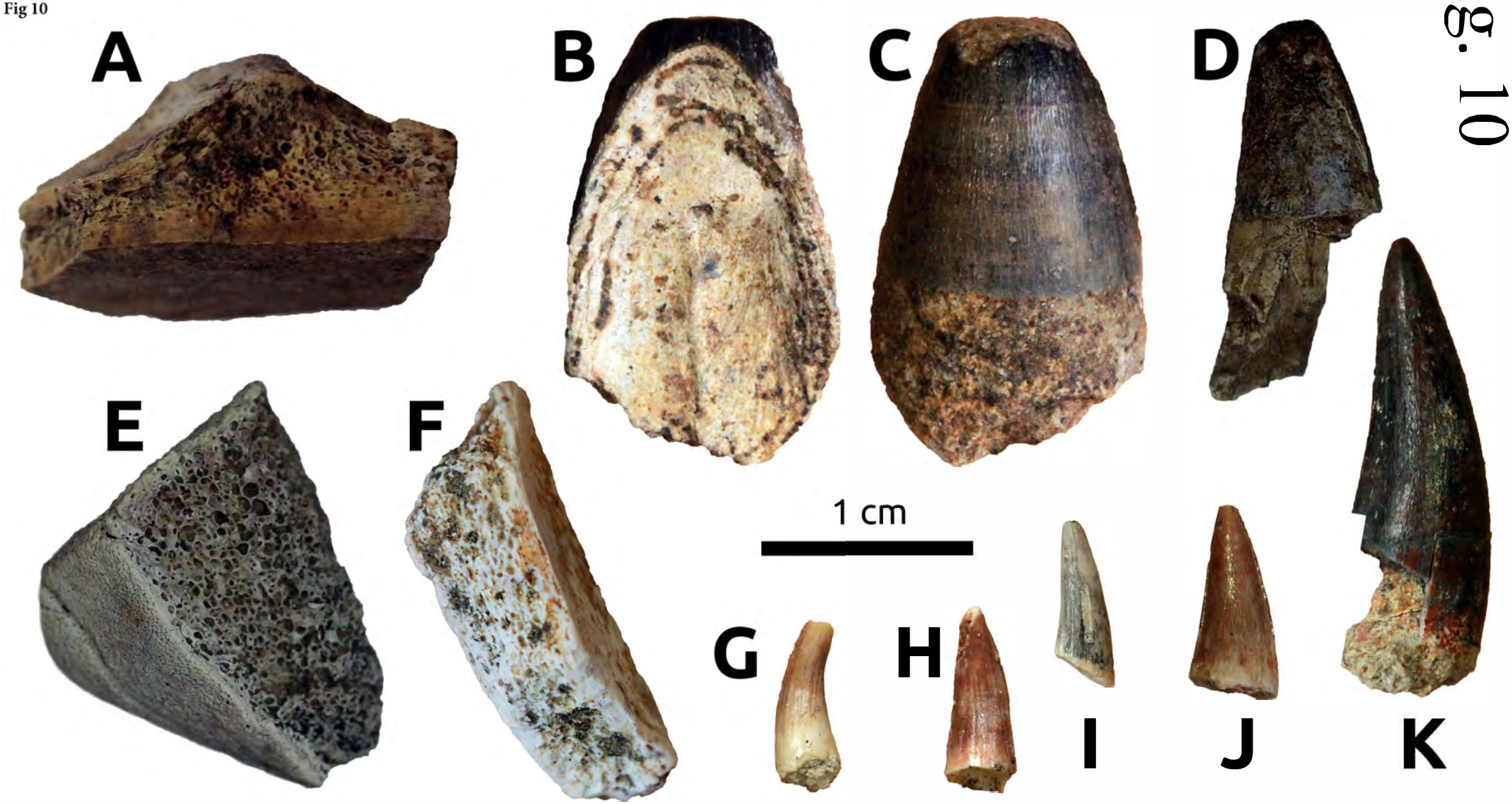

Fig. 10

Figure 11

Figure 11A

Figure 11B

Fig. 12

a)

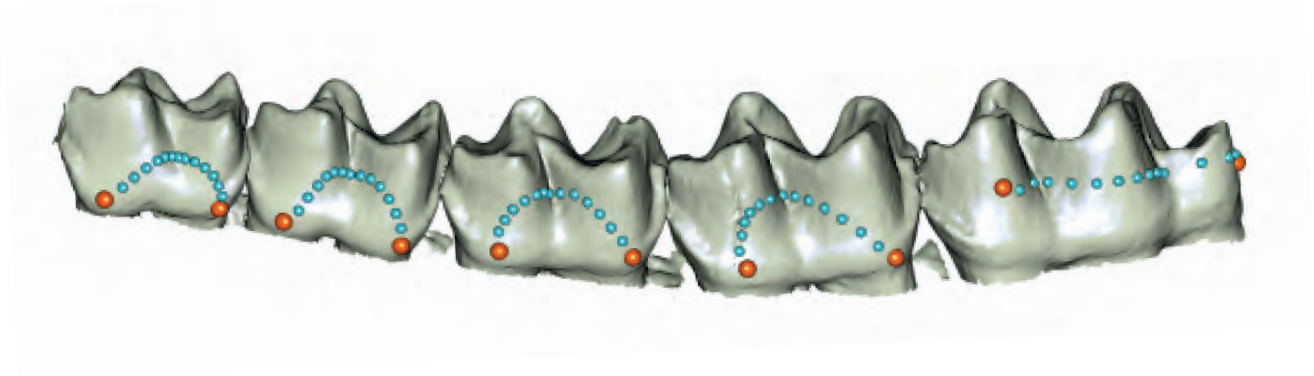

b)

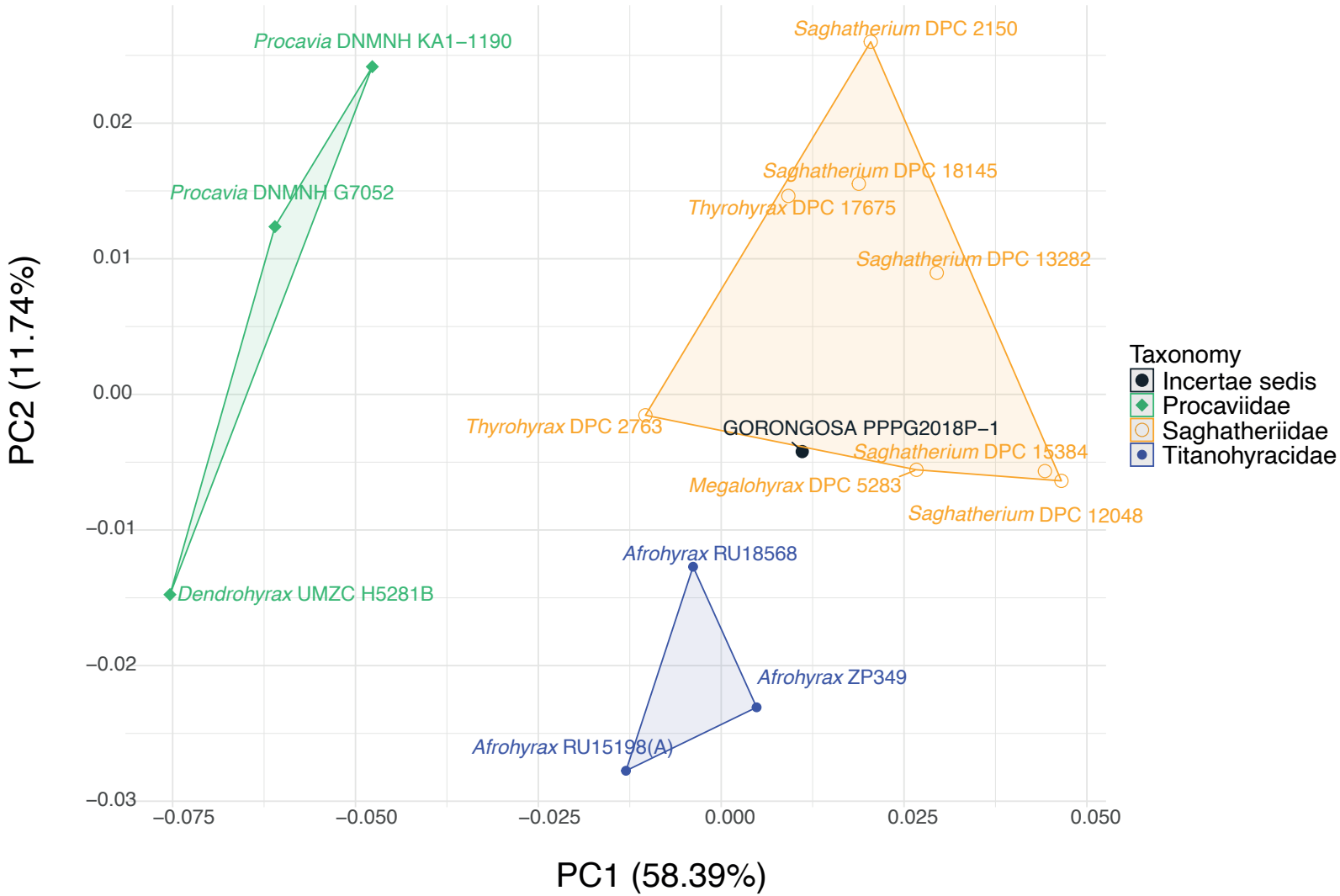
Procavia DNMNH KA1–1190
Procavia DNMNH G7052
Dendrohyrax UMZC H5281B
Saghatherium DPC 2150
Saghatherium DPC 18145
Thyrohyrax DPC 17675
Saghatherium DPC 13282
Thyrohyrax DPC 2763
GORONGOSA PPPG2018P–1
Saghatherium DPC 15384
Megalohyrax DPC 5283
Saghatherium DPC 12048
Afrohyrax RU18568
Afrohyrax ZP349
Afrohyrax RU15198(A)
0.02
0.01
0.00
–0.01
–0.02
–0.03
–0.075
–0.050
–0.025
0.000
0.025
0.050
PC2 (11.74%)
PC1 (58.39%)
Taxonomy
Incertae sedis
Procaviidae
Saghatheriidae
Titanohyracidae

Fig 13

a)

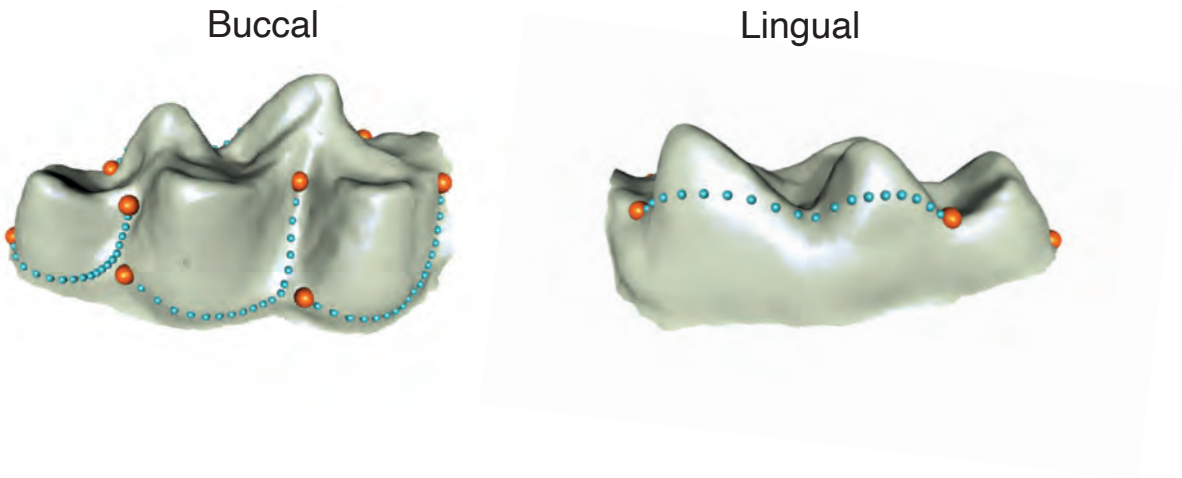
Buccal
Lingual

b)

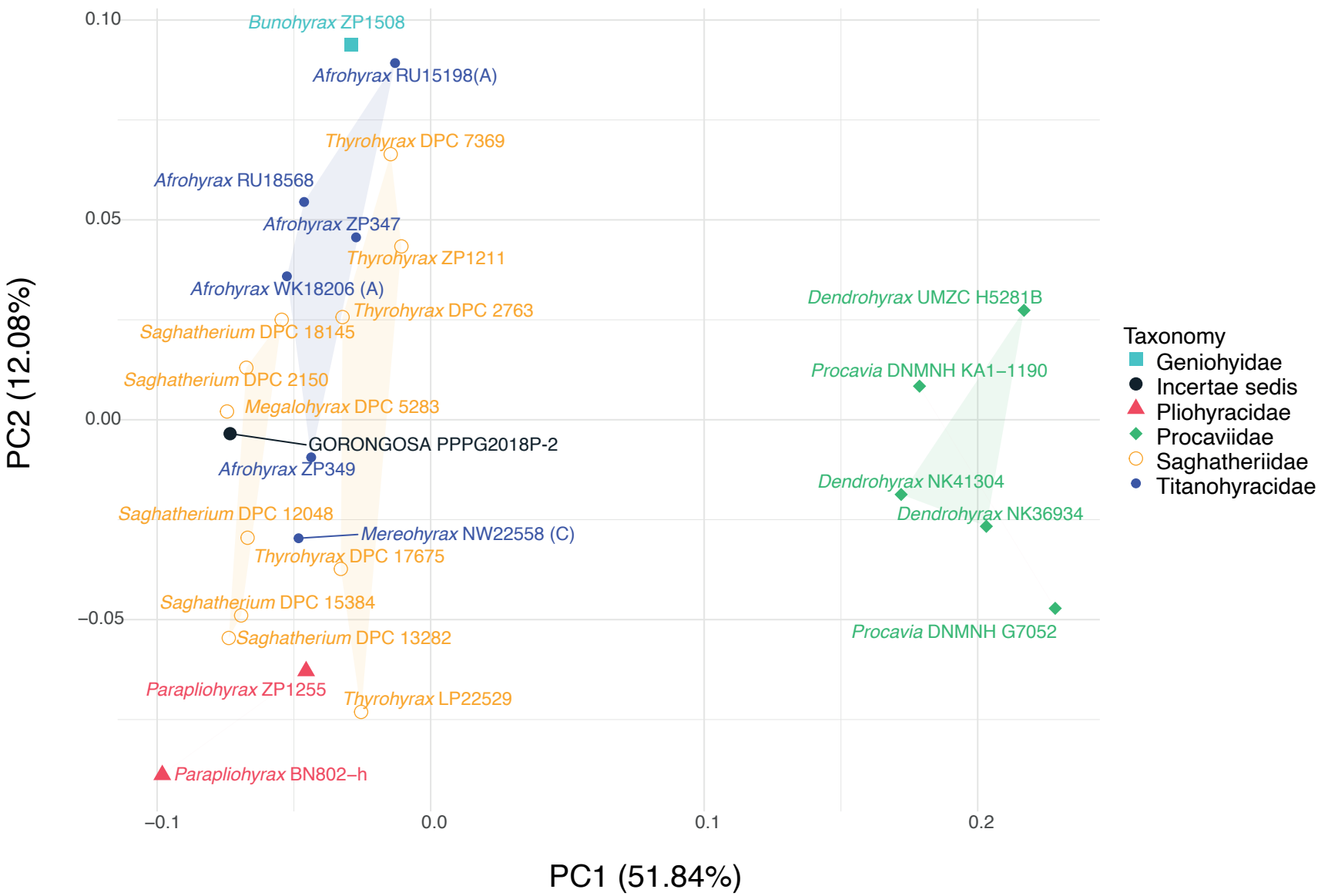
Bunohyrax ZP1508
Afrohyrax RU15198(A)
Thyrohyrax DPC 7369
Afrohyrax RU18568
Afrohyrax ZP347
Thyrohyrax ZP1211
Afrohyrax WK18206 (A)
Thyrohyrax DPC 2763
Saghatherium DPC 18145
Saghatherium DPC 2150
Megalohyrax DPC 5283
GORONGOSA PPPG2018P-2
Afrohyrax ZP349
Saghatherium DPC 12048
Mereohyrax NW22558 (C)
Thyrohyrax DPC 17675
Saghatherium DPC 15384
Saghatherium DPC 13282
Parapliohyrax ZP1255
Thyrohyrax LP22529
Parapliohyrax BN802–h
Dendrohyrax UMZC H5281B
Procavia DNMNH KA1–1190
Dendrohyrax NK41304
Dendrohyrax NK36934
Procavia DNMNH G7052
0.10
0.05
0.00
−0.05
−0.1
0.0
0.1
0.2
PC2 (12.08%)
PC1 (51.84%)
Taxonomy
Geniohyidae
Incertae sedis
Pliohyracidae
Procaviidae
Saghatheriidae
Titanohyracidae

Fig. 14

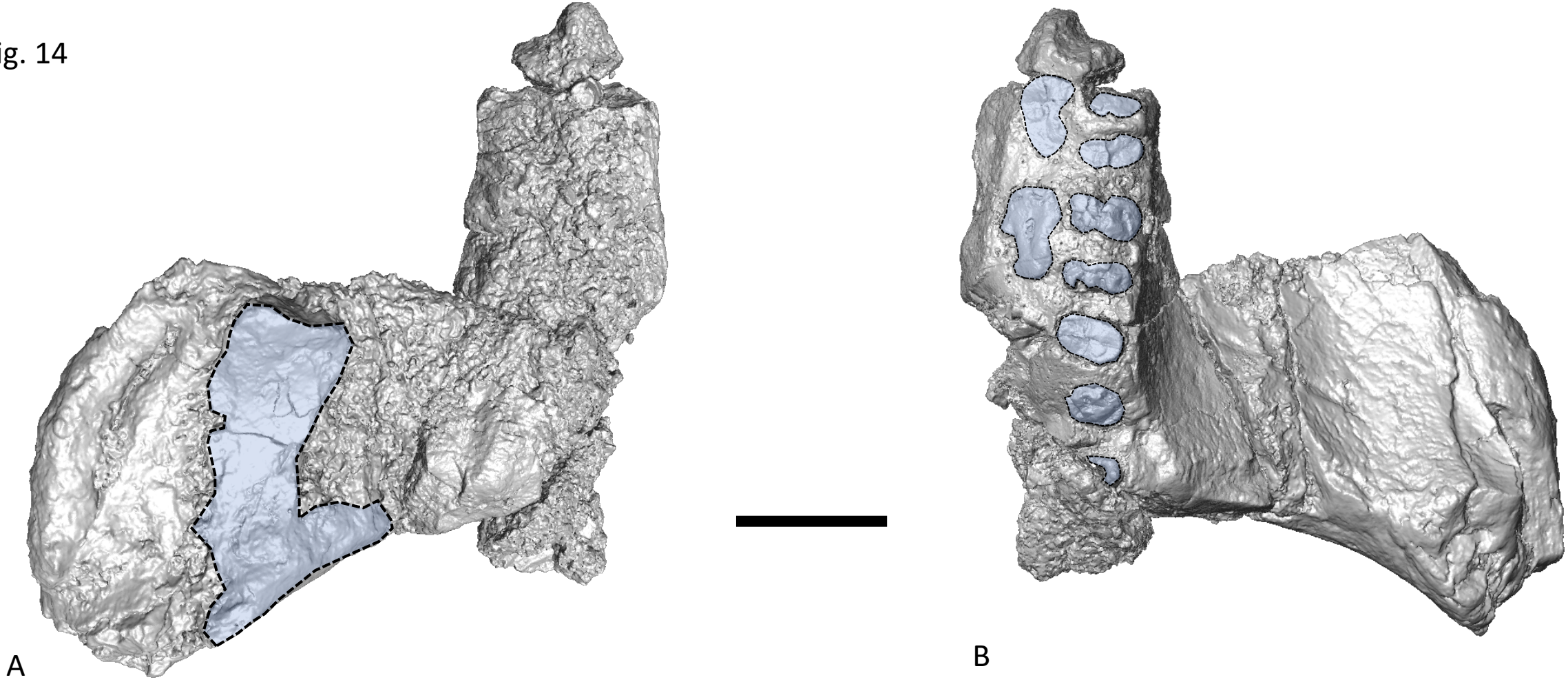

Fig. 14. Surface rendering of PPG2017-P-126, left maxillary fragment with alveolar process. (A) Superior view. In the zygomatic bone some cortical bone surface is still preserved (area highlighted in blue). (B) inferior view with postcanine tooth roots highlighted in blue. Anterior is to the top. Scale bar = 1 cm.

Fig. 15

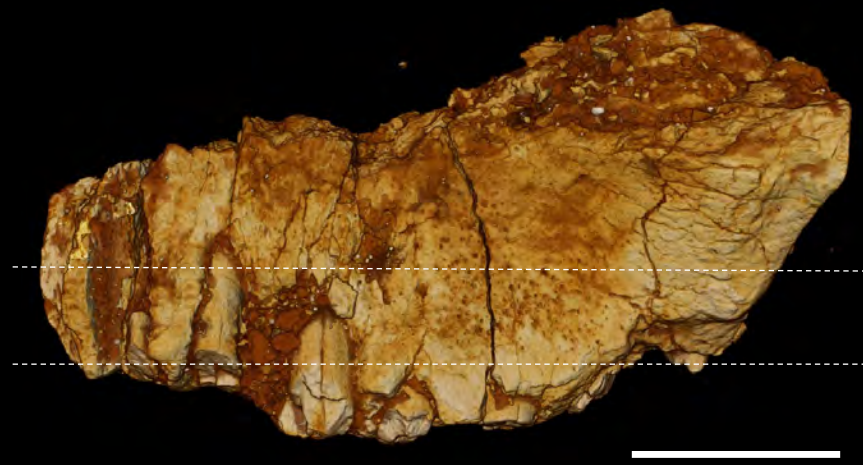

A

B

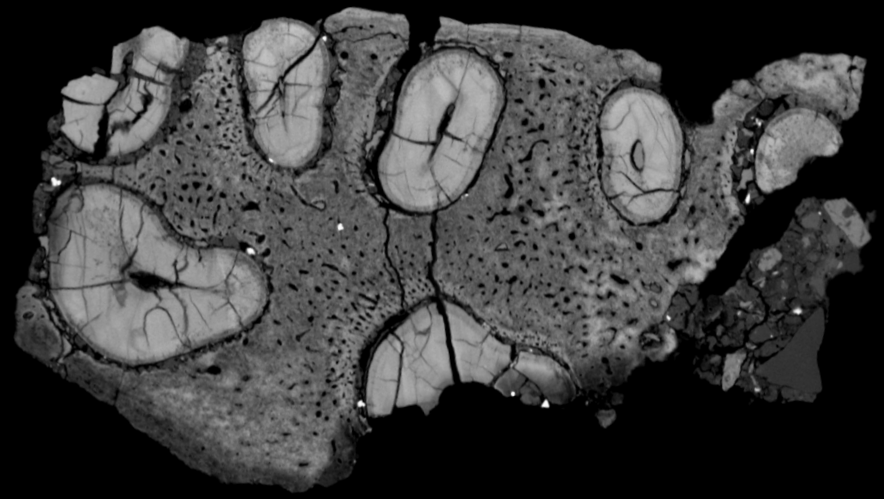

C

Figure 15. 3D rendering and CT sections of PPG2017-P-126, left maxillary fragment with alveolar process. (A) Buccal view. Anterior to the left. Dashed lines indicate virtual sections at the levels of mid-root and root apex. (B) Apical view of tooth roots and transverse CT scan showing cancellous bone at the level of root apex. (C) Apical view of tooth roots and transverse CT scan showing cancellous bone at mid-root. Scale bars = 1 cm.

Fig. 16A

Fig. 16B

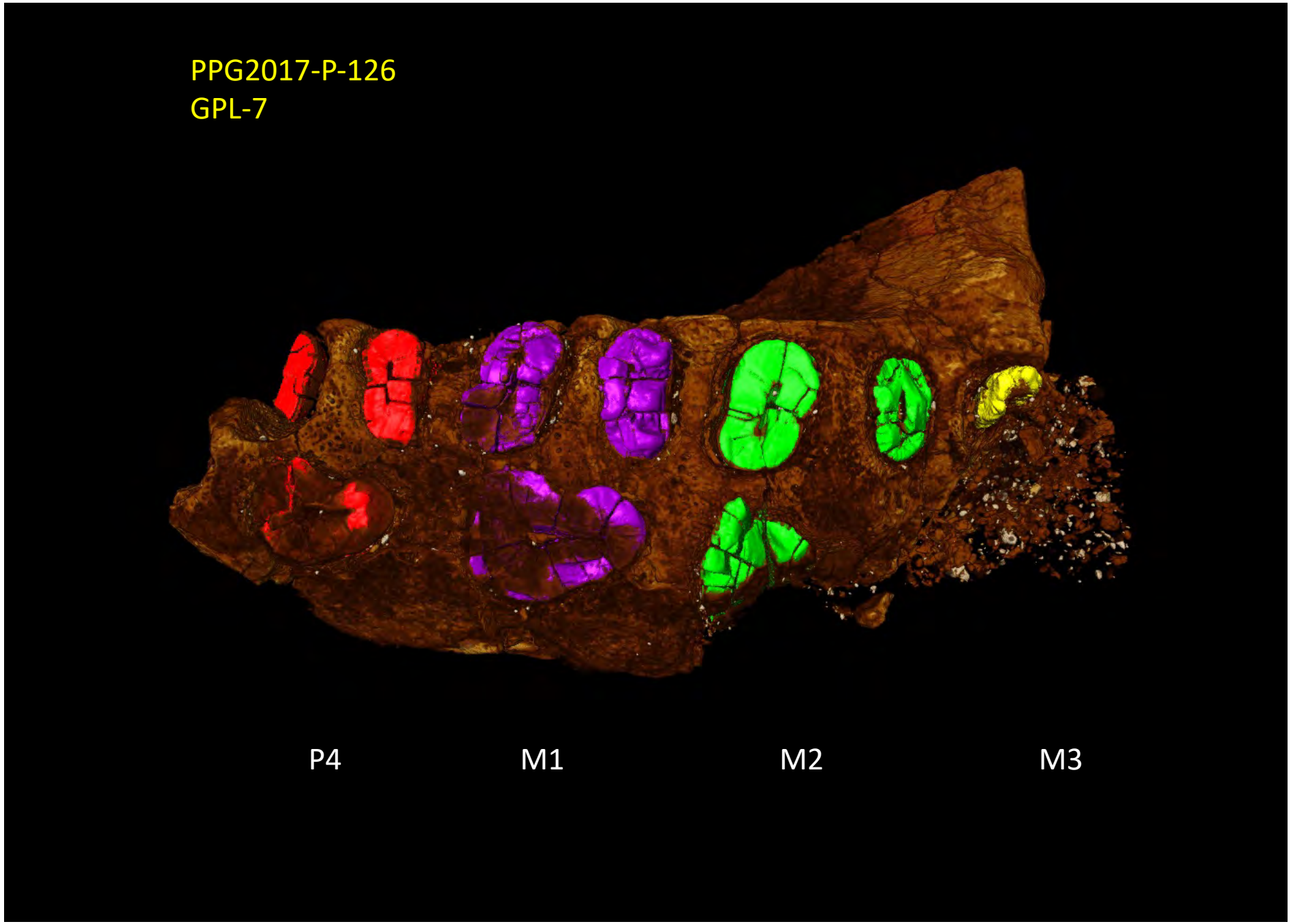

Fig. 17

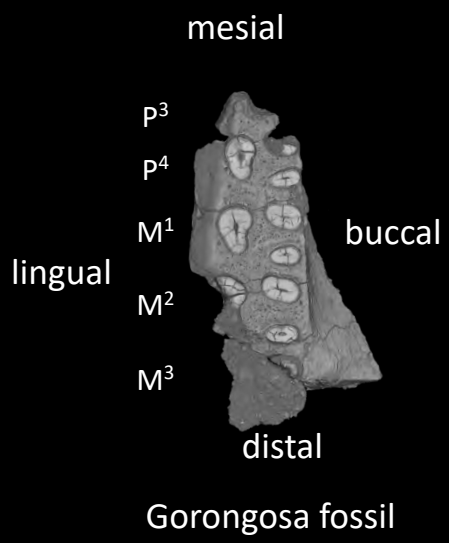

Gorongosa fossil

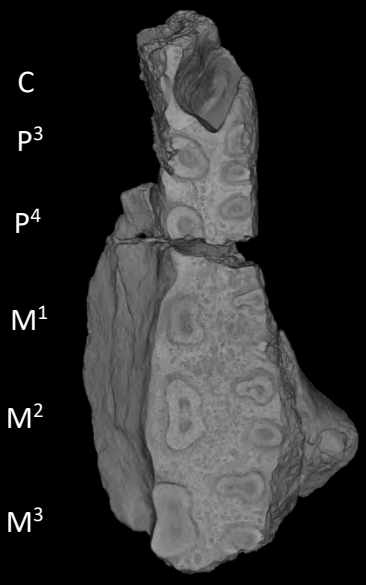

Samburupithecus kiptalami

Simiolus enjiessi

Rangwapithecus gordoni

Victoriapithecus macinnesi

Proconsul africanus

Papio angusticeps

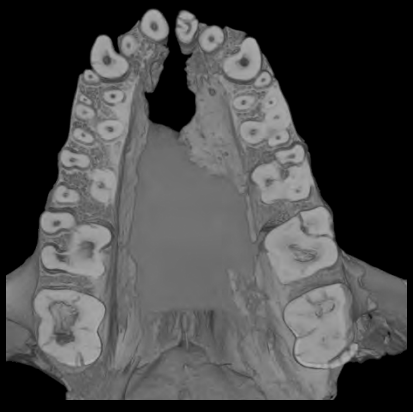

Theropithecus oswaldi

Cercopithecoides williamsi

3 cm

Fig. 18

a)

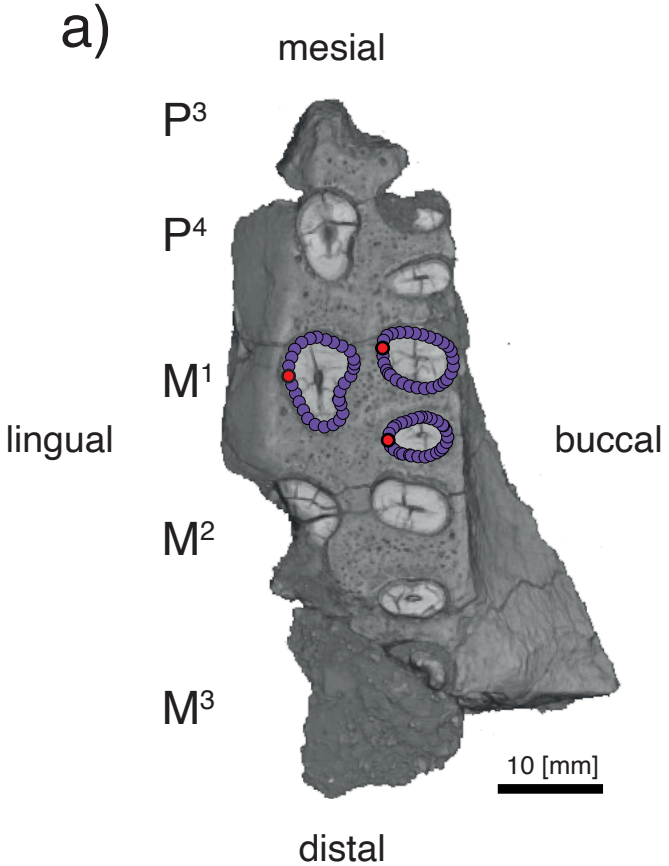
mesial
P3
P4
M1
M2
M3
lingual
buccal
10 [mm]
distal

b)

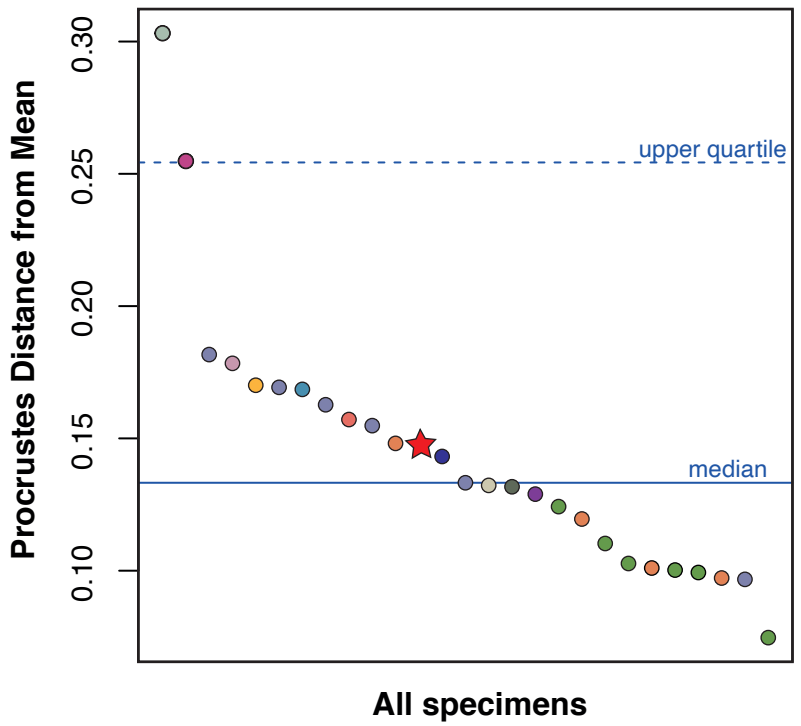
Procrustes Distance from Mean
0.30
0.25
0.20
0.15
0.10
upper quartile
median
All specimens

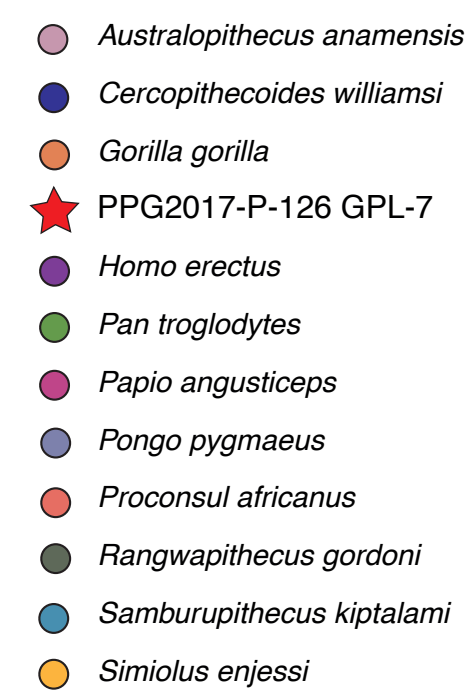
Australopithecus anamensis
Cercopithecoides williamsi
Gorilla gorilla
PPG2017-P-126 GPL-7
Homo erectus
Pan troglodytes
Papio angusticeps
Pongo pygmaeus
Proconsul africanus
Rangwapithecus gordoni
Samburupithecus kiptalami
Simiolus enjessi
Theropithecus oswaldi
Victoriapithecus macinnesi

c)

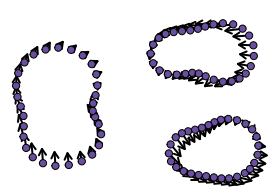

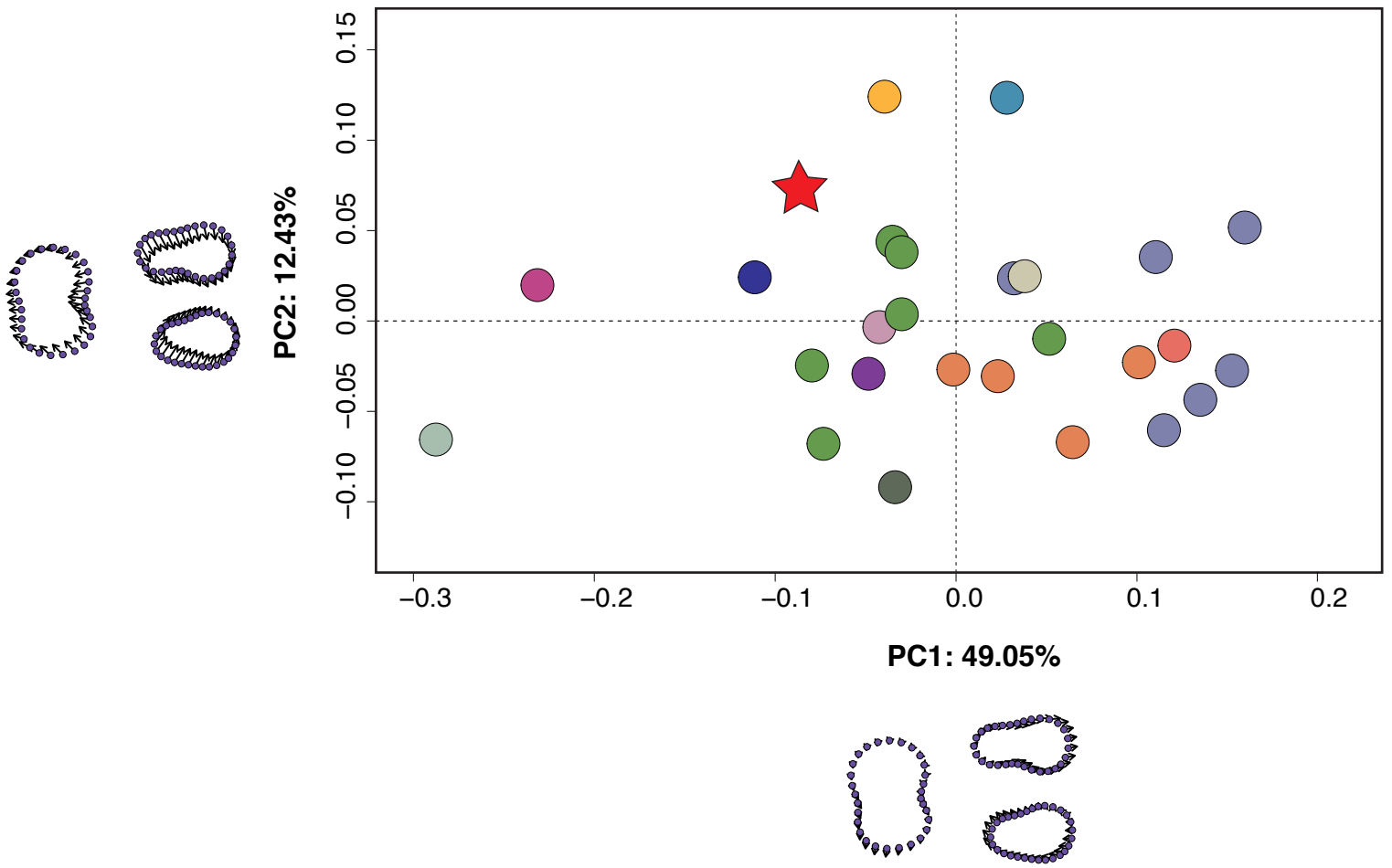
PC2: 12.43%
0.15
0.10
0.05
0.00
−0.05
−0.10
−0.3
−0.2
−0.1
0.0
0.1
0.2
PC1: 49.05%

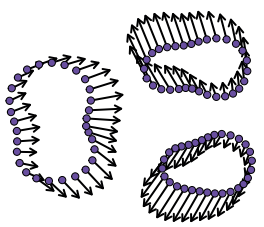


N
Gulley Survey (PPPG, 2018)
Areas surveyed
High density of fossils
Gorongosa Paleontological Localities
White Patches Survey (Pickford, 2013)
Invertebrates
Single vertebrate find
GPL-12
GPL-12B
White Patch 1 *Turritella* Site
White Patch 3 Mammal
White Patch 2 Mammal
White Patch 4 "Snails"
0
100
200 m

Table 1. Gorongosa Paleontological Localities

Locality	Elev	Facies
GPL-1	112	Conglomerate, sandstones, claystones, marlstones
GPL-2	120	Sandstones, claystone
GPL-3	116	Ssandstones, claystone
GPL-4	110	Conglomerates, quartzitic sandstone
GPL-5	99	Conglomerates, quartzitic sandstone
GPL-6	115	Sandstones, claystones
GPL-7	101	Siliciclastic sandstone, pebble lag
GPL-8	111	Conglomerate, sandstones
GPL-9	107	Conglomerate, sandstones
GPL-10	99	Sandstones
GPL-11	100	Rudstone, sandstones
GPL-12	114	Sandstones, claystones
Menguere Hill	108	Calcrete, silcrete
Mussapassua	160	Coarse quartzitic sands

Depositional environments	**Notes**
Fluvial to estuarine	First locality, abundant vertebrate fossils
Estuarine to shallow marine	Crustaceans, gastropods, bivalves
Estuarine to shallow marine	Crustaceans, gastropods, bivalves
Fluvial?	Surface stone tools (not in situ)
Fluvial?	Surface stone tools (not in situ)
Fluvial to estuarine, marine?	Large mammal bones
Fluvial	Mammal maxillary fragment
Fluvial, reworked estuarine/marine	*Striostera margaritacea* oyster
Fluvial, reworked estuarine/marine	Mollusks, red algae, serpulid
Coastal delta plain	Oysters, bivalves, crustaceans
Shallow marine	Abundant oysters, gastropods
Fluvial to estuarine	Richest vertebrate locality
Paleo-pan?	Fossil wood, tree trunks
Fluvial	Upper member Mazamba Fm

Table 2: Computed authigenic ages for the lower member of the Mazamba Formation

	Samples	(1) Considering Modern Environment equivalent		(2) Considering Modern Full Estuarine equivalent		(3) Considering Modern Source equivalent	
		Initial Authigenic $^{10}Be/^{9}Be$ $*10^{-8}$	Authigenic Age Ma	Initial Authigenic $^{10}Be/^{9}Be$ $*10^{-8}$	Authigenic Age Ma	Initial Authigenic $^{10}Be/^{9}Be$ $*10^{-8}$	Authigenic Age Ma
Lower Mazamba Formation	Be18-Gor-GPL1NE-1	13.867 ± 0.521	8.591 ± 0.179	0.640 ± 0.034	7.043 ± 0.190	0.226 ± 0.007	4.958 ± 0.165
	Be18-Gor-GPL1NE-2	13.867 ± 0.521	14.568 ± 0.268	0.640 ± 0.034	13.020 ± 0.273	0.226 ± 0.007	10.935 ± 0.252
	Be18-Gor-GPL1NE-3	0.640 ± 0.034	8.957 ± 0.199	0.640 ± 0.034	8.957 ± 0.199	0.226 ± 0.007	6.872 ± 0.173
	Be18-Gor-GPL1NE-4	0.640 ± 0.034	14.540 ± 0.519	0.640 ± 0.034	14.540 ± 0.519	0.226 ± 0.007	12.455 ± 0.508
	Be18-Gor-GPL1NE-5	0.640 ± 0.034	17.779 ± 0.696	0.640 ± 0.034	17.779 ± 0.696	0.226 ± 0.007	15.693 ± 0.687
	Be18-Gor-GPL1NE-6	0.640 ± 0.034	6.870 ± 0.227	0.640 ± 0.034	6.870 ± 0.227	0.226 ± 0.007	4.785 ± 0.206
	17-Gor-GPL2-5	0.640 ± 0.034	8.940 ± 0.186	0.640 ± 0.034	8.940 ± 0.186	0.226 ± 0.007	6.855 ± 0.158
	17-Gor-GPL2-10	0.640 ± 0.034	7.778 ± 0.201	0.640 ± 0.034	7.778 ± 0.201	0.226 ± 0.007	5.692 ± 0.176
	17-Gor-GPL6-3	0.640 ± 0.034	10.952 ± 0.225	0.640 ± 0.034	10.952 ± 0.225	0.226 ± 0.007	8.866 ± 0.201
	17-Gor-GPL6-8	0.640 ± 0.034	10.761 ± 0.308	0.640 ± 0.034	10.761 ± 0.308	0.226 ± 0.007	8.675 ± 0.291
	Be18-Gor-GPL12-0.1	13.867 ± 0.521	17.100 ± 0.450	0.640 ± 0.034	15.552 ± 0.452	0.226 ± 0.007	13.467 ± 0.439
	Be18-Gor-GPL12-1.1	13.867 ± 0.521	19.531 ± 0.842	0.640 ± 0.034	17.983 ± 0.843	0.226 ± 0.007	15.898 ± 0.835
	Be18-Gor-GPL12-3.1	0.640 ± 0.034	10.887 ± 0.233	0.640 ± 0.034	10.887 ± 0.233	0.226 ± 0.007	8.802 ± 0.209
	Be18-Gor-GPL12-4.1	13.867 ± 0.521	16.894 ± 0.570	0.640 ± 0.034	15.346 ± 0.572	0.226 ± 0.007	13.261 ± 0.562
	Be18-Gor-GPL12-5.1	0.226 ± 0.007	13.159 ± 0.288	0.640 ± 0.034	13.159 ± 0.288	0.226 ± 0.007	11.073 ± 0.268

Table 3: Stable carbon and oxygen isotopic values with sample ID, distance from the base of section GPL-1NE (for stratigraphic context see (Habermann et al 2019) and Fig. 3), amount of untreated carbonate powder and carbonate content.

Sample ID	Distance from base [cm]	$\delta^{13}C_{VPDB}$ [‰]	$\delta^{18}O_{VSMOW}$ [‰]	Weight [µg]	Carbonate content [%]
GLP1-1NE-25	390	-6.8	26.2	112	91
GLP1-1NE-24	385	-9.1	25.8	144	87
GLP1-1NE-23	380	-7.7	26.4	121	89
GLP1-1NE-22	360	-8.6	26.0	129	95
GPL1-1NE-21	350	-7.1	25.7	366	16
GLP1-1NE-19	340	-6.4	25.7	146	96
GLP1-1NE-18	335	-7.0	26.0	135	91
GLP1-1NE-17	330	-7.0	25.6	135	93
GLP1-1NE-16	325	-7.5	25.5	170	89
GLP1-1NE-15	320	-6.7	26.1	139	88
GLP1-1NE-14	310	-9.3	25.9	159	78
GPL1-1NE-13	200	-7.6	25.7	149	83
GPL1-1NE-10	145	-7.4	25.4	123	50
GPL1-1NE-09	135	-7.5	26.0	131	62
GPL1-1NE-08	120	-6.3	26.2	136	79
GPL1-1NE-07	110	-5.9	26.5	131	86
GPL1-1NE-06	90	-6.3	26.3	150	80

Table 4. Gorongosa Hyracoidea - measurements in mm

PPG2018-P-1	Side	mesio-distal	bucco-lingual
p1	Lt	12.81	n.a.
p2	Lt	14.64	n.a.
p3	Lt	14.96	n.a.
p4	Lt	15.72	n.a.
m1	Lt	17.59	n.a.
m2	Lt	19.61	n.a.
m3	Lt	31.01	n.a.
PPG2018-P-2			
p3	Rt	14.48	8.93
p4	Rt	16.14	10.26
m1	Rt	16.63	12.60
m2	Rt	20.77	15.31
m3	Rt	32.40	14.46

Supplementary Table S1: Sampling details for rock samples from the lower member of the Mazamba Formation and modern sediment samples taken for atmospheric ^{10}Be dating.

Sample ID	Sample type	Locality/site	Decimal degree		Lithology	Sedimentary environment (interpreted for "fossil" samples)	Sampling depth below surface
			°S	°E			
Be18-Gor-GPL1NE-1	Fossil	GPL1NE_section base	-18.9288	34.6476	coarse carbonate-cemented sandstone	fluvial, alluvial channel	excavated trench wall
Be18-Gor-GPL1NE-2	Fossil	GPL1NE	-18.9288	34.6476	clay-bearing sandstone	fluvio-deltaic	excavated trench wall
Be18-Gor-GPL1NE-3	Fossil	GPL1NE	-18.9288	34.6476	sandy claystone	estuarine, central basin/swamp	excavated trench wall
Be18-Gor-GPL1NE-4	Fossil	GPL1NE	-18.9288	34.6476	clayey sandstone	fluvio-deltaic, distributary channel	excavated trench wall
Be18-Gor-GPL1NE-5	Fossil	GPL1NE	-18.9288	34.6476	sandy claystone	estuarine, central basin/swamp	excavated trench wall
Be18-Gor-GPL1NE-6	Fossil	GPL1NE_section top	-18.9288	34.6476	sandy clay- to marlstone	estuarine, central basin	excavated trench wall
Be18-Gor-GPL12-0.1	Fossil	GPL12, STP101_section base	-18.9337	34.6456	coarse carbonate-cemented sandstone	fluvial, alluvial channel	excavated trench wall
Be18-Gor-GPL12-1.1	Fossil	GPL12, STP101	-18.9337	34.6456	coarse carbonate-cemented reddish sandstone	fluvio-deltaic	excavated trench wall
Be18-Gor-GPL12-3.1	Fossil	GPL12, STP101	-18.9337	34.6456	brown-beige sandy claystone	estuarine, central basin/swamp	excavated trench wall
Be18-Gor-GPL12-4.1	Fossil	GPL12, STP101	-18.9337	34.6456	brown-beige clayey sandstone	fluvio-deltaic, distributary channel	excavated trench wall
Be18-Gor-GPL12-5.1	Fossil	GPL12, STP101_section top	-18.9337	34.6456	olive-green claystone	estuarine, central basin	excavated trench wall
17-Gor-GPL6-8	Fossil	GPL6 section base	-18.9271	34.6530	clayey sandstone	estuarine, central basin/swamp	excavated section wall
17-Gor-GPL6-3	Fossil	GPL6 section center	-18.9271	34.6530	laminated claystone	estuarine, central basin/swamp	excavated section wall
17-Gor-GPL2-5	Fossil	GPL2 section base	-18.9070	34.6757	clayey olive-brown sanstone	estuarine/marine, lagoonal shelf/barrier	excavated section wall
17-Gor-GPL2-10	Fossil	GPL2 section top	-18.9070	34.6757	olive clayey sandstone	estuarine/marine, lagoonal shelf/barrier	excavated section wall
Be18-Gor-Pu-2	Modern	Pungwe River	-18.9944	34.3494	sandy clay	fluvial, alluvial floodplain c. 200 m north of river	60 cm, ca. 2-3 m above water level
Be18-Gor-Urem-1.1	Modern	Urema River	-18.9878	34.5693	dark-brown sandy clay/mud	fluvial, riverbank	30 cm, at water level
Be18-Gor-Vun-1.1	Modern	Vunduzi River (?)	-18.4805	34.2103	muddy coarse sand	fluvial, riverbank	water-sediment interface at 1 cm water depth
Be18-Gor-VunS1-1.1	Modern	Stream S of Vunduzi River	-18.4899	34.2011	sandy mud	fluvial, riverbank	water-sediment interface at 1 cm water depth
Be18-Gor-Muc-1.1	Modern	Mucuro Mazi River	-18.5187	34.1915	muddy sand	fluvial, riverbank	water-sediment interface at 1 cm water depth
Be18-Gor-LUrem-1.1	Modern	Lake Urema	-18.9130	34.5178	muddy sand	fluvio-lacustrine, lakeshore	30 cm, at water level
Be18-Bei-EstRi1-1	Modern	1st estuary NE Beira	-19.7873	34.9609	muddy sand	fluvio-deltaic, river-dominated estuary shore	20 cm, ca. 1 cm above water level
Be18-Bei-SavEst-1	Modern	Savane River estuary NE Beira	-19.6806	35.1396	organic-rich sandy mud/clay	lagoonal estuary shore on mangrove-dominated barrier peninsular	surface at water level
Be18-Bei-SavFor-1	Modern	Savane River estuary NE Beira	-19.6821	35.1399	organic-rich sandy mud/clay	mangrove forest/swamp on lagoonal barrier peninsular	20 cm, ca. 0.5 m above water level

Supplementary Table S2: ^{10}Be and ^{9}Be concentrations and $^{10}Be/^{9}Be$ ratios for the Gorongosa samples

	Samples	Depth [m]	Sample weight [g]	Measured (^{10}Be /^{9}Be) $*10^{-13}$	Authigenic ^{9}Be $*10^{16}$ [at.g^{-1}]	Authigenic ^{10}Be $*10^{7}$ [at.g^{-1}]	Authigenic ^{10}Be /^{9}Be $*10^{-8}$
Modern	Be18-Gor-Pu-2		0,9593	106,6344 ± 2,1964	5,1161 ± 0,1496	22,6219 ± 0,4653	4,4217 ± 0,3162
	Be18-Gor-Urem-1.1		0,9584	89,1654 ± 1,9579	7,9130 ± 0,2405	18,9476 ± 0,4153	2,3945 ± 0,1795
	Be18-Gor-Vun-1.1		0,9596	15,8407 ± 0,4884	1,6814 ± 0,0095	3,3464 ± 0,1021	1,9902 ± 0,1235
	Be18-Gor-VunS1-1.1		0,9574	86,4330 ± 1,8054	7,5941 ± 0,0724	18,3644 ± 0,3829	2,4182 ± 0,1109
	Be18-Gor-Muc-1.1		0,9585	84,7570 ± 2,1050	2,6621 ± 0,1283	17,9818 ± 0,4458	6,7548 ± 0,7323
	Be18-Gor-Lurem-1.1		0,9624	70,8797 ± 1,7002	3,3840 ± 0,1200	14,9327 ± 0,3574	4,4127 ± 0,3776
	Be18-Bei-EstRi1-1		0,9585	280,9860 ± 5,0466	4,2827 ± 0,0239	59,3875 ± 1,0660	13,8668 ± 0,5213
	Be18-Bei-SavEst-1		0,9583	77,6644 ± 1,8204	2,3125 ± 0,0795	16,4663 ± 0,3852	7,1206 ± 0,5920
	Be18-Bei-SavFor-1		0,9583	75,6599 ± 1,9046	2,6573 ± 0,0655	16,0133 ± 0,4023	6,0262 ± 0,4240
Lower Mazamba Formation	Be18-Gor-GPL1NE-1 (2)		0,9162	1,7757 ± 0,0005	0,0137 ± 0,0569	0,5941 ± 0,0186	0,1894 ± 0,0137
	Be18-Gor-GPL1NE-2		0,9174	0,1918 ± 0,0008	0,0011 ± 0,1369	0,0610 ± 0,0032	0,0096 ± 0,0011
	Be18-Gor-GPL1NE-3		0,9137	1,2693 ± 0,0005	0,0054 ± 0,1006	0,4189 ± 0,0137	0,0728 ± 0,0054
	Be18-Gor-GPL1NE-4 (2)		0,9158	0,0383 ± 0,0018	0,0011 ± 0,0457	0,0125 ± 0,0015	0,0045 ± 0,0011
	Be18-Gor-GPL1NE-5		0,9172	0,0082 ± 0,0024	0,0003 ± 0,0490	0,0027 ± 0,0005	0,0009 ± 0,0003
	Be18-Gor-GPL1NE-6 (2)		0,9151	2,6210 ± 0,0004	0,0196 ± 0,1535	0,8776 ± 0,0272	0,2065 ± 0,0196
	17-Gor-GPL2-5		0,9167	1,5327 ± 0,0005	0,0048 ± 0,0700	0,5178 ± 0,0162	0,0734 ± 0,0048
	17-Gor-GPL2-10 (2)		0,9174	1,9923 ± 0,0006	5,0197 ± 0,1192	0,6586 ± 0,0203	0,1312 ± 0,0102
	17-Gor-GPL6-3		0,9173	0,4146 ± 0,0006	0,0023 ± 0,0873	0,1396 ± 0,0056	0,0269 ± 0,0023
	17-Gor-GPL6-8		0,9192	0,1950 ± 0,0009	0,0040 ± 0,0568	0,0653 ± 0,0041	0,0296 ± 0,0040
	Be18-Gor-GPL12-0.1 (2)		0,9174	0,0464 ± 0,0015	0,0006 ± 0,1541	0,0156 ± 0,0016	0,0027 ± 0,0006
	Be18-Gor-GPL12-1.1		0,9174	0,0103 ± 0,0030	0,0003 ± 0,0754	0,0035 ± 0,0007	0,0008 ± 0,0003
	Be18-Gor-GPL12-3.1 (2)		0,9175	0,4907 ± 0,0006	0,0025 ± 0,0883	0,1649 ± 0,0071	0,0277 ± 0,0025
	Be18-Gor-GPL12-4.1		0,9191	0,0423 ± 0,0019	0,0008 ± 0,1172	0,0141 ± 0,0019	0,0030 ± 0,0008
	Be18-Gor-GPL12-5.1 (2)		0,9168	0,1879 ± 0,0009	0,0011 ± 0,0901	0,0630 ± 0,0037	0,0089 ± 0,0011

Supplementary Table S3: Results of $^{26}Al/^{10}Be$ analyses

Sample	Depth (cm)	Depth ($g.cm^{-2}$)	Dissolved quartz (g)	^{9}Be carrier (10^{19} at.)	^{10}Be (10^{5} at.g^{-1})	^{26}Al (10^{5} at.g^{-1})	$^{26}Al/^{10}Be$
16-Gor-Muss-7	1500	3750	20,1345	3,0244	9909,71 ± 1328,88	37881,44 ± 14645,17	3,8227 ± 1,5642
16-Gor-Muss-8	1050	2625	20,1432	3,0511	11973,11 ± 1589,53	57683,13 ± 13054,15	4,8177 ± 1,2640

Supplementary Table S4: Model outputs of burial durations and denudation rates

Sample	Model Without Post-B production		Model With Post-B. production				
	Denud. before burial ($m.Ma^{-1}$)	Min Burial duration (ka)	Denud. before B. ($m.Ma^{-1}$)	Max Burial duration (ka)	Denud. after B. ($m.Ma^{-1}$)	% [^{10}Be] Post-B.	% [^{26}Al] Post-B.
16-Gor-Muss-7	140,04	1 316,25 ± 539,66	1 054,85	971,99 ± 398,52	20,93	84	81
16-Gor-Muss-8	147,30	838,16 ± 220,96	1 746,90	971,99 ± 256,24	20,93	92	92

Supplementary Table S5. Miocene sharks

Specimen Number	n	Source/Museum	Locality	Epoch	Species	Reference
MPEG-1131-V	1	Aguilera et al. 2017	Brazil	Early Miocene	†*Carcharhinus ackermannii*	doi:10.1371/journal.pone.0182740
AMU-CURS-990	1	Carrillo-Briceño et al. 2016	Venezuela	Early Miocene	†*Carcharhinus brachyurus*	doi:10.5167/uzh-125933
MUN-STRI-43808	1	Carrillo-Briceño et al. 2019	Colombia	Middle Miocene	†*Carcharhinus gibbesii*	doi:10.5194/bg-16-33-2019
MPEG-1836-V	1	Aguilera et al. 2017	Brazil	Early Miocene	†*Carcharhinus perezi*	doi:10.1371/journal.pone.0182740
UAP-14.181-14	1	Andrianavalona et al. 2015	NW Madagascar	Miocene	†*Carcharhinus priscus*	doi:10.1371/journal.pone.0129444
UAP-13.159	1	Andrianavalona et al. 2015	NW Madagascar	Miocene	†*Carcharhinus* sp.	doi:10.1371/journal.pone.0129444
AMU-CURS-647	1	Carrillo-Briceño et al. 2016	Venezuela	Early Miocene	†*Galeocerdo aduncus*	doi:10.5167/uzh-125933
AMU-CURS-730	1	Carrillo-Briceño et al. 2016	Venezuela	Early Miocene	†*Galeocerdo aduncus*	doi:10.5167/uzh-125933
LPN 162	1	Capetta, 1970	France (Montpellier)	Miocene	†*Galeocerdo aduncus*	CAPPETTA, Hemipristis (1970) Les Sélaciens du Miocène de la région de Montpellier. Palaeovertebrata, Mémoire extraordinaire 1970: 139 p., 22 fig., 27 pl.
LPN 163	1	Capetta, 1970	France (Montpellier)	Miocene	†*Galeocerdo aduncus*	CAPPETTA, Hemipristis (1970) Les Sélaciens du Miocène de la région de Montpellier. Palaeovertebrata, Mémoire extraordinaire 1970: 139 p., 22 fig., 27 pl.
MUSM 3262	2	Landini et al. 2017	Peru	Late Miocene	†*Galeocerdo aduncus*	doi:10.1016/j.jsames.2016.12.010
NA	1	Pawellek et al. 2012	Lybia	Early Pliocene	*Galeocerdo cuvier*	doi:10.1127/0077-7749/2012/0272
105Z100	1	Argyriou et al. 2015	Lybia	Early Miocene	†*Galeocerdo mayumbensis*	doi:10.1016/j.jafrearsci.2014.11.008
112Z100	1	Argyriou et al. 2015	Lybia	Early Miocene	†*Galeocerdo mayumbensis*	doi:10.1016/j.jafrearsci.2014.11.008
AMU-CURS-646	1	Carrillo-Briceño et al. 2016	Venezuela	Early Miocene	†*Galeocerdo mayumbensis*	doi:10.5167/uzh-125933
AMU-CURS-995	1	Carrillo-Briceño et al. 2016	Venezuela	Early Miocene	†*Galeocerdo mayumbensis*	doi:10.5167/uzh-125933
MPEG-1710-V	1	Aguilera et al. 2017	Brazil	Early Miocene	†*Galeocerdo mayumbensis*	doi:10.1371/journal.pone.0182740
MPEG-177-V	1	Aguilera et al. 2017	Brazil	Early Miocene	†*Galeocerdo mayumbensis*	doi:10.1371/journal.pone.0182740
MPEG-1854-V	1	Aguilera et al. 2017	Brazil	Early Miocene	†*Galeocerdo mayumbensis*	doi:10.1371/journal.pone.0182740
UAP-13.167	1	Andrianavalona et al. 2015	NW Madagascar	Miocene	†*Galeocerdo mayumbensis*	doi:10.1371/journal.pone.0129444
UAP-13.172	1	Andrianavalona et al. 2015	NW Madagascar	Miocene	†*Galeocerdo mayumbensis*	doi:10.1371/journal.pone.0129444
MPEG-781-V	1	Aguilera et al. 2017	Brazil	Early Miocene	†*Hemipristis serra*	doi:10.1371/journal.pone.0182740
MUN-STRI-34790	2	Carrillo-Briceño et al. 2019	Colombia	Middle Miocene	†*Hemipristis serra*	doi:10.5194/bg-16-33-2019
MUN-STRI-41132	1	Carrillo-Briceño et al. 2019	Colombia	Middle Miocene	†*Physogaleus contortus*	doi:10.5194/bg-16-33-2019
AMU-CURS-648	1	Carrillo-Briceño et al. 2016	Venezuela	Early Miocene	†*Physogaleus contortus*	doi:10.5167/uzh-125933
AMU-CURS-719	1	Carrillo-Briceño et al. 2016	Venezuela	Early Miocene	†*Physogaleus contortus*	doi:10.5167/uzh-125933
MUSM 3261	1	Landini et al. 2017	Peru	Late Miocene	†*Physogaleus contortus*	doi:10.1016/j.jsames.2016.12.010
EMRG-Chond-T-76	59	Institute of Palaeontology, Vertebrate Collection, University of Vienna (David J. Ward)	USA (North Carolina)	Early Miocene	†*Galeocerdo aduncus*	doi:10.1017/pab.2021.6
NA	6	Haimuseum Aathal Switzerland	Germany	Miocene	†*Galeocerdo aduncus*	doi:10.1017/pab.2021.6
KM_DJ.033	3	Haimuseum Aathal Switzerland	Germany	Oligocene	†*Galeocerdo aduncus*	doi:10.1017/pab.2021.6
2012/0017/0240	14	Natural History Museum Vienna	USA (Florida)	Miocene	†*Galeocerdo aduncus*	doi:10.1017/pab.2021.6
UF 116830	2	Florida Museum of Natural History	USA (Florida)	Middle Miocene	†*Galeocerdo aduncus*	doi:10.1017/pab.2021.6
UF 217131	5	Florida Museum of Natural History	USA (Florida)	Middle Miocene	†*Galeocerdo aduncus*	doi:10.1017/pab.2021.6
UF 231021	1	Florida Museum of Natural History	USA (Florida)	Middle Miocene	†*Galeocerdo aduncus*	doi:10.1017/pab.2021.6
UF 232403	16	Florida Museum of Natural History	USA (Florida)	Middle Miocene	†*Galeocerdo aduncus*	doi:10.1017/pab.2021.6
UF 232425	1	Florida Museum of Natural History	USA (Florida)	Middle Miocene	†*Galeocerdo aduncus*	doi:10.1017/pab.2021.6
UF 234253	1	Florida Museum of Natural History	USA (Florida)	Middle Miocene	†*Galeocerdo aduncus*	doi:10.1017/pab.2021.6
UF 240484	7	Florida Museum of Natural History	USA (Florida)	Late Miocene	†*Galeocerdo aduncus*	doi:10.1017/pab.2021.6
UF 278633	1	Florida Museum of Natural History	USA (Florida)	Middle Miocene	†*Galeocerdo aduncus*	doi:10.1017/pab.2021.6
UF 28780	4	Florida Museum of Natural History	USA (Florida)	Middle Miocene	†*Galeocerdo aduncus*	doi:10.1017/pab.2021.6
UF/TRO 15237	1	Florida Museum of Natural History	USA (Florida)	Late Miocene	†*Galeocerdo aduncus*	doi:10.1017/pab.2021.6
24756	3	National Museum of Natural History, Washington, D.C.	USA (North Carolina)	Miocene	†*Galeocerdo aduncus*	doi:10.1017/pab.2021.6
287850	27	National Museum of Natural History, Washington, D.C.	USA (North Carolina)	Miocene	†*Galeocerdo aduncus*	doi:10.1017/pab.2021.6
KF-17E	1	Patnaik et al. 2014	India (Gujarat)	Early Miocene	†*Galeocerdo bigelowi*	doi:10.1017/pab.2021.6
NA	1	Lawley 1881	Italy (Tuscany)	Pliocene	†*Galeocerdo capellini*	doi:10.1017/pab.2021.6
IGM 5854	1	Universidad Nacional Autónoma de México	Mexico	Pliocene	†*Galeocerdo capellini*	doi:10.1017/pab.2021.6
1281	25	Universidad Nacional Autónoma de México	Mexico	Pliocene	†*Galeocerdo capellini*	doi:10.1017/pab.2021.6
S216(P49)	1	Müller 1999	USA (North Carolina)	Early Miocene	†*Galeocerdo casei*	doi:10.1017/pab.2021.6
S217(P49)	1	Müller 1999	USA (North Carolina)	Early Miocene	†*Galeocerdo casei*	doi:10.1017/pab.2021.6
P.30501	1	Natural History Museum London	USA (Alabama)	Early Eocene	†*Galeocerdo clarkensis*	doi:10.1017/pab.2021.6
P.30465-7	1	Natural History Museum London	USA (Alabama)	Early Eocene	†*Galeocerdo clarkensis*	doi:10.1017/pab.2021.6
NA	25	Haimuseum Aathal Switzerland	USA (South Carolina)	Late Eocene	†*Galeocerdo clarkensis*	doi:10.1017/pab.2021.6
UF 65552	1	Florida Museum of Natural History	USA (Florida)	Middle Miocene	*Galeocerdo cuvier*	doi:10.1017/pab.2021.6
NA	3	Haimuseum Aathal Switzerland	USA (Florida)	Miocene	*Galeocerdo cuvier*	doi:10.1017/pab.2021.6
NA	5	Haimuseum Aathal Switzerland	USA (North Carolina)	Late Miocene	*Galeocerdo cuvier*	doi:10.1017/pab.2021.6
NA	2	Florida Museum of Natural History	USA (North Carolina)	Pliocene	*Galeocerdo cuvier*	doi:10.1017/pab.2021.6
NA	1	Florida Museum of Natural History	USA (South Carolina)	Early Pliocene	*Galeocerdo cuvier*	doi:10.1017/pab.2021.6
NA	1	Florida Museum of Natural History	USA (North Carolina)	Miocene	*Galeocerdo cuvier*	doi:10.1017/pab.2021.6
EJ-XX-427	1	Florida Museum of Natural History	USA (Florida)	Miocene	*Galeocerdo cuvier*	doi:10.1017/pab.2021.6
UF/TRO 11181	1	Florida Museum of Natural History	USA (Florida)	Early Pliocene	*Galeocerdo cuvier*	doi:10.1017/pab.2021.6
UF/TRO 15482	3	Florida Museum of Natural History	USA (Florida)	Early Pliocene	*Galeocerdo cuvier*	doi:10.1017/pab.2021.6
UF/TRO 14220	3	Florida Museum of Natural History	USA (Florida)	Early Pliocene	*Galeocerdo cuvier*	doi:10.1017/pab.2021.6
UF 17860	2	Florida Museum of Natural History	USA (Florida)	Early Pliocene	*Galeocerdo cuvier*	doi:10.1017/pab.2021.6
UF 227304	1	Florida Museum of Natural History	USA (Florida)	Early Pliocene	*Galeocerdo cuvier*	doi:10.1017/pab.2021.6
UF 227889	1	Florida Museum of Natural History	USA (Florida)	Early Pliocene	*Galeocerdo cuvier*	doi:10.1017/pab.2021.6
UF 227871	2	Florida Museum of Natural History	USA (Florida)	Early Pliocene	*Galeocerdo cuvier*	doi:10.1017/pab.2021.6
UF 228801	1	Florida Museum of Natural History	USA (Florida)	Early Pliocene	*Galeocerdo cuvier*	doi:10.1017/pab.2021.6
UF/TRO 3801	3	Florida Museum of Natural History	USA (Florida)	Early Pliocene	*Galeocerdo cuvier*	doi:10.1017/pab.2021.6
UF/TRO 3876	3	Florida Museum of Natural History	USA (Florida)	Early Pliocene	*Galeocerdo cuvier*	doi:10.1017/pab.2021.6
UF/TRO 5438	4	Florida Museum of Natural History	USA (Florida)	Early Pliocene	*Galeocerdo cuvier*	doi:10.1017/pab.2021.6
UF/TRO 5603	1	Florida Museum of Natural History	USA (Florida)	Early Pliocene	*Galeocerdo cuvier*	doi:10.1017/pab.2021.6
UF/TRO 5679	1	Florida Museum of Natural History	USA (Florida)	Early Pliocene	*Galeocerdo cuvier*	doi:10.1017/pab.2021.6
UF/TRO 5700	2	Florida Museum of Natural History	USA (Florida)	Early Pliocene	*Galeocerdo cuvier*	doi:10.1017/pab.2021.6
UF/TRO 5745	2	Florida Museum of Natural History	USA (Florida)	Early Pliocene	*Galeocerdo cuvier*	doi:10.1017/pab.2021.6
UF/TRO 8604	1	Florida Museum of Natural History	USA (Florida)	Early Pliocene	*Galeocerdo cuvier*	doi:10.1017/pab.2021.6
UF/TRO 8935	1	Florida Museum of Natural History	USA (Florida)	Early Pliocene	*Galeocerdo cuvier*	doi:10.1017/pab.2021.6
UF/TRO 9227	2	Florida Museum of Natural History	USA (Florida)	Early Pliocene	*Galeocerdo cuvier*	doi:10.1017/pab.2021.6
EMRG-Chond-J-9	38	Institute of Palaeontology, Vertebrate Collection, University of Vienna	South-east Asia	Extant	*Galeocerdo cuvier*	doi:10.1017/pab.2021.6
EMRG-Chond-J-10	41	Institute of Palaeontology, Vertebrate Collection, University of Vienna	South-east Asia	Extant	*Galeocerdo cuvier*	doi:10.1017/pab.2021.6
EMRG-Chond-J-16	45	Institute of Palaeontology, Vertebrate Collection, University of Vienna	?	Extant	*Galeocerdo cuvier*	doi:10.1017/pab.2021.6
DGM 653-P	1	dos Reis 2005	Brasil (Pará)	Miocene	*Galeocerdo cuvier*	doi:10.1017/pab.2021.6
NA	1	Davis 1888	New Zealand	Middle Miocene	†*Galeocerdo davisi*	doi:10.1017/pab.2021.6
NA	14	Haimuseum Aathal Switzerland	Morocco (Ad Dakhla)	Late Eocene	†*Galeocerdo eaglesomei*	doi:10.1017/pab.2021.6
CGM 60025	1	Underwood et al. 2011	Egypt	Middle Eocene	†*Galeocerdo eaglesomei*	doi:10.1017/pab.2021.6
PAL 13577	1	Natural History Museum London	Nigeria	Middle Eocene	†*Galeocerdo eaglesomei*	doi:10.1017/pab.2021.6
P.13578	1	Natural History Museum London	Nigeria	Middle Eocene	†*Galeocerdo eaglesomei*	doi:10.1017/pab.2021.6
P.13579	1	Natural History Museum London	Nigeria	Middle Eocene	†*Galeocerdo eaglesomei*	doi:10.1017/pab.2021.6
P.13580	1	Natural History Museum London	Nigeria	Middle Eocene	†*Galeocerdo eaglesomei*	doi:10.1017/pab.2021.6
P.13581	1	Natural History Museum London	Nigeria	Middle Eocene	†*Galeocerdo eaglesomei*	doi:10.1017/pab.2021.6
P.13582	1	Natural History Museum London	Nigeria	Middle Eocene	†*Galeocerdo eaglesomei*	doi:10.1017/pab.2021.6
P.13583	1	Natural History Museum London	Nigeria	Middle Eocene	†*Galeocerdo eaglesomei*	doi:10.1017/pab.2021.6
P.13586	1	Natural History Museum London	Nigeria	Middle Eocene	†*Galeocerdo eaglesomei*	doi:10.1017/pab.2021.6
P.13588	1	Natural History Museum London	Nigeria	Middle Eocene	†*Galeocerdo eaglesomei*	doi:10.1017/pab.2021.6
P.13589	1	Natural History Museum London	Nigeria	Middle Eocene	†*Galeocerdo eaglesomei*	doi:10.1017/pab.2021.6

P.13591	1	Natural History Museum London	Nigeria	Middle Eocene	†*Galeocerdo eaglesomei*	doi:10.1017/pab.2021.6
P.13592	1	Natural History Museum London	Nigeria	Middle Eocene	†*Galeocerdo eaglesomei*	doi:10.1017/pab.2021.6
P.13593	1	Natural History Museum London	Nigeria	Middle Eocene	†*Galeocerdo eaglesomei*	doi:10.1017/pab.2021.6
P.73677	1	Natural History Museum London	Morocco (Ad Dakhla)	Late Eocene	†*Galeocerdo eaglesomei*	doi:10.1017/pab.2021.6
L.U. 211	1	Tewari et al. 1960	India (Gujarat)	Early Miocene	†*Galeocerdo gajensis*	doi:10.1017/pab.2021.6
DJ.033	1	Haimuseum Aathal Switzerland	USA (Texas)	Eocene	†*Galeocerdo latidens*	doi:10.1017/pab.2021.6
DJ.033	3	Haimuseum Aathal Switzerland	Great Britain	Eocene	†*Galeocerdo latidens*	doi:10.1017/pab.2021.6
NA	6	Haimuseum Aathal Switzerland	Togo	Late Eocene	†*Galeocerdo latidens*	doi:10.1017/pab.2021.6
NA	1	Haimuseum Aathal Switzerland	Morocco (Ad Dakhla)	Late Eocene	†*Galeocerdo latidens*	doi:10.1017/pab.2021.6
NA	3	Haimuseum Aathal Switzerland	Great Britain (Sussex)	Eocene	†*Galeocerdo latidens*	doi:10.1017/pab.2021.6
	1	D. J. Kemp	Great Britain (Hampshire)	Eocene	†*Galeocerdo latidens*	doi:10.1017/pab.2021.6
NA	2	D. J. Kemp	Great Britain (Hampshire)	Eocene	†*Galeocerdo latidens*	doi:10.1017/pab.2021.6
DTK 14-19/9/85	2	D. J. Kemp	Great Britain (Hampshire)	Eocene	†*Galeocerdo latidens*	doi:10.1017/pab.2021.6
DTK:2000.95.12.1	3	D. J. Kemp	Great Britain (Hampshire)	Eocene	†*Galeocerdo latidens*	doi:10.1017/pab.2021.6
CGM 60026	1	Underwood et al. 2011	Egypt	Eocene	†*Galeocerdo latidens*	doi:10.1017/pab.2021.6
NA	10	Haimuseum Aathal Switzerland	USA (Florida)	Miocene	†*Galeocerdo mayumbensis*	doi:10.1017/pab.2021.6
UF 232399	4	Florida Museum of Natural History	USA (Florida)	Middle Miocene	†*Galeocerdo mayumbensis*	doi:10.1017/pab.2021.6
UF/TRO 6017	6	Florida Museum of Natural History	USA (Florida)	Middle Miocene	†*Galeocerdo mayumbensis*	doi:10.1017/pab.2021.6
UF/V 4963	1	Florida Museum of Natural History	USA (Florida)	Early Miocene	†*Galeocerdo mayumbensis*	doi:10.1017/pab.2021.6
UF/V 4988	1	Florida Museum of Natural History	USA (Florida)	Early Miocene	†*Galeocerdo mayumbensis*	doi:10.1017/pab.2021.6
UF/V 5118	1	Florida Museum of Natural History	USA (Florida)	Early Miocene	†*Galeocerdo mayumbensis*	doi:10.1017/pab.2021.6
UF/V 2676	1	Florida Museum of Natural History	USA (Florida)	Early Miocene	†*Galeocerdo mayumbensis*	doi:10.1017/pab.2021.6
UF/V 4181	2	Florida Museum of Natural History	USA (Florida)	Early Miocene	†*Galeocerdo mayumbensis*	doi:10.1017/pab.2021.6
NRPS-P12007	5	Swedish Museum of Natural History, Stockholm	New Guinea	Miocene	†*Galeocerdo mayumbensis*	doi:10.1017/pab.2021.6
N. 653-P--D.G.M.-D.N.I	1	da Silva Santos & Travassos 1960	Brasil (Pará)	Early Miocene	†*Galeocerdo paulinoi*	doi:10.1017/pab.2021.6
334960	3	National Museum of Natural History, Washington, D.C.	USA (Maryland)	Middle Miocene	†*Galeocerdo triqueter*	doi:10.1017/pab.2021.6
DJ.034	2	Haimuseum Aathal Switzerland	USA (Georgia)	Eocene	†*Hemipristis curvatus*	doi:10.1017/pab.2021.6
NA	3	Haimuseum Aathal Switzerland	Morocco (Ad Dakhla)	Late Eocene	†*Hemipristis curvatus*	doi:10.1017/pab.2021.6
NA	6	Haimuseum Aathal Switzerland	USA (Arkansas)	Early Pliocene	†*Hemipristis serra*	doi:10.1017/pab.2021.6
7-298	1	Haimuseum Aathal Switzerland	USA (California)	Miocene	†*Hemipristis serra*	doi:10.1017/pab.2021.6
NA	1	Leriche 1910	France (Paris Basin)	Oligocene early	†*Physogaleus acutus*	doi:10.1017/pab.2021.6
PAL366457	1	National Museum of Natural History, Washington, D.C.	USA (Alabama)	Early Eocene	†*Physogaleus alabamensis*	doi:10.1017/pab.2021.6
5361/15	1	Malyshkina et al. 2013	Ukraine (Crimea)	Middle Eocene	†*Physogaleus alabamensis*	doi:10.1017/pab.2021.6
KM_EZ-AF GA/Ca 7-19	1	Haimuseum Aathal Switzerland	?	Eocene	†*Physogaleus alabamensis*	doi:10.1017/pab.2021.6
EMRG-Chond-T-74	21	Institute of Palaeontology, Vertebrate Collection, University of Vienna (David J. Ward)	Morocco (Ad Dakhla)	Eocene	†*Physogaleus alabamensis*	doi:10.1017/pab.2021.6
NA	2	Haimuseum Aathal Switzerland	USA (New Jersey)	Early Miocene	†*Physogaleus contortus*	doi:10.1017/pab.2021.6
EMRG-Chond-T-75	26	Institute of Palaeontology, Vertebrate Collection, University of Vienna (David J. Ward)	USA (North Carolina)	Early Miocene	†*Physogaleus contortus*	doi:10.1017/pab.2021.6
P.9083-4	2	Natural History Museum London	Argentina	Late Oligocene	†*Physogaleus contortus*	doi:10.1017/pab.2021.6
NA	1	Florida Museum of Natural History	USA (Florida)	Miocene	†*Physogaleus contortus*	doi:10.1017/pab.2021.6
UF 227864	1	Florida Museum of Natural History	USA (Florida)	Early Pliocene	†*Physogaleus contortus*	doi:10.1017/pab.2021.6
UF 228424	1	Florida Museum of Natural History	USA (Florida)	Middle Miocene	†*Physogaleus contortus*	doi:10.1017/pab.2021.6
UF 231020	1	Florida Museum of Natural History	USA (Florida)	Middle Miocene	†*Physogaleus contortus*	doi:10.1017/pab.2021.6
UF 231225	3	Florida Museum of Natural History	USA (Florida)	Middle Miocene	†*Physogaleus contortus*	doi:10.1017/pab.2021.6
UF 240509	1	Florida Museum of Natural History	USA (Florida)	Late Miocene	†*Physogaleus contortus*	doi:10.1017/pab.2021.6
UF 28779	7	Florida Museum of Natural History	USA (Florida)	Middle Miocene	†*Physogaleus contortus*	doi:10.1017/pab.2021.6
UF/V 9977	1	Florida Museum of Natural History	USA (Florida)	Early Miocene	†*Physogaleus contortus*	doi:10.1017/pab.2021.6
UF/TRO 11514	1	Florida Museum of Natural History	USA (Florida)	Middle Miocene	†*Physogaleus contortus*	doi:10.1017/pab.2021.6
UF/TRO 14490	1	Florida Museum of Natural History	USA (Florida)	Middle Miocene	†*Physogaleus contortus*	doi:10.1017/pab.2021.6
UF/TRO 14631	3	Florida Museum of Natural History	USA (Florida)	Middle Miocene	†*Physogaleus contortus*	doi:10.1017/pab.2021.6
UF/TRO 15103	2	Florida Museum of Natural History	USA (Florida)	Middle Miocene	†*Physogaleus contortus*	doi:10.1017/pab.2021.6
UF/TRO 15236	1	Florida Museum of Natural History	USA (Florida)	Late Miocene	†*Physogaleus contortus*	doi:10.1017/pab.2021.6
UF/TRO 15241	1	Florida Museum of Natural History	USA (Florida)	Middle Miocene	†*Physogaleus contortus*	doi:10.1017/pab.2021.6
UF/TRO 15442	5	Florida Museum of Natural History	USA (Florida)	Middle Miocene	†*Physogaleus contortus*	doi:10.1017/pab.2021.6
UF/TRO 9881	2	Florida Museum of Natural History	USA (Florida)	Middle Miocene	†*Physogaleus contortus*	doi:10.1017/pab.2021.6

Supplementary Table S6. Shark Linear Discriminant Analyses

a) LDA Shark genera (6 PCs)
Genera Confusion Matrix

	Carcharhinus	*Galeocerdo*	*Hemipristis*	*Physogaleus*
Carcharhinus	0.571428571	0	0.224489796	0
Galeocerdo	0	76.58843537	0.044217687	6.741496599
Hemipristis	0.108843537	0.360544218	0.880952381	0.197278912
Physogaleus	0	1.962585034	0.891156463	11.42857143

Accuracy	0.89
Cohen's Kappa	0.6652854

Gorongosa fossil predictions (posterior probabilities)	*Carcharhinus*	*Galeocerdo*	*Hemipristis*	*Physogaleus*
Gorongosa_A_PPG2019-P-129	0.00%	97.53%	0.02%	2.45%
Gorongosa_B_PPG2019-P-127	0.00%	96.04%	1.81%	2.16%

b) LDA using *Galeocerdo & Physogaleus* genera (4 PCs)
Galeocerdo & Physogaleus Confusion Matrix

	Galeocerdo aduncus	*Galeocerdo capellini*	*Galeocerdo clarkensis*	*Galeocerdo cuvier*	*Galeocerdo eaglesomei*	*Galeocerdo mayumbensi*	*Physogaleus alabamen*	*Physogaleus contortus*
Galeocerdo aduncus	11.03759398	0.285714286	1.255639098	3.597744361	0.045112782	0	1.436090226	0.996240602
Galeocerdo capellini	0	0.116541353	0	0.165413534	0.007518797	0	0.011278195	0
Galeocerdo clarkensis	0.206766917	0.007518797	0.078947368	0.063909774	0.105263158	0	0.15037594	0
Galeocerdo cuvier	6.469924812	3.763157895	0.578947368	34.27067669	0.545112782	0.80075188	0.639097744	0.296992481
Galeocerdo eaglesomei	0.308270677	0.109022556	0.218045113	0.815789474	4.07518797	0.387218045	0.684210526	0
Galeocerdo mayumbensis	0	0.229323308	0.304511278	0.289473684	0.184210526	4.827067669	0	0
Physogaleus alabamensis	1.015037594	0	1.72556391	0.646616541	0.30075188	0	3.721804511	0.236842105
Physogaleus contortus	0.511278195	0	0.34962406	0	0	0	0.12406015	12.0037594

Accuracy	0.7022556
Cohen's Kappa	0.5994338

Gorongosa fossil predictions (posterior probabilities)	*Galeocerdo aduncus*	*Galeocerdo capellini*	*Galeocerdo clarkensis*	*Galeocerdo cuvier*	*Galeocerdo eaglesomei*	*Galeocerdo mayumbensi*	*Physogaleus alabamen*	*Physogaleus contortus*
Gorongosa_A_PPG2019-P-129	12.36%	16.61%	11.22%	27.80%	13.72%	12.54%	5.75%	0.00%
Gorongosa_B_PPG2019-P-127	35.43%	1.01%	28.05%	8.16%	6.62%	0.19%	20.42%	0.12%

c) LDA using *Galeocerdo* species (4 PCs)
Galeocerdo species confusion Matrix

	Galeocerdo aduncus	*Galeocerdo capellini*	*Galeocerdo clarkensis*	*Galeocerdo cuvier*	*Galeocerdo eaglesomei*	*Galeocerdo mayumbensis*
Galeocerdo aduncus	17.06132075	0.429245283	3.382075472	3.844339623	0.023584906	0
Galeocerdo capellini	0	0.367924528	0.051886792	0.731132075	0.04245283	0
Galeocerdo clarkensis	0.273584906	0.018867925	0.54245283	0.113207547	0.533018868	0
Galeocerdo cuvier	6.806603774	4.443396226	0.981132075	44.33962264	0.768867925	1
Galeocerdo eaglesomei	0.386792453	0.113207547	0.235849057	0.716981132	4.985849057	0.872641509
Galeocerdo mayumbensis	0	0.287735849	0.466981132	0.254716981	0.25	5.674528302

Accuracy	0.729717
Cohen's Kappa	0.5749247

Gorongosa fossil predictions (posterior probabilities)	*Galeocerdo aduncus*	*Galeocerdo capellini*	*Galeocerdo clarkensis*	*Galeocerdo cuvier*	*Galeocerdo eaglesomei*	*Galeocerdo mayumbensis*
Gorongosa_A_PPG2019-P-129	9.43%	12.75%	11.14%	31.04%	18.08%	17.54%
Gorongosa_B_PPG2019-P-127	47.18%	0.11%	37.04%	2.52%	13.09%	0.07%

Confusion matrix entries are average cell counts across the 200 resamples

Supplementary Table S7. Hyracoid comparative sample - mandibles

Specimen Number	Museum	Online repository	Genus	Species	doi/ark
KA1−1190	Ditsong National Museum of Natural History	Morphosource	*Procavia*	*Procavia transvaalensis*	doi:10.17602/M2/M5459
G7052	Ditsong National Museum of Natural History	Morphosource	*Procavia*	*Procavia* sp.	doi:10.17602/M2/M5470
H.5281.B	University Museum of Zoology, Cambridge	Morphosource	*Dendrohyrax*	*Dendrohyrax arboreus*	doi:10.17602/M2/M48250
RU18568	National Museums of Kenya		*Afrohyrax*	*Afrohyrax* sp.	
ZP349	National Museums of Kenya		*Afrohyrax*	*Afrohyrax championi*	
RU15198(A)	National Museums of Kenya		*Afrohyrax*	*Afrohyrax championi*	
DPC2150	Duke Lemur Center Division of Fossil Primates	Morphosource	*Saghatherium*	*Saghatherium humarum*	ark:/87602/m4/M103969
DPC18145	Duke Lemur Center Division of Fossil Primates	Morphosource	*Saghatherium*	*Saghatherium bowni*	ark:/87602/m4/M31737
DPC17675	Duke Lemur Center Division of Fossil Primates	Morphosource	*Thyrohyrax*	*Thyrohyrax meyeri*	ark:/87602/m4/M81579
DPC13282	Duke Lemur Center Division of Fossil Primates	Morphosource	*Saghatherium*	*Saghatherium bowni*	ark:/87602/m4/M83288
DPC2763	Duke Lemur Center Division of Fossil Primates	Morphosource	*Thyrohyrax*	*Thyrohyrax domorictus*	ark:/87602/m4/M103971
DPC15384	Duke Lemur Center Division of Fossil Primates	Morphosource	*Saghatherium*	*Saghatherium bowni*	
DPC5283	Duke Lemur Center Division of Fossil Primates	Morphosource	*Megalohyrax*	*Megalohyrax eocaenus*	ark:/87602/m4/M104021
DPC12048	Duke Lemur Center Division of Fossil Primates	Morphosource	*Saghatherium*	*Saghatherium bowni*	ark:/87602/m4/M81573

Supplementary Table S8. Hyracoid comparative sample - m3

Specimen Number	Museum	Online repository	Genus	Species	doi/ark	notes
ZP1508	National Museums of Kenya		*Bunohyrax*	*Bunohyrax* aff. *fajumensis*		cast
RU15198(A)	National Museums of Kenya		*Afrohyrax*	*Afrohyrax championi*		
DPC7369	Duke Lemur Center Division of F	Morphosource	*Thyrohyrax*	*Thyrohyrax domorictus*	ark:/87602/m4/M104159	
RU18568	National Museums of Kenya		*Afrohyrax*	*Afrohyrax* sp.		
ZP349	National Museums of Kenya		*Afrohyrax*	*Afrohyrax championi*		cast
ZP347	National Museums of Kenya		*Afrohyrax*	*Afrohyrax championi*		cast
ZP1211	National Museums of Kenya		*Thyrohyrax*	*Thyrohyrax domorictus*		cast
WK18206(A)	National Museums of Kenya		*Afrohyrax*	*Afrohyrax championi*		
DPC2763	Duke Lemur Center Division of F	Morphosource	*Thyrohyrax*	*Thyrohyrax domorictus*	ark:/87602/m4/M103971	
DPC18145	Duke Lemur Center Division of F	Morphosource	*Saghatheriun*	*Saghatherium bowni*	ark:/87602/m4/M31737	
DPC2150	Duke Lemur Center Division of F	Morphosource	*Saghatheriun*	*Saghatherium humarum*	ark:/87602/m4/M103969	
DPC5283	Duke Lemur Center Division of F	Morphosource	*Megalohyrax*	*Megalohyrax eocaenus*	ark:/87602/m4/M104021	
DPC12048	Duke Lemur Center Division of F	Morphosource	*Saghatheriun*	*Saghatherium bowni*	ark:/87602/m4/M81573	
NW22558 (C)	National Museums of Kenya		*Meroehyrax*	*Meroehyrax kyongoi*		
DPC17675	Duke Lemur Center Division of F	Morphosource	*Thyrohyrax*	*Thyrohyrax meyeri*	ark:/87602/m4/M81579	
DPC15384	Duke Lemur Center Division of F	Morphosource	*Saghatheriun*	*Saghatherium bowni*		
DPC13282	Duke Lemur Center Division of F	Morphosource	*Saghatheriun*	*Saghatherium bowni*	ark:/87602/m4/M83288	
ZP1255	National Museums of Kenya		*Parapliohyra*	*Parapliohyrax mirabilis*		cast
BN802 (H)	National Museums of Kenya		*Parapliohyra*	*Parapliohyrax ngororaensis*		
LP22529	National Museums of Kenya		*Thyrohyrax*	*Thyrohyrax microdon*		
KA1–1190	Ditsong National Museum of Na	Morphosource	*Procavia*	*Procavia transvaalensis*	doi:10.17602/M2/M5459	
G7052	Ditsong National Museum of Na	Morphosource	*Procavia*	*Procavia* sp.	doi:10.17602/M2/M5470	
H.5281.B	University Museum of Zoology, (	Morphosource	*Dendrohyrax*	*Dendrohyrax arboreus*	doi:10.17602/M2/M48250	
NK41304	National Museums of Kenya		*Dendrohyrax*	*Dendrohyrax* cf. *validus*		
NK36934	National Museums of Kenya		*Dendrohyrax*	*Dendrohyrax* cf. *validus*		